Modeling non-premixed flames in the presence of electric fields

This is a PhD Thesis

Original Citation:
Modeling non-premixed flames in the presence of electric fields / Di Renzo, Mario. - (2018). [10.60576/poliba/iris/di-renzo-mario_phd2018]

Availability:
This version is available at http://hdl.handle.net/11589/121884 since: 2018-02-07

Published version
Politecnico di Bari
DOI:10.60576/poliba/iris/di-renzo-mario_phd2018

Department of Mechanics, Mathematics and Management

Mechanical and Management Engineering
Ph. D. Program

SSD: ING-IND/06 – Fluid Dynamics

Final dissertation

Modeling non-premixed flames in the presence of electric fields

by

Mario Di Renzo

Referees:
Dr. Donato Cecere
Dr. Javier Urzay

Supervisors:
Prof. Giuseppe Pascazio

Prof. Marco D. de Tullio

Coordinator of the Ph. D. Program:
Prof. Giuseppe P. Demelio

Course n° 30, 01/11/2014-31/10/2017

Politecnico di Bari

Abstract

Department of Mechanics, Mathematics and Management

Ph. D. in Mechanical and Management Engineering

Modeling non-premixed flames in the presence of electric fields

by Mario DI RENZO

The impingement of electric fields on flames is known to have potential for mitigating combustion instabilities, enhancing flame propagation and decreasing pollutant emissions. In this work, a computational analysis of counterflow methane-oxygen laminar diffusion flames impinged by electric fields is performed, using axisymmetric numerical simulations, complex transport and a detailed chemistry mechanism, with the final aim of studying in detail the effects of electric fields on the flow and the kinetics. The electric field steers the charged intermediate species, which exchange momentum with the rest of the gas, thereby changing the flow around the flame and creating an ionic wind whereby anions and cations flow towards the corresponding electrodes. As a result, the aerothermal field and scalar dissipation rate undergo variations that may be of significance for the subgrid-scale modeling of turbulent flames subject to electric fields. The results are found to agree well with previous experiments considering the state-of-the-art on this type of calculations. The same numerical configuration has also been studied with a newly developed flamelet model in the mixture fraction space able to account for the impinging electric field. The results of this model have been compared with those of the aforementioned detailed model showing a very good agreement between the two sets of data. Thanks to the lower dimensionality of the model, the computational cost of each simulation is very low and, therefore, it can be employed for computing enough flamelets to construct a complete electrified s-curve for a particular chemical configuration. This study determines the response of the reacting layer to the applied electric field in a wide range of reaction regimes regulated by the variation of the diffusion time scale. The last part of the present work describes an efficient flamelet progress-variable approach developed to model the fluid dynamics of flames immersed in an electric field. The main feature of this model is that it can use complex ionization mechanisms without increasing the computational cost of the simulation. The model is based on the assumption that the combustion process is not directly influenced by the electric field. It has been tested using two chemi-ionization mechanisms of different complexity, in order to examine its behavior with and without the presence of heavy anions in the mixture. Using one- and two-dimensional numerical test cases, the proposed flamelet progress-variable approach has been able to reproduce all the major aspects encountered when a flame is subject to an imposed electric field and the main effects of the different chemical mechanisms. Moreover, the proposed model is shown to produce a large reduction in the computational cost, being up to 40 times faster than the standard simulation methods.

Keywords: Electric field-flame interaction; Ionic wind; Chemi-ionization; Electrified flamelet; Flamelet progress-variable model.

Contents

List of Figures

List of Tables

List of Abbreviations

AC	**A**lternate **C**urrent
CFD	**C**omputational **F**luid **D**ynamics
CFL	**C**ourant–**F**riedrichs–**L**ewy
DC	**D**irect **C**urrent
EEDF	**E**lectron **E**nergy **D**istribution **F**unction
FPV	**F**lamelet **P**rogress **V**ariable
LHS	**L**eft **H**and **S**ide
ODE	**O**rdinary **D**ifferential **E**quation
PIV	**P**article **I**mage **V**elocimetry
RHS	**R**ight **H**and **S**ide

Physical Constants

Avogadro Number	$N_a = 6.022\,14 \times 10^{23}/\mathrm{mol}$
Free-space electric permittivity	$\epsilon_0 = 8.854\,187\,817\,6 \times 10^{-12}\,\mathrm{F/mol}$
Universal gas constant	$\mathcal{R} = 8.314\,459\,8\,\mathrm{J/(K\,mol)}$
Elementary charge	$e = 1.602\,18 \times 10^{-19}\,\mathrm{C}$
Boltzmann constant	$k_B = 1.380\,648\,52 \times 10^{-23}\,\mathrm{J/K}$

List of Symbols

A	Strain rate	1/s
C	Progress variable	-
$E_{a,j}$	Jth reaction specific activation energy	kJ/mol
I	Electric current	A
J	Electric current density	A/s
$K_{br,j}$	Jth backward reaction rate	$\mathrm{cm^{3n}/mol^{n}/s}$
$K_{eq,j}$	Jth reaction equilibrium constant	-
$K_{fr,j}$	Jth forward reaction rate	$\mathrm{cm^{3n}/mol^{n}/s}$
M	Negative charge density	C/kg
P	Positive charge density	C/kg
T	Mixture temperature	K
Z	Mixture fraction	-
$\Omega_{ij}^{(1,1)*}$	Ith species collision integral with jth species	-
$\Omega_{i}^{(2,2)*}$	Ith species collision integral	-
Φ	Electric potential	V
$\mathcal{S}_i$	Ith species number of elementary charges	-
χ	Scalar dissipation rate	1/s
δ_m	Mixing layer thickness	m
α_i	Ith species diffusivity	$\mathrm{m^2/s}$
$\alpha_{T,i}$	Ith species thermal diffusivity	$\mathrm{m^2/(s\,K)}$
α_Z	Mixture fraction diffusivity	$\mathrm{m^2/s}$
α_M	Negative charge density diffusivity	$\mathrm{m^2/s}$
α_P	Positive charge density diffusivity	$\mathrm{m^2/s}$
α_C	Progress variable diffusivity	$\mathrm{m^2/s}$
η_i	Ith species dynamic viscosity	$\mathrm{kg/(m\,s)}$
η	Mixture dynamic viscosity	$\mathrm{kg/(m\,s)}$
λ_i	Ith species thermal conductivity	$\mathrm{W/(m\,s)}$
λ	Mixture thermal conductivity	$\mathrm{W/(m\,s)}$
$\mathcal{A}_j$	Jth reaction pre-exponential coefficient	$\mathrm{cm^{3n}/mol^{n}/s}$
Y_i	Ith species mass fraction	-
W_i	Ith species molar mass	kg/mol
W	Mixture molar mass	kg/mol
k_i	Ith species mobility	$\mathrm{m^2/(s\,V)}$
k_M	Negative charge density mobility	$\mathrm{m^2/(s\,V)}$
k_P	Positive charge density mobility	$\mathrm{m^2/(s\,V)}$
n_i	Ith species number density	$\mathrm{part/m^3}$
ν''	Stoichiometric coefficient of the species as product of a reaction	-
ν'	Stoichiometric coefficient of the species as reactant of a reaction	-
ν	Mixture kinematic viscosity	$\mathrm{m^2/s}$
ϕ	Mixture equivalence ratio	-

$\dot{\omega}_i$	Ith species production rate	1/s
$\dot{\omega}_M$	Negative charge density production rate	1/s
$\dot{\omega}_P$	Positive charge density production rate	1/s
$\dot{\omega}_C$	Progress variable production rate	1/s
$\rho_{p,i}$	Ith particle density	kg/m^3
$\rho_{q,i}$	Ith species electric charge density	C/m^3
ρ_q	Mixture electric charge density	C/m^3
ρ	Gas density	kg/m^3
σ_i	Ith species Lennard–Jones collision diameter	m
$\mathbf{V}_i$	Ith species diffusion velocity	m/s
$\mathbf{u}_{p,i}$	Ith particle velocity	m/s
$\mathbf{x}_{p,i}$	Ith particle position	m
X_i	Ith species molar fraction	-
ξ_i	Ith species Lennard–Jones potential well-depth	J
$a_{p,i}$	Ith particle diameter	m
c_p	Mixture constant pressure heat capacity	J/(kg K)
c_{p_i}	Ith species constant pressure heat capacity	J/(kg K)
h_i	Ith species specific enthalpy	J/kg
n_j	Jth reaction temperature exponent	-
p_{th}	Thermodynamic pressure	Pa
p	Pressure	Pa
$q_{p,i}$	Ith particle electric charge	C
u	Flow velocity magnitude	m/s
$\overline{\overline{S}}$	Strain tensor	1/s
$\overline{\overline{\sigma}}$	Viscous stress tensor	Pa
$\mathbf{E}$	Electric field	V/m
$\mathbf{g}$	Acceleration of gravity	m/s^2
$\mathbf{u}$	Flow velocity	m/s

List of Dimensionless Numbers

$\mathrm{Le}_i = \dfrac{\lambda}{\rho\alpha_i c_p}$	I^{th} species Lewis number
$\Theta = \dfrac{u_{ref}L_{ref}}{\Delta\Phi_{ref}k_{ref}}$	Ion wind number
$\Xi = \dfrac{\epsilon_0(\Delta\Phi_{ref})^2}{\rho_{ref}u_{ref}^2L_{ref}^2}$	Electric interaction parameter
$\mathrm{Da} = \dfrac{L_{ref}}{u_{ref}}\dfrac{\rho_{ref}\mathcal{A}_{ref}}{W_{ref}}\exp\left(-\dfrac{E_{a,ref}}{\mathcal{R}\Delta T_{ref}}\right)$	Damköhler number
$\mathrm{Ec} = \dfrac{u_{ref}^2}{c_{p,ref}\Delta T_{ref}}$	Eckert number
$\mathrm{Fr} = \dfrac{u_{ref}}{\sqrt{\lvert\mathbf{g}\rvert L_{ref}}}$	Froude number
$\mathrm{Pr} = \dfrac{\nu_{ref}c_{p,ref}\rho_{ref}}{\lambda_{ref}}$	Prandtl number
$\mathrm{Re} = \dfrac{u_{ref}L_{ref}}{\nu_{ref}}$	Reynolds number
$\mathrm{Sc} = \dfrac{\nu_{ref}}{\alpha_{ref}}$	Schmidt number
$\mathrm{St}_i = \dfrac{2}{9}\dfrac{a_{p,i}^2}{\nu_{ref}}\dfrac{\rho_{p,i}}{\rho_{ref}}\dfrac{1}{t_{ref}}$	Stokes number

Chapter 1

Introduction

1.1 Motivations and objectives

Rocket and aircraft engines, piston engines and boilers are just a few examples of systems that, during their life, may experience problems related to combustion instability. In fact, the nowadays combustion chambers are frequently operated very close to their extinction limits in order to comply with the stringent requirement of efficiency, weight reduction and low emissions imposed by the market and by the regulations. In this context, being able to control the flame behavior is a crucial aspect for enlarging the design options for these systems and improve their effectiveness.

In particular, experimental tests have demonstrated that both premixed and diffusion flames can be controlled by the impingement of an external electric field. Those experiments have provided: detailed analyses of the ionic chemistry of hydrocarbon flames [38, 39, 118]; laminar premixed-flame speed augmentation by electric fields [35, 63]; electric extinction of liquid-pool fires and jet diffusion flames [96]; electrically-induced instabilities in premixed flames [57, 115, 120]; modification of the amount of soot produced by the combustion [56, 119]; augmentation of the atomization in spray flames [36] and variations of lift-off heights jet diffusion flames with electric fields [19, 47, 54, 60, 122]. A big advantage of this concept, especially from an industrial point of view, is the minimal number of modifications needed by existing burner in order to employ this technology [3]. In fact, they mainly consist in the addition to the combustor of a number of electrodes that, connected to an electric power generator, apply a difference of electric potential in the flame region. Thanks to the electric conductive capabilities of the modern ceramic thermal barrier coatings these electrodes can be embedded in the combustor structure limiting the weight and complexity increase penalties. Moreover, being the flame in most of the applications electrically isolated from the electrodes by the surrounding gas mixture, the amount of current produced in the electric circuit is very low, entailing a negligible amount of power required to operate the control system.

In spite of the experimental evidence, very few models have been developed for the prediction of this phenomenon, and none of them is suitable for practical design purposes because of the high computational complexity. In fact, most of the numerical studies in the literature about this topic involve the computation of simplified configuration as one-dimensional premixed flames. Therefore, the first objective of the present thesis is to extend the application of these detailed models to more complex flames, studying how the known phenomena triggered by the impinging electric field are modified by the different features of these flows. Then, the knowledge gained through the analysis of the detailed solutions will be used to formulate reduced order models, which, reducing the computational cost of the simulation, will eventually allow one to predict the effect of an electric field on complex turbulent flames with an acceptable computational effort.

1.2 A brief review of the phenomenon from experimental evidence

To the best of the author's knowledge, the first studies present in the literature about the electrical properties of the flames are dated to the beginning of the 1930's [11, 40, 61]. Since that time, the ease of producing this phenomenon and the economic benefits deriving from the ability to govern the combustion processes led to the production of a large number of experimental studies in this field. The attention of the researchers has been focused on understanding two main classes of interaction between the electric field and the reacting layer of the flame: the modification of the chemical process and the hydrodynamic effects.

Both types of interaction rely on the intrinsic capability of flames to produce ionized species and free-electrons, which revealed to be an important property for the diagnosis and the control of combustion. Wortberg [118] was probably the first to quantify the number of ions produced in the reacting region of a methane/oxygen premixed laminar flame. Later, using similar experiments, Goodings and Bohme [37] and Goodings et al. [38, 39] provided further measurements to the ion concentrations in the premixed flame and speculated about the main reactions involved in the chemi-ionization mechanism. They proposed that the main ionization pattern was based on the reaction that, because of the high temperature, produces CHO^+ and e^- from the radical CH and atomic oxygen. Interestingly, even though the technology used in these studies has shown some limitations over the years, their experiments are still used to validate the nowadays chemi-ionization mechanisms for methane, which most of the times are based on the ionization pattern of Goodings and Bohme [37]. This property of the flame front has revealed to be particularly useful in the construction of sensors for the diagnosis of the flame stability in industrial combustion chambers. These sensors, taking advantage of the different transport properties of the ions produced in the reacting region, are able to give information regarding the flame conditions measuring a difference of electric potential produced by the flame itself. This difference of potential is usually of the order of $1\,\mathrm{V}$ [1, 68, 75].

One of the first experiments that tried to quantitatively show the impact of an electric field on the flame velocity has been published by Jaggers and Engel [51]. They proposed two different types of combustion regimes: a premixed flame front propagating in a tube and a floating flat flame. In both the experiments, two electrodes are used to apply a difference of electric potential in a direction parallel to the flame front. Such a configuration is chosen in order to minimize the effect of the electric force on the flow avoiding the presence of a force component in the direction of the flame front propagation. Jaggers and Engel [51] were able to show a doubling of the laminar flame speed because of the ion wind. This increase of the overall combustion rate was attributed to the ability of the ionized species, steered by the electric filed, to collide with the reacting molecules producing species that, being less chemically stable, promote the oxidation process. Interestingly, this effect is achieved even in the case when the applied electric field is not sufficiently strong to promote the presence of non-thermal effects ($|\mathbf{E}| < 200\,\mathrm{Td}$ [64]). Another noteworthy aspect of this phenomenon pointed out in this work is the influence of the type of applied voltage. In fact, Jaggers and Engel [51] shown that the use of a Direct Current (DC) is more effective in this case, compared with Alternate Current (AC), being able to determine a larger displacement of the electron distribution, increasing their ability to collide with the neutral species. More recently, a more drastic modification of the combustion chemistry has been achieved using electric fields. It consists in ionizing the mixture breaking its own dielectric strength and generating a large amount of plasma. Recent studies [34, 74, 104] have shown that this technique can strongly enhance the overall combustion rate thanks to the high amount of energetic particles produced during the discharge. On the other hand, the electrons, subjected to the very high electric force produced in these systems, generate excited molecules through a series of anelastic and super-elastic collisions, determining a deviation of the species temperature distribution from the classical Maxwell-Boltzmann shape. These systems, which require particular attention in the treatment of the chemical processes involved during the combustion and the discharge, are achieved with electric fields intensity far beyond the values considered in the present work and, therefore, they will not be further discussed.

The second type of interactions is instead based on modifying the momentum of the flow taking advantage of the charged species produced by the flame. In fact, the electric force exerted on the ionized particles exposed to an electric field is transmitted to the neutral particles of the mixture by means of elastic collisions. This mechanism generates a local force on the flow that can be used to produce specific fluid dynamic features. The existence of this effect has been at first postulated by Lawton and Weinberg [59]. These scientists were the first to relate the presence of an ion wind flowing from the flame to the electrodes with the presence of a body force applied on the flow. In fact: i) defining the total electric force density applied on the flow as

$$\mathbf{f}_{el} = e\mathbf{E}(n^{+} - n^{-}), \tag{1.1}$$

where:

- $\mathbf{E}$ is the local electric field vector,
- n^{+} and n^{-} are the local number density of positive and negative particles,
- e is the elementary charge;

ii) considering that, in first approximation, the electric flux due to positive and negative charges can be respectively computed as

$$\mathbf{J}^{+} = e\mathbf{E}n^{+}k^{+}; \qquad \mathbf{J}^{-} = e\mathbf{E}n^{-}k^{-}; \tag{1.2}$$

being k^{+} and k^{-} an average electric mobility of the positive and negative species, respectively; Lawton and Weinberg [59] formulated the equation

$$\mathbf{f}_{el} = \frac{\mathbf{J}^{+}}{k^{+}} - \frac{\mathbf{J}^{-}}{k^{-}}, \tag{1.3}$$

which relates the presence of an electric force ($\mathbf{f}_{el}$) applied on the flow by the ion flux ($\mathbf{J}$) through a measure of the number of collisions that the particles undergo when the Lorentz force is exerted on them (the electrical mobility k). It has also been demonstrated that more complex flow modifications consisting in toroidal vortices can be achieved using the Hall effect in cases with very high frequency and amplitude AC applied voltage. Unfortunately, the study of this effect is more complicated than for the chemical pattern modification discussed earlier because of the difficulties in producing an experiment that isolates this phenomenon.

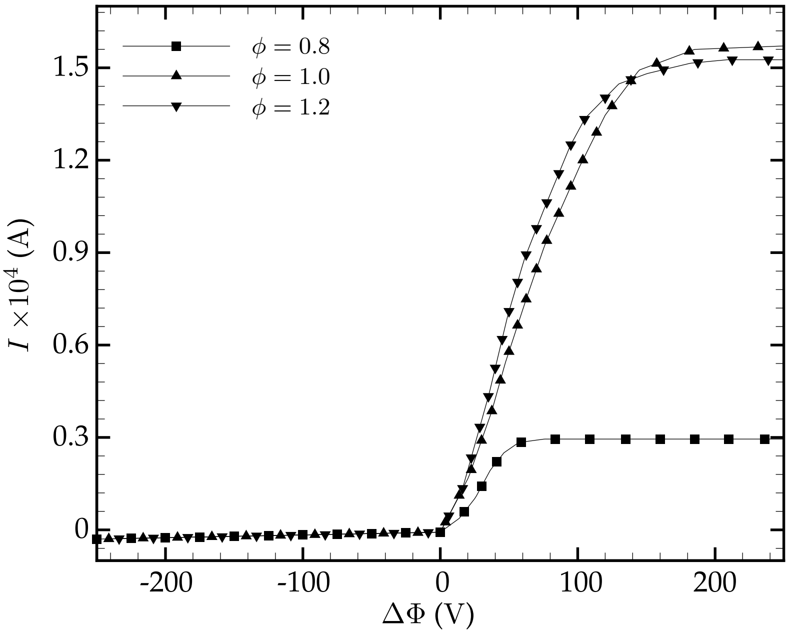

FIGURE 1.1: Characteristic ion-current response of an electrified flame to the applied voltage for various equivalence ratios (ϕ) [100].

The description of the phenomena involved in the impingement of the electric field on the reacting layer clearly highlights the importance of the displacement induced on the intermediate charged particles on the properties of the flame response. Marcum and Ganguly [63] were probably the first to perform an analysis on this aspect showing the scaling of the ion-current with respect to the applied voltage for a premixed conical propane-air flame burning between two electrodes, whose purpose is to generate an electric field parallel to the flow direction. These two electrodes configuration is one of the most used electrical solutions employed in the electrified flames tested so far because it guarantees good control over the shape of the applied electric field. On the other hand, positioning an electrode inside the burnt mixture poses technological issues because of the aging of the metallic material exposed to the high temperatures produced by the flame. The ion current entering the electrodes is probably the most common integral quantity used in modeling works and experiments to describe the electric properties of a flame because of its ease of measuring and because of the number of information that provides regarding the number and nature of ions produced by the flame. A typical ion current response curve to an applied electric field for a premixed flame is shown in Figure 1.1. The first feature pointed out in this work is the so-called "diodic effect". In fact, these response curves are usually characterized by different values of current depending on the polarity of the DC voltage, resembling the electrical behavior of a diode. This phenomenon is characteristic of this kind of premixed flames and it is due to the presence of free-electrons among the negative ions. Thanks to their low mass, compared to the positive ions (which are, at least, composed of one atom), the electrons have a very high electrical mobility and therefore they can be much more easily steered by the electric field. Because of conservation of charge, at steady state or at least in a time-averaged sense, the integral fluxes of positive and negative ions out of the domain have to be the same [43]. If the two electrodes are positioned at different distances from the reacting region, as it usually happens in this kind of premixed flames, the polarity that forces the positive ions to flow over the shortest distance will also produce the higher current density. In fact, a reduction of the amount of space that the species with lower electrical mobility have to cover before entering the electrode, colliding with the surrounding mixture, decreases the electric resistance of the system. The second phenomenon shown by the scaling of the ion-current with the applied voltage is the electrical saturation of the flame. When the flame is not exposed to an electric field, the charged particles are produced and recombined at the same rate inside the reacting layer generating a negligible ion-current. If an electric field is applied, the positive and negative charges move in opposite directions reducing the region of space where they coexist and, therefore, their recombination rate. Since the ion production rate only depends on the concentration of the neutral species and on the temperature, if the flame does not undergo any particular modification, it can be considered constant in a first approximation. This mechanism is responsible of the relation between the ion-current and the applied voltage in the region of the graph in Figure 1.1 between $\Delta\Phi = 0\,\mathrm{V}$ and $60\,\mathrm{V}$. This condition of the flame is called the sub-saturated regime and it is characterized by a super-linear increase of the ion-current (decrease of the recombination charge rate) with the applied voltage. In this condition, part of the charged particles remains around the flame creating a sort of Faraday cage around the reacting layer. Therefore, the electric potential forms a plateau in the flame region, letting the flame to behave as a sort of additional electrode [19, 43]. If the electric field is increased, the recombination rate of the ions will eventually become zero. At that point, the total amount of ions produced by the flame is drained toward the electrodes and, therefore, the ion-current becomes independent of the applied voltage. For this reason, this is called the saturated condition. A small region at constant electric potential is still present but it tends to disappear increasing the voltage. Because of the relation in Equation (1.3), also the electric force applied to the flow reaches a plateau. Once the saturation voltage is reached, the only way to further increase the electric current measured at the electrodes is to break the dielectric strength of the mixture, causing the formation of discharges.

In order to better understand the effectiveness of this technology but also the level of uncertainty related to the measurements of these phenomena, the outcomes of a series of studies present in the literature about the reaction of lifted diffusion propane flames will be compared in Table 1.1. The first important aspect that can be inferred from the data reported in the table is the higher efficiency of the AC voltage with respect to the DC in stabilizing the flame. This result seems in contradiction with the findings of Jaggers and Engel [51], suggesting that the stabilization of these flames may be mainly governed by the effect of the ion-wind on the flow rather than by the modification of the chemical mechanism. This trend is present in all the mentioned experimental studies, where the effects of the two types of current are compared with the exception of the work of Won et al. [117]. Their experiments consisted in a lifted tribrachial propane-air flame propagating in a co-flow burner from an ignition position in the downstream side of the combustion chamber to its steady-state position near the fuel injection point. In this experiment, the fuel nozzle itself was used as an electrode in order to apply the voltage. Unlike the double electrodes configuration described in the previous paragraph, this single electrode arrangement is the simplest solution used to electrify a flame, but, on the downside, it gives a reduced control on the shape of the electric potential field, since relies on the surrounding grounded environment (the laboratory in this case) to produce the difference of potential. In contradiction to the all the other studies, Won et al. [117]

TABLE 1.1: Effects of the applied electric field parameters on diffusive propane flames. P = Proportional; MP = Marginally Proportional; MIP = Marginally Inversely Proportional; IP = Inversely Proportional.; M = Minimal influence

Reference	**Measured quantity**	**Flow regime**	**N° of electrodes**	**AC Voltage**	**AC Frequency**	**DC Voltage**	**Notes**
Lee et al. [60]	Liftoff height	Turbulent	Single electrode	IP	IP at low freq.	MP	-
Won et al. [116]	Reattachment velocity	Laminar	Single electrode	P	IP	MP	-
Won et al. [117]	Propagation speed	Laminar	Single electrode	P	MP	P	-
Kim et al. [54]	Detachment velocity	Laminar	Single electrode	P	M	-	Low voltage
				IP	M	-	Intermediate voltage
				MIP	M	-	High voltage
Hutchins et al. [47]	Liftoff height	Laminar	Double electrode	-	-	IP	Positive polarity
				-	-	P	Negative polarity
Ryu et al. [94]	Liftoff height	Laminar	Single electrode	IP	M	-	Unsteady at low freq.
Cessou et al. [19]		Turbulent	Double electrode	-	-	IP	-

stated that the type of applied current on the propagation speed of their tribrachial flame has marginal influence. Moreover, the authors justified their results claiming that the electric field unsteadiness of the AC voltage, that presumably causes the faster attachment of the flame, was created also in the DC case by the displacement of the flame. Few arguments have been produced to support this point and further investigation seems needed to really understand the phenomena involved in these experiments. Another set of interesting data has been presented by Kim et al. [54]. They used the same experimental apparatus as Won et al. [117] to estimate the stabilizing effect of the electric field increasing the fuel injection velocity from an attached configuration until the liftoff happens. The surprising aspect of this experiment is that three different regimes characterized by three completely different responses of the flame to an increase of applied voltage have been observed. In the first regime, at low differences of potential, the detachment velocity was linearly proportional to the applied voltage. In the second regime, characterized by the appearance of small sparks between the flame and the fuel nozzle, the detachment velocity showed an opposite scaling to the applied voltage. When the applied voltage was sufficiently high to generate streamers between the flame front and the electrode, the detachment velocity became independent of the impinging electric field intensity. Probably, such a peculiar behavior is due to the high currents generated inside the sparks, that, draining the ions from the flame front, reduce the ion-wind hydrodynamic effect. The influence of the AC frequency emerging from these studies seems even more contradictory. On the overall, its effect seems marginal on the flame stabilization process, but comparing the results of Lee et al. [60] and of Won et al. [116] a completely different effect of the increase of this parameter can be pointed out. Lee et al. [60], measuring the liftoff height of a non-premixed turbulent flame, showed that, especially at low frequencies, the increase of the AC frequency had a beneficial effect on the flame stabilization. On the other hand, Won et al. [116] claimed a completely opposite effect on their tribrachial laminar flame. The reasons for such a discrepancy among the results of these experiments on this aspect may be found in the interaction of the ion-wind with the turbulence or in a bias induced by the different quantities used to determine the stabilizing effect. A last noteworthy aspect regarding the influence of the AC frequency has been proposed by Ryu et al. [94]. Their experiment consisted in a lifted triple flame subjected to a low frequency AC voltage and they observed that the liftoff height exhibited an oscillating behavior induced by the electric field. The amplitude of the flame front motion seemed proportional to the applied voltage and inversely proportional to the frequency. This behavior is somehow consistent with the findings of Hutchins et al. [47] on the influence of the DC polarity of the on the liftoff height of a similar flame and it can be used as starting point to develop methods to counteract fluid dynamic instabilities.

The previous analysis has mainly the objective of giving a broad picture of the number and complexity of the problems that are still open in this field from an experimental point of view. Most of the present knowledge on this interaction, gained through the experiments, seems, in fact, more based on phenomenological observation of qualitative quantities, rather than being funded on quantitative measurements. In fact, the electric field that surrounds the flame worsens the already complicated problem of extracting quantitative data at a high resolution from reacting flows. Considering the level of detail in the measurements achievable at the present time, even in a laboratory flames, it is evident the need of employing numerical techniques to predict the integral quantities known from the experimental evidence and to be able to completely understand the physics involved in this complicated kind of flows. The next section will provide a brief description of how the nowadays computational model have approached this complex problem.

1.3 Existing mathematical models

As described in the previous section, the interaction of an electric field with a flame involved in this kind of flow is a strongly multi-physics and multi-scale problem. The intermediate charged species produced by a flame are just a very small percentage of the mixture composition and their presence is regulated by very sensitive chemical equilibria [31]. For this reason, the determination of the local effects of the electric field requires very sophisticated kinetic reaction mechanisms, that still need to be defined in order to accurately predict the production rates of both the neutral and charged species. Moreover, the structure of the molecules that constitute the mixture entails the generation of various types of particle interactions, that regulates their transport properties. Non-trivial issues are also associated with the definition of transport models able to correctly recover the behavior of the large number of species required to predict the chemical kinetics up to the accuracy required to compute the amount of charge present in the mixture.

In order to limit the complexity of the ionization reactions, the development of chemi-ionization mechanism has been so far focused on the combustion of light hydrocarbons. In particular, the attention of the researchers has been drawn to determining the major reactions happening in methane/air combustion. To the best of the author's knowledge, the most detailed mechanism for ionized species has been proposed by Starik and Titova [102]. It consists of 214 equilibrium reactions for the production and depletion of 23 charged species. This mechanism, coupled with a reduced mechanism for the prediction of the CH_4/O_2 neutral species chemistry composed of 392 reactions for the production and depletion of 59 species [23], has been employed to perform zero-dimensional studies on the concentration of the charged particles during the mixture ignition. Another noteworthy kinetic scheme, proposed by Prager et al. [91], is based on the mechanism for the prediction of lean methane-air mixtures combustion assembled by Warnatz et al. [112] (208 reactions among 38 species) and takes into account the production and depletion of 11 charged species through 67 reactions. The most reduced mechanism proposed in this context is contained in the work of Belhi et al. [4]. The ionization process is based on the reaction

$$\mathrm{CH} + \mathrm{O} \longrightarrow \mathrm{HCO}^+ + \mathrm{e}^-, \tag{R1.1}$$

proposed by Goodings et al. [38]. The produced HCO^+ is converted in H_3O^+ trough the reaction

$$\mathrm{HCO}^+ + \mathrm{H_2O} \longrightarrow \mathrm{H_3O}^+ + \mathrm{CO} \tag{R1.2}$$

with a very high reaction rate leaving a very small amount of HCO^+ in the mixture [81]. The H_3O^+ then recombines with the electron producing either water or hydrogen (atomic or molecular) or OH. Later, the same authors [5] defined an extension of the previous mechanism, introducing the electrons attachment mechanisms in order to produce the heavy negative ions studied by Goodings et al. [39].

A large effort has also been spent in the determination of the transport properties, especially concerning the free electrons produced by the flame. A very sophisticated model has been proposed by Bisetti and El Morsli [8], where the electron properties are computed using the momentum transfer cross-sections of the electrons with the main components of the gas mixture. The complexity of the model has been further improved by the same authors [9], including non-thermal effects in the ionization

TABLE 1.2: Summary of the transport model of Han et al. [42].

	Heavy ions	**Electrons**	**Neutral particles**
Heavy ions	Coulomb	Coulomb	(n,6,4)
Electrons	-	Coulomb	Cross-sections
Neutral particles	-	-	LJ/Stockmayer

process. Han et al. [42] have probably been the first to formalize a thorough statistical model of the particle to particle interaction, distinguishing whether the pair of species was composed of neutral or charged species or of electrons. The basic structure of their model is summarized in Table 1.2. The interaction between two neutral particles is modeled with Lennard-Jones/Stockmayer potentials, which is the standard choice used in many previous combustion studies [12, 52, 100]. The model of Bisetti and El Morsli [9] is instead used to determine the binary transport properties of the electrons with the neutral molecules. The (n,6,4) theory, which, unlike the Stockmayer solution, takes into account the presence of the polarization effects induced by the charged particles on neutral species, is used to determine the diffusivity and electrical mobility of heavy ions in rest of the mixture. Coulomb forces dominate the interactions between two charged particles, whether they are both heavy or electrons and heavy ions.

The nonlinear problem obtained by coupling the charged and neutral species transport equations with the conservation equations of the fluid dynamics, with the electrodynamic laws and with the computation of the local reaction rates and species properties has a number of properties that make its numerical solution particularly complex. First of all, as it can be inferred by the number of species employed in be the kinetic mechanisms described earlier, the number of dimensions and unknowns of the problem is very high. Secondly, the large interval of temporal and spatial scales involved in the phenomenon implicates a very high stiffness of the problems making a large number of numerical methods ineffective for the solution of the system. For instance, the simulation of a standard laboratory flame similar to those described in the previous section involves, at the same time, the flow physics, that can happen on scales of the order of the second, the neutral chemistry, that has characteristic time scales of the order of the nanosecond, and the free-electrons, that evolve on scale similar to the picosecond. As a result, being the ratio of the time scales similar to the ratio of the maximum and minimum eigenvalues of the local Jacobian matrix of the nonlinear operator, the resulting stiffness requires the employment of very robust numerical methods, that, at the present time, pose big limitations on the size of the resolved problem. For this reason, the majority of the studies present in the literature, involving detailed chemistry and complex transport models, deal with the description of one-dimensional premixed flames. In fact, in this kind of flames, the solution of the fluid dynamics becomes trivial, needing only the mass conservation equation to determine the velocity field. Moreover, the number of points needed in the computational mesh is small enough to be treated using a Newton-based solver even in the presence on a large number of transported species [2, 81, 100, 101]. Among these studies, probably, Speelman et al. [101] have been the first to employ a complete binary diffusion approach [30], which computes the binary diffusion velocity of the species solving a linear system of equations, that takes into account at the same time the molecular diffusion and the drift due to the electric field. The main advantage of this model is that it conserves the molar mass of each species without the need of any diffusion velocity correction. The works of

Speelman et al. [100, 101] are also among the few studies that provided an experimental validation of the numerical results obtained with their model, evidencing the shortcomings of the nowadays kinetic and transport models.

Only a few simulations have been carried out in two-dimensional configurations in conjunction with a Computational Fluid Dynamics (CFD) approach. One of the first attempts in modeling the interaction of the electric field with the combustion process has been done by Hu et al. [46]. In this model, a co-flow flame and a candle flame of methane in air have been studied using a reduced kinetic mechanism computed at run-time in a two-dimensional configuration. This approach neglects the effect of the local charge distribution on the electric field, therefore considering it constant at each point of the domain. This assumption can often lead to a large underestimation of the local electric field strength and, therefore, to a reduced effect of the voltage difference on the flow. A few years later, a large improvement in modeling the phenomenon has been achieved by Yamashita et al. [123], who computed the capillary combustion chamber already studied experimentally and numerically by Papac [76] and Papac and Dunn-Rankin [77]. The interaction between the charge produced by the flame and the local electrical potential was taken into account solving the Gauss law at each time-step of the simulation. Since the flame was mostly confined close to the metallic surfaces, the presence of the electrons in the mixture was neglected assuming that, because of the high mobility, they would have been rapidly removed. This assumption, in conjunction with a reaction mechanism which considers only the electrons as negatively charged species, probably leads to an over-estimation of the flame response to the voltage.

Although the transport of the entire set of species of the kinetic mechanism guarantees the best accuracy during the calculation, this approach is still computationally too expensive to be applied to real industrial cases. For this reason, the development of reduced order combustion models is necessary even for the computation of two-dimensional configurations. The first solution to this problem has been proposed by Belhi et al. [4, 5]. Neglecting the effect of the production of charged species on the neutral chemistry, the proposed model uses a laminar Flamelet Progress-Variable (FPV) approach [32] to simulate the combustion process. Two equations (one for the mixture fraction Z and one for the progress-variable C) are solved and a tabulated function, namely

$$\psi = \mathcal{F}_{\phi}(Z, C), \tag{1.4}$$

is used to predict the generic thermo-chemical mixture property ψ. An additional transport equation is then added to the system for each charged species considered in the mechanism. The species properties and production rates are computed using the temperature and mass fractions stored in the FPV chem-table (Equation (1.4)). This approach definitely allows one to use detailed schemes for the combustion description, but still, poses limits on the number of species used in the ionization mechanism.

A measure of the amount of work that is still required in the development of these models is the magnitude of the errors encountered in the few validations with experimental data present in the literature. The first kind of comparison with the experimental data regards the amount and type of ions produced inside a one-dimensional premixed flame without any imposed electric voltage. This procedure has been employed mainly to test the accuracy of the chemi-ionization mechanisms formulated over the years. In fact, the absence of an external electric field allows one to assume that the mixture is electrically neutral and to avoid the complexity of the influence of the electric field on the ion transport. As already mentioned earlier in this chapter, the most common set of data for this kind of validation is that provided by Goodings et al. [38, 39]. For instance, one of the best agreement with the experimental data in this context has been shown by Prager et al. [91]. Looking at the number density of the ions in the mixture, they have been able to predict the peak present in the flame front with an overestimation of about 22%. Their mechanism also predicted a faster production and depletion of the ions leading to a much narrower region interested by the presence of the ions and to large errors (of order 100%) far from the flame front. A similar validation has been performed by Belhi et al. [4] using a much more skeletal mechanism of the ion-production (only three reactions among just as many species), but increasing the detail of the neutral chemistry. This mechanism provided much better results in the flame front region, matching the experimental peak of ion number density with an error of about 3-4%. An improvement with respect to the work of Prager et al. [91] was also evident in the recombination rate of the charged species, which, in this case, seemed slower than in the experimental data. Because of this different trend, the ion number density at the downstream end of the combustion chamber computed by Belhi et al. [4] is almost twice the experimental value. Small improvements have been achieved by the same authors including the negative ions chemistry [5]. The comparison is even worse when the effect of the electric field is included and the dependence of the ion current produced by the flame to the applied voltage is analyzed. In fact, in these configurations, being the determination of the electric induced diffusion a mandatory requirement for the determination of the ion distribution, the transport properties of the species are as relevant as the production rates for the computation of the flame response. For instance, Speelman et al. [101], using the kinetic mechanism of Belhi et al. [4] for the neutral and chemical species, computed a saturation current of 197 μA, where the experimental measurement performed by the same authors is of about 70 μA. Even though the transport properties of all the species were based on Stockmayer potentials, the scaling in the sub-saturated region and the saturation voltage are well captured by the numerical model. Speelman et al. [100] had a similar kind of agreement with the experimental data, obtaining a ratio between the computed and measured saturation current of about 3. Also the saturation voltage and the ion current scaling in the sub-saturated regime were not captured by Speelman et al. [100]. To obviate to these mismatches, the authors of the paper made a sensitivity analysis of the ionization pre-exponential coefficients and ion transport properties in order to optimize the model parameters and match the experimental ion current profiles.

1.4 Accomplishments

In the following sections of this thesis, a detailed description of the mathematical model employed to describe the interaction of the impinging electric field with a laminar flame will be provided, highlighting the main assumptions and limitations of the present formulation. Afterwards, the results of a series of two-dimensional calculations involving a counterflow laminar flame impinged by an electric field will be presented analyzing the main features of the electrical response of the flame and showing a comparison with the results obtained experimentally on the same configuration [78]. The output of the detailed simulations will also be used to validate a one-dimensional flamelet model obtained mapping the governing equations of the problem in the mixture fraction space. At the end of the thesis, an FPV model formulated to increase the computational efficiency and to take into account for arbitrarily complex chemical mechanism will be proposed.

The main innovative contributions of this thesis are:

- An algorithm for the computation of multi-dimensional reacting flow, involving chemi-ionization and electric field induced transport, has been formulated and employed for the detailed simulation of a counterflow laminar flame.
- The physical phenomena involved in a counterflow diffusion flame impinged by an electric field have been analyzed using the axisymmetry approximation.
- A flamelet model in the mixture fraction space, that includes the electric diffusion effects, has been proposed. Such a model has shown the ability to recover the prediction of the detailed model, largely reducing the computational cost of the simulations.
- Thanks to the relatively low computational cost of the flamelet calculations, it has been possible to conduct a preliminary parametric investigations of the steady-state operating conditions of electrified counterflow flames.
- An FPV model for the simulation of electrified flames has been formulated and applied to the simulation of a lifted methane-air flame, quantitatively recovering the effects of the electric field on the flame liftoff present in the literature.
- This FPV model is completely independent of the complexity of the chemical mechanism employed for the prediction of the species production rates allowing the use of an arbitrarily complex set of reactions without any computational cost increase.
- Taking advantage of the averaging procedures present in the FPV model in order to compute the charged species properties, the computational cost of each simulation has been reduced up to 40 times with respect to the standard method.

Chapter 2

Mathematical model

This chapter provides a description of the basic mathematical laws and physical relations involved in the formulation of the mathematical models used in the following chapters. At first, basic transport equations will be listed in their complete form in order to highlight the main assumptions made during the mathematical description of the phenomenon. Then a non-dimensional form of the equations will be provided defining the main dimensionless groups that regulate the involved phenomena. The chapter will be completed with the description of the algorithm employed for the definition of the transport properties of the chemical species and with the definition of the two main chemi-ionization mechanisms used during all the computations described in this thesis.

2.1 Transport equations

All the mathematical models used in the simulations presented in this thesis are based on the conservation equations of mass, momentum, species mass fraction and energy that, in the order, read as:

$$\frac{\partial \rho}{\partial t} + \nabla \cdot (\rho \mathbf{u}) = 0; \tag{2.1}$$

$$\frac{\partial \rho \mathbf{u}}{\partial t} + \nabla \cdot (\rho \mathbf{u}\mathbf{u}) = -\nabla p + \nabla \cdot \overline{\overline{\sigma}} + \rho \sum_{i=1}^{N_s} Y_i \mathbf{g}_i; \tag{2.2}$$

$$\frac{\partial \rho Y_i}{\partial t} + \nabla \cdot (\rho \mathbf{u} Y_i) = -\nabla \cdot (\rho \mathbf{V}_i Y_i) + \rho \dot{\omega}_i; \tag{2.3}$$

$$\begin{aligned} c_p \frac{\partial \rho T}{\partial t} + c_p \nabla \cdot (\rho \mathbf{u} T) = & \nabla \cdot (\lambda \nabla T) + \frac{\partial p}{\partial t} + \mathbf{u} \cdot \nabla p + \overline{\overline{\sigma}} : \mathbf{u} - \rho \sum_{i=1}^{N_s} h_i \dot{\omega}_i \\ & - \rho \sum_{i=1}^{N_s} Y_i \mathbf{V}_i \cdot \nabla h_i + \rho \sum_{i=1}^{N_s} Y_i \mathbf{g}_i \cdot \mathbf{V}_i \\ & - \mathcal{R} T \sum_{i=1}^{N_s} \sum_{j=1}^{N_s} \frac{X_j \alpha_{T,i}}{W_i \alpha_{ij}} (\mathbf{V}_i - \mathbf{V}_j). \end{aligned} \tag{2.4}$$

where: ρ is the mixture density; $\mathbf{u}$ is the velocity vector; p is the pressure; N_s is the number of species composing the mixture; $\mathbf{g}_i$ are the accelerations relative to the body force acting on the each species; Y_i are the species mass fractions; X_i are the species molar fractions; W_i are the species molar mass; $\mathbf{V}_i$ are the species diffusion velocities; $\dot{\omega}_i$ are the chemical source term of the transported species; T is the mixture temperature; c_p is the mixture averaged specific heat capacity, computed as

$c_p = \sum_{i=1}^{N_s} Y_i c_{p_i}$ where c_{p_i} are the specific heat capacities of each species evaluated as function of the temperature; λ is the mixture thermal conductivity; $\mathcal{R}$ is the universal gas constant; α_{ij} are binary diffusivities between the species i and j; $\alpha_{T,i}$ are the species thermal diffusivities. The Left Hand Sides (LHSs) of all the four equations are composed only of the classical time derivative and convective flux terms. The Right Hand Side (RHS) of the momentum conservation equation (Equation (2.2)) features, in order of appearance, the effect of the pressure gradient, the local shear stress flux and the volumetric source and sink terms due to the body forces applied to the species that compose the mixture. The local shear stress tensor $\overline{\overline{\sigma}}$ is modeled as

$$\overline{\overline{\sigma}} = 2\rho \left[\nu \overline{\overline{S}} - \nu_b (\nabla \cdot \mathbf{u}) \overline{\overline{I}}\right], \qquad \text{with} \qquad \overline{\overline{S}} = \frac{1}{2}\left[\nabla \mathbf{u} + (\nabla \mathbf{u})^T\right], \tag{2.5}$$

ν and ν_b being the molecular and bulk kinematic viscosities, respectively. The RHS of the species mass fraction conservation equations (2.3) is composed of the divergence of the diffusive flux of the species in the mixture and of the chemical production term. According to Williams [114], the complete derivation of the diffusion velocity vector, based on the conservation of the particles momentum arguments, leads to the following implicit expression:

$$\begin{aligned} \nabla X_i =& \sum_{j=1}^{N_s} \frac{X_i X_j}{\alpha_{ij}} (\mathbf{V}_i - \mathbf{V}_j) + X_i \left(\frac{W_i}{W} - 1\right) \nabla \ln(p) + \frac{\rho}{p} \sum_{j=1}^{N_s} Y_i Y_j (\mathbf{g}_i - \mathbf{g}_j) \\ &+ \sum_{j=1}^{N_s} \frac{X_i X_j}{\rho \alpha_{ij}} \left(\frac{\alpha_{T,i}}{Y_i} - \frac{\alpha_{T,j}}{Y_j}\right) \nabla \ln(T); \end{aligned} \tag{2.6}$$

in particular, the RHS of the Equation (2.6) contains, in order of appearance, the Stefan-Maxwell diffusion and the diffusion fluxes due to the pressure gradient, to the body forces and to the temperature gradient (Soret effect). The averaged mixture molar mass (W) is computed as

$$W = \left(\sum_{i=1}^{N_s} \frac{Y_i}{W_i}\right)^{-1}, \tag{2.7}$$

whereas, the relation between the species mass fractions and molar fractions is

$$Y_i = \frac{W_i}{W} X_i. \tag{2.8}$$

The solution of this linear system in Equation (2.6) for each point of the computational grid would lead to the determination of the local diffusion velocity, but this procedure is usually avoided when the number of transported species is very high because of its computational cost [90]. The species production term ($\dot{\omega}_i$) is instead evaluated as

$$\dot{\omega}_i = W^{-1} \sum_{j=1}^{N_r} \left[W_i (\nu'_{j,i} - \nu''_{j,i}) \left(K_{fr,j} \prod_{k=1}^{N_p} X_i^{\nu'_{j,i}} - K_{br,j} \prod_{k=1}^{N_p} X_i^{\nu''_{j,i}} \right) \right] \tag{2.9}$$

where: N_r is the number of reactions present in the chemical mechanism; $\nu'_{j,i}$ and $\nu''_{j,i}$ are the stoichiometric coefficients of the species i in the reaction j as reactant or product, respectively; $K_{fr,j}$ and $K_{br,j}$ are the forward and backward reaction rates and are related to each other by the equilibrium constant of the reaction ($K_{eq,j}$) with the equation:

$$K_{eq,j} = \frac{K_{fr,j}}{K_{br,j}}. \tag{2.10}$$

$K_{eq,j}$ is determined using the Gibbs free energy of the reaction. Further details about the number of reactions and their rates will be provided later in Section 2.3 of this chapter. The temperature conservation equation (Equation (2.4)) contains in its RHS the terms accounting for: the thermal conduction (Fourier law); the effect of the change of the thermodynamic pressure on the internal energy; the contributions of the work done by the pressure gradient and by viscous dissipation acting on the internal energy; the heat release rate due to the chemical production of the transported species; the enthalpy flux due to the species diffusion; the internal energy component of the work done by the body forces acting on the species; and the heat flux due to the density gradient (Dufour effect). The species specific enthalpy (h_i) used in this equation is evaluated as

$$h_i(T) = h(T_0) + \int_{T_0}^{T} c_{p_i}(\theta) d\theta. \tag{2.11}$$

It is noteworthy that, for mass conservation arguments, the summation of all the mass fraction equations has to recover the mass conservation equation (2.1), therefore

$$\sum_{i=1}^{N_s} Y_i = 1, \tag{2.12}$$

$$\sum_{i=1}^{N_s} \dot{\omega}_i = 0, \tag{2.13}$$

$$\sum_{i=1}^{N_s} Y_i \mathbf{V}_i = \mathbf{0}. \tag{2.14}$$

2.1.1 Main simplifying assumptions

This section reports all the assumptions made about the constitutive properties of the fluid and the electrical and hydrodynamic regime of the flow in order to close the problem formulation defined by the equations in the previous section and to reduce the computational effort needed to perform the calculations.

1. *Low Mach number:* all the configurations analyzed in this work involve the solution of flows characterized by a maximum ratio between the local fluid velocity and speed of sound (also known as Mach number) much lower than one. In general, the pressure field can be decomposed in a mean value, which will also be called thermodynamic pressure (p_{th}), and an oscillation field ($p = p_{th} + p'$). Considering that the effect of the local pressure fluctuations on the thermodynamic state of the fluid scales as the Mach number squared, the thermodynamic component of the pressure is the only one retained in the calculations concerning the energy of the systems (equation of state, species transport properties, ...) in all the calculations presented in this work. This is equivalent to neglect compressibility effects of the mixture. The fluctuating field is instead used in the evaluation of the effects of hydrodynamic pressure on the momentum. Thanks to the spatial homogeneity of the thermodynamic pressure, it is

trivial to show that $\nabla p = \nabla p'$. Moreover, in this kind of flow the Eckert number (Ec, see Section 2.1.2 for the definition) is very small (Ec $\ll 1$) and, for this reason, the hydrodynamic pressure effects on the internal energy can be neglected.

2. *Viscous heating:* it can be easily shown that the amount of internal energy produced by the viscous heating ($\overline{\overline{\sigma}} : \mathbf{u}$) scales with the ratio (Ec/Re), where Re is the Reynolds number (defined in Section 2.1.2). The present work deals with the modeling of laminar flows that have a Reynolds number of the order $\mathcal{O}(100)$. Since Ec $\ll 1$, it is possible to consider the viscous heating as a minor component of the Equation (2.4) and, therefore, to neglect it during the calculations.

3. *Ideal gas:* considering that the present work deals with single-phase flow of a mixture composed of multiple species in the gaseous state, it has been decided to use the ideal gas law as constitutive equation of the fluid. For this reason the well-known ideal gas equation of state, namely

$$p_{th} = \rho \frac{\mathcal{R}}{W} T, \tag{2.15}$$

has been used in order to relate the mixture density with the thermodynamic pressure, temperature and mixture composition.

4. *Bulk viscosity:* the identity between the thermodynamical and mechanical pressure acting on the elemental fluid control volume requires that the viscous stress tensor should not have any isotropic component, therefore the trace of $\overline{\overline{\sigma}}$ has to be zero. This assumption leads to the Stokes' hypothesis [106] that equates the bulk viscosity (ν_b) in Equation (2.5) to one-third of the molecular viscosity.

5. *Electrostatic regime:* the electromagnetic effects produced by the imposed electric field and by the electric charges moving inside the computational domain should be modeled using the entire set of the Maxwell equations. On the other hand, considering that: i) in all the configurations examined in this thesis a constant DC voltage is applied; ii) no magnetic fields are applied to the systems; iii) the expected ion-current is not strong enough to generate a significant magnetic field; the system can be considered in the electrostatic regime and, therefore, the Gauss law is the only relation retained from the set of Maxwell equations. In fact, the electric potential (Φ) is computed solving the following equation

$$\nabla^2 \Phi = -\frac{\rho_q}{\epsilon_0}, \tag{2.16}$$

where ϵ_0 is the electric permittivity of free-space. In this formulation, $\rho_q = \sum_{i=1}^{N_s} \rho_{q,i}$ denotes the sum of the individual charge densities

$$\rho_{q,i} = \rho N_a e \frac{\mathcal{S}_i Y_i}{W_i}. \tag{2.17}$$

where: N_a is the Avogadro number; e is the elementary electric charge value; $\mathcal{S}_i$ is the number of elementary charges, with $\mathcal{S}_i = 0$ for neutral species, and $\mathcal{S}_i > 0$ and $\mathcal{S}_i < 0$ for positively and negatively charged species, respectively.

Consequently, the electric field ($\mathbf{E}$) is computed as $\mathbf{E} = -\nabla\Phi$. Consistently with this approximation, only the electrostatic component of the Lorentz force is considered. In fact, the specific body force applied to each species ($\mathbf{g}_i$) considered in this work is expressed as

$$\mathbf{g}_i = \mathbf{g} + N_a e \frac{\mathcal{S}_i}{W_i}\mathbf{E}; \tag{2.18}$$

the first term of this equation takes into account the gravitational force applied to all the chemical species that compose the mixture ($\mathbf{g}$ is the gravitational acceleration), whereas the second term represents the electric force applied to the charged particles.

6. *Dufour effect:* in flows involving exothermic reactions, such as those studied in the present work, the heat flux due to the Dufour effect is negligible [114, p. 644]. For this reason, it will not be considered in the temperature transport equation (2.4).

7. *Diffusion velocity:* as already mentioned in the previous section, the solution of the implicit linear problem in Equation (2.6) for each point of the computational grid poses strong restrictions on the number of species that can be considered in the chemical mechanism. Considering the detail of the chemical reaction mechanism required in order to have a quantitative accurate prediction of the chemi-ionization, it has been decided to approximate the diffusion velocity with the following equation:

$$\mathbf{V}_i = -\frac{\alpha_i}{X_i}\nabla X_i + \sum_{j=1}^{N_s}\frac{Y_j}{X_j}\alpha_j\nabla X_j + \mathcal{S}_i k_i \mathbf{E} - \sum_{j=1}^{N_s}\mathcal{S}_j Y_j k_j \mathbf{E}, \tag{2.19}$$

where k_i and α_i are the mixture averaged species electrical mobility and molecular diffusivity, respectively. The first term represents the molecular diffusion computed as suggested by Curtiss and Hirschfelder [22], the second term is the correction term formulated by Coffee and Heimerl [20] in order to preserve the total mass of the mixture in a multicomponent mixture, the third term takes into account the charged species diffusion flux induced by the local electric field [81] and the last term enforces Equation (2.14) on the electric diffusion flux.

8. *Thermalized gas:* a common approximation used for the statistical description of the mixture in many laws of the chemistry is that the mixture is thermalized. This assumption consists in considering that the energy distribution functions of all the species contained in the mixture are Maxwell–Boltzmann distribution with the same mean. The mean energy of all the distributions corresponds to the mixture temperature. For instance, the Arrhenius equation used for the determination of the reaction rates in Equation (2.9), namely

$$K_{fr,j} = \mathcal{A}_j T^{n_j} \exp\left(-\frac{E_{a,j}}{\mathcal{R}T}\right), \tag{2.20}$$

where the pre-exponential coefficients ($\mathcal{A}_j$), the exponent of the temperature (n_j) and the activation energy ($E_{a,j}$) are properties of the reaction, is based on this assumption. However, the presence of an external electric field leads to

> the formation of the body forces on the charged species, as described by Equation (2.18). Because of their reduced mass, this force may become dominant in the conservation of the momentum of electrons, strongly increasing their kinetic energy. This effect is not only observable as an increase of the mean energy of the distribution, but also introduces distortions on the shape of the Electron Energy Distribution Function (EEDF). These distortions of the distribution are due to the activation of collisions where the electrons exchange a large amount of energy with the surrounding molecules. These collisions are called inelastic and super-elastic whether the electrons give or receive the energy from the other particles. Studies in the literature have demonstrated the importance of these phenomena in the chemical description of these systems [16–18, 21]. On the other hand, the calculation of the local EEDF based on the electric field and on the composition of the mixture requires the solution of a Boltzmann equation [92] for each point of the computational grid. This solution is computationally very expensive considering the number of energetic layers that must be used in order to accurately describe the EEDF and that the presence of the inelastic and super-elastic collisions makes the linear system resulting from the discretization of the Boltzmann equation non-diagonally dominant and therefore very difficult to be numerically resolved. For this reason, in conjunction with relatively small reduced electric field encountered in the analyzed flows [64], it has been decided to neglect the presence of non-thermal effects in the mixture, consistently with the majority of the numerical studies present in the literature about this topic [4, 5, 77, 91, 100, 101].

The simplified system of equations obtained applying the mentioned assumptions to the transport equations (2.1)-(2.4) reads as:

$$\frac{\partial \rho}{\partial t} + \nabla\cdot(\rho\mathbf{u}) = 0; \tag{2.21}$$

$$\frac{\partial \rho\mathbf{u}}{\partial t} + \nabla\cdot(\rho\mathbf{u}\mathbf{u}) = -\nabla p + \nabla\cdot\overline{\overline{\sigma}} + \rho\mathbf{g} + \rho_q\mathbf{E}; \tag{2.22}$$

$$\begin{aligned}\frac{\partial \rho Y_i}{\partial t} + \nabla\cdot(\rho\mathbf{u}Y_i) =& \nabla\cdot\left[\rho Y_i\left(\frac{\alpha_i}{X_i}\nabla X_i - \sum_{j=1}^{N_s} Y_j\frac{\alpha_j}{X_j}\nabla X_j\right)\right] + \rho\dot{\omega}_i\\ &- \nabla\cdot\left[\rho Y_i\left(\mathcal{S}_i k_i - \sum_{j=1}^{N_s} Y_j\mathcal{S}_j k_j\right)\mathbf{E}\right];\end{aligned} \tag{2.23}$$

$$\begin{aligned}\frac{\partial \rho T}{\partial t} + \nabla\cdot(\rho\mathbf{u}T) =& \frac{1}{c_p}\nabla\cdot(\lambda\nabla T) - \frac{\rho}{c_p}\sum_{i=1}^{N_s} h_i\dot{\omega}_i + \frac{1}{c_p}\frac{\partial p_{th}}{\partial t}\\ &+\frac{\rho}{c_p}\sum_{i=1}^{N_s}\nabla h_i\cdot Y_i\left[\frac{\alpha_i}{X_i}\nabla X_i - \sum_{j=1}^{N_s}\frac{Y_j}{X_j}\alpha_j\nabla X_j - \left(\mathcal{S}_i k_i - \sum_{j=1}^{N_s} Y_j\mathcal{S}_j k_j\right)\mathbf{E}\right]\\ &-\frac{1}{c_p}\mathbf{E}\cdot\sum_{i=1}^{N_s}\rho_{q,i}\left[\frac{\alpha_i}{X_i}\nabla X_i - \sum_{j=1}^{N_s}\frac{Y_j}{X_j}\alpha_j\nabla X_j - \left(\mathcal{S}_i k_i - \sum_{j=1}^{N_s} Y_j\mathcal{S}_j k_j\right)\mathbf{E}\right];\end{aligned} \tag{2.24}$$

$$p_{th} = \rho\frac{\mathcal{R}}{W}T; \tag{2.25}$$

$$\nabla\cdot\mathbf{E} = -\nabla^2\Phi = \frac{\rho_q}{\epsilon_0}. \tag{2.26}$$

2.1.2 Dimensionless formulation

The present section deals with the derivation of the dimensionless form of Equations (2.21)-(2.26) in order to point out the major non-dimensional groups characterizing the impingement of an electric field with a flame. At first, a dimensionless version of the differential operators is derived using a reference length (L_{ref}) and velocity (u_{ref}), namely

$$\frac{\partial}{\partial t^*} = \frac{L_{ref}}{u_{ref}}\frac{\partial}{\partial t}; \qquad \nabla^* = L_{ref}\nabla.$$

Afterwards, the following dimensionless variables and mixture properties are defined (likewise the definition of L_{ref} and u_{ref}, the subscript $(\cdot)_{ref}$ is used to define the reference value for the quantity):

$$\begin{array}{llll}
\mathbf{u}^* = \dfrac{\mathbf{u}}{u_{ref}}; & \rho^* = \dfrac{\rho}{\rho_{ref}}; & \mathbf{E}^* = \dfrac{\mathbf{E}L_{ref}}{\Delta\Phi_{ref}}; & W_i^* = \dfrac{W_i}{W_{ref}}; \\
Y_i^* = \dfrac{Y_i}{Y_{i,ref}}; & \alpha_i^* = \dfrac{\alpha_i}{\alpha_{ref}}; & k_i^* = \dfrac{k_i}{k_{ref}}; & c_p^* = \dfrac{c_p}{c_{p,ref}}; \\
\lambda^* = \dfrac{\lambda}{\lambda_{ref}}; & h_i^* = \dfrac{h_i}{c_{p,ref}\Delta T_{ref}}; & \mathcal{R}^* = \dfrac{\mathcal{R}}{c_{p,ref}W}; & \mathbf{g}^* = \dfrac{\mathbf{g}}{|\mathbf{g}|}; \\
T^* = \dfrac{T}{\Delta T_{ref}}; & X_i^* = \dfrac{X_i}{Y_{i,ref}}; & p^* = \dfrac{p}{u_{ref}^2\rho_{ref}}; & \overline{\overline{\sigma}}^* = \dfrac{\overline{\overline{\sigma}}L_{ref}}{u_{ref}\nu_{ref}\rho_{ref}};
\end{array}$$

$$\rho_q^* = \sum_{i=1}^{N_s}\rho_{q,i}^* = \sum_{i=1}^{N_s}\frac{\rho_{q,i}}{\epsilon_0}\frac{L_{ref}^2}{\Delta\Phi_{ref}}; \qquad \dot{\omega}_i^* = \frac{\dot{\omega}_i W_{ref}}{Y_{i,ref}\rho_{ref}\mathcal{A}_{ref}}\exp\left(\frac{E_{a,ref}}{\mathcal{R}\Delta T_{ref}}\right).$$

Finally substituting the dimensionless quantities and operators in the Equations (2.21)-(2.26), it is possible to obtain the dimensionless version of the governing equations, namely

$$\frac{\partial\rho^*}{\partial t^*} + \nabla^*\cdot(\rho^*\mathbf{u}^*) = 0; \tag{2.27}$$

$$\frac{\partial\rho^*\mathbf{u}^*}{\partial t^*} + \nabla^*\cdot(\rho^*\mathbf{u}^*\mathbf{u}^*) = -\nabla^* p^* + \frac{1}{\mathrm{Re}}\nabla^*\cdot\overline{\overline{\sigma}}^* + \frac{1}{\mathrm{Fr}^2}\rho^*\mathbf{g}^* + \Xi\rho_q^*\mathbf{E}^*; \tag{2.28}$$

$$\begin{aligned}\frac{\partial\rho^* Y_i^*}{\partial t^*} + \nabla^*\cdot(\rho^*\mathbf{u}^* Y_i^*) =& \frac{1}{\mathrm{Re\ Sc}}\nabla^*\cdot(\rho^* Y_i^*\mathbf{D}_i^*) + \mathrm{Da}\ \rho^*\dot{\omega}_i^* \\ & - \frac{1}{\Theta}\nabla^*\cdot\left[\rho^* Y_i^*\left(\mathcal{S}_i k_i^* - \sum_{j=1}^{N_s} Y_{j,ref}Y_j^*\mathcal{S}_j k_j^*\right)\mathbf{E}^*\right];\end{aligned} \tag{2.29}$$

$$\begin{aligned}\frac{\partial\rho^* T^*}{\partial t^*} + \nabla^*\cdot(\rho^*\mathbf{u}^* T^*) =& \frac{1}{\mathrm{Re\ Pr}}\frac{1}{c_p^*}\nabla^*\cdot(\lambda^*\nabla^* T^*) - \frac{\rho^*}{c_p^*}\mathrm{Da}\sum_{i=1}^{N_s} Y_{i,ref}h_i^*\dot{\omega}_i^* \\ & + \frac{\rho^*}{c_p^*}\sum_{i=1}^{N_s} Y_{i,ref}Y_i^*\left[\frac{\mathbf{D}_i^*}{\mathrm{Re\ Sc}} - \left(\mathcal{S}_i k_i^* - \sum_{j=1}^{N_s} Y_{j,ref}Y_j^*\mathcal{S}_j k_j^*\right)\frac{\mathbf{E}^*}{\Theta}\right]\cdot\nabla^* h_i^* \\ + \frac{\mathrm{Ec}}{c_p^*}\frac{\partial p_{th}^*}{\partial t^*} - \frac{\Xi\ \mathrm{Ec}}{c_p^*}\sum_{i=1}^{N_s}\rho_{q,i}^* & \left[\frac{\mathbf{D}_i^*}{\mathrm{Re\ Sc}} - \left(\mathcal{S}_i k_i^* - \sum_{j=1}^{N_s} Y_{j,ref}Y_j^*\mathcal{S}_j k_j^*\right)\frac{\mathbf{E}^*}{\Theta}\right]\cdot\mathbf{E}^*;\end{aligned} \tag{2.30}$$

$$p_{th}^* = \frac{1}{\mathrm{Ec}}\rho^*\mathcal{R}^* T^*; \tag{2.31}$$

$$\nabla^*\cdot\mathbf{E}^* = \rho_q^*; \tag{2.32}$$

where

$$\mathbf{D}_i^* = \frac{\alpha_i^*}{X_i^*}\nabla^* X_i^* - \sum_{j=1}^{N_s} Y_{j,ref}\frac{Y_j^*}{X_j^*}\alpha_j^* \nabla^* X_j^*.$$

The result of the non-dimensionalization procedure performed in this section is the definition of the dimensionless numbers that describe the phenomena involved in the flow:

- Reynolds number: $\mathrm{Re} = \dfrac{u_{ref}L_{ref}}{\nu_{ref}}$;
- Froude number: $\mathrm{Fr} = \dfrac{u_{ref}}{\sqrt{|\mathbf{g}|L_{ref}}}$;
- electric interaction parameter: $\Xi = \dfrac{\epsilon_0(\Delta\Phi_{ref})^2}{\rho_{ref}u_{ref}^2 L_{ref}^2}$;
- Schmidt number: $\mathrm{Sc} = \dfrac{\nu_{ref}}{\alpha_{ref}}$;
- ion wind number: $\Theta = \dfrac{u_{ref}L_{ref}}{\Delta\Phi_{ref}k_{ref}}$;
- Damköhler number: $\mathrm{Da} = \dfrac{L_{ref}}{u_{ref}}\dfrac{\rho_{ref}\mathcal{A}_{ref}}{W_{ref}}\exp\left(-\dfrac{E_{a,ref}}{\mathcal{R}\Delta T_{ref}}\right)$;
- Prandtl number $\mathrm{Pr} = \dfrac{\nu_{ref}c_{p,ref}\rho_{ref}}{\lambda_{ref}}$;
- Eckert number $\mathrm{Ec} = \dfrac{u_{ref}^2}{c_{p,ref}\Delta T_{ref}}$;

Two similarity parameters in the previous list are formulated for the first time in this work, at the best of the author's knowledge. The first is the electric interaction parameter (Ξ): it is a ratio between the characteristic convective acceleration of the flow and the electric force density. The nature of the proposed number is similar to the Stuart number (also known as magnetic interaction parameter), used in magnetohydrodynamics to relate the inertia of the flow with the magnetic force. The second dimensionless group that is proposed in this work is ion wind number (Θ): it relates the characteristic flow velocity to electric drift velocity of the ionized species.

2.2 Transport properties

This section describes the algorithm used to compute the mixture and species properties introduced in the previous section during the definition of the transport equations. The pure species dynamic viscosities (η_i) and binary diffusivities (α_{ij}) are evaluated using the standard kinetic theory equations proposed by Hirschfelder et al. [45]:

$$\eta_i = \frac{5}{16}\frac{\sqrt{\pi k_B T W_i/N_a}}{\pi\sigma_i^2\Omega_i^{(2,2)*}}; \tag{2.33}$$

and

$$\alpha_{ij} = \frac{3}{16}\frac{\sqrt{2\pi N_a k_B^3 T^3/W_{ij}}}{p_{th}\pi\sigma_{ij}^2\Omega_{ij}^{(1,1)*}}. \tag{2.34}$$

In the previous equations: k_B is the Boltzmann constant; σ_i is the Lennard–Jones collision diameter; σ_{ij} is the reduced Lennard–Jones collision diameter computed as $\sigma_{ij} = (\sigma_i + \sigma_j)/2$; W_{ij} is the reduced molar mass computed as $(W_i W_j)/(W_i + W_j)$. $\Omega_{ij}^{(1,1)*}$ and $\Omega_i^{(2,2)*}$ are the collision integrals, which represent the departure of collision energies and velocity distributions from the hard sphere model. They are functions of the reduced temperature $T_i^* = k_B T/\xi_i$ (for $\Omega_i^{(2,2)*}$) and $T_{i,j}^* = k_B T/\sqrt{\xi_i \xi_j}$ (for $\Omega_{ij}^{(1,1)*}$) and, in this work, they are computed using the the Stockmayer potentials given by Monchick and Mason [71]. The choice of using the Lennard–Jones/Stockmayer potentials represents a compromise solution between computational cost and physical accuracy. In fact, Han et al. [42] suggested that the (n, 6, 4) theory should be more appropriate for the prediction of the charged species transport properties in the presence of collisions with neutral species that have dipole moments. On the other hand, the need of reducing the complexity of the overall calculation has lead to use the Lennard-Jones/Stockmayer potentials for both charged and neutral species (except for electrons). Assessing the influence of this approximation is deferred to future works. For the neutral species, the Lennard–Jones collision diameter (σ_i), along with the potential well-depth (ξ_i) required to compute the collision integrals $\Omega_{ij}^{(1,1)*}$ and $\Omega_i^{(2,2)*}$, are read from the transport data provided with the GriMech 3.0 mechanism [98]. Moreover, the corresponding values for the heavy ions are approximated to be equal to those of similar neutral species (i.e., H_2O for H_3O^+, CO for HCO^+, O for O^-, O_2 for $O_2{}^-$ and OH for OH^-).

The thermal conductivity of each species (λ_i) is computed neglecting the effects of its geometry and using the expression for mono-atomic gases:

$$\lambda_i = \eta_i \left(c_{p_i} + \frac{5}{4} \frac{\mathcal{R}}{W_i} \right) \tag{2.35}$$

with η_i given by Eq. (2.33). The temperature dependence of the individual specific heats c_{p_i} are modeled using the NASA polynomials [67]. The polynomial coefficients for the neutrals species are provided with the GriMech 3.0 mechanism [98], on the other hand, those for the charged species have been extracted from the Burcat and Ruscic [13] database. The mixture averaged diffusivity for each species is evaluated using the expression proposed by Bird et al. [7]:

$$\alpha_i = \frac{1 - Y_i}{\sum\limits_{j=1, j\neq i}^{N_s} \frac{X_j}{\alpha_{ij}}}. \tag{2.36}$$

The mixture thermal conductivity and dynamic viscosity (η) are instead evaluated using the averaging rules proposed by Mathur et al. [66] and by Wilke [113], respectively:

$$\lambda = \frac{1}{2} \left[\sum_{i=1}^{N_s} X_i \lambda_i + \left(\sum_{i=1}^{N_s} \frac{X_i}{\lambda_i} \right)^{-1} \right]; \tag{2.37}$$

and

$$\rho\nu = \eta = \sum_{i=1}^{N_s} \frac{Y_i \eta_i}{\Delta_i} \tag{2.38}$$

where:

$$\Delta_i = \sum_{j=1}^{N_s} G_{ij} \frac{W_i}{W_j} Y_j; \tag{2.39}$$

$$G_{ij} = \frac{1}{\sqrt{8}} \left(1 + \frac{W_i}{W_j}\right)^{-\frac{1}{2}} \left[1 + \left(\frac{\eta_i}{\eta_j}\right)^{-\frac{1}{2}} \left(\frac{W_j}{W_i}\right)^{\frac{1}{4}}\right]^2. \tag{2.40}$$

The binary mobility of the considered ionized species (except for the electrons) is evaluated applying the Einstein relation [64]:

$$\frac{\alpha_{ij}}{k_{ij}} = \frac{k_B T}{e}. \tag{2.41}$$

The averaged species mobility is consequently computed using the Blanc's law [64]:

$$k_i = \left(\sum_{j=1}^{N_s} \frac{X_j}{k_{ij}}\right)^{-1}. \tag{2.42}$$

An important role in the electrical properties of a flame is played by the mobility of electrons k_{e^-}, in that its value determines the rate at which the electrons are drained from the flame in the subsaturated regime, and also influences the voltage and the amount of ion current measured at the electrodes at the saturation onset [100]. It should, however, be noted that the analytical and experimental determination of adequate mobility coefficients for diffusion flames is an active area of research. In this study, and in the absence of conclusive values for diffusion flames, the electron mobility k_{e^-} is set to a constant value. The value of the electron mobility has an important influence on the simulation cost, in that the larger k_{e^-} is, the shorter is the electric drift diffusion time scale of the electrons, and, consequently, the stiffer the numerical integrations become. This value has been chosen among those present in literature making a compromise between the calculation accuracy and the computational cost of the simulations. Consistently with this choice, the electron molecular diffusivity α_{e^-} is computed from the standard expression

$$\alpha_{e^-} = \frac{k_B k_{e^-} T}{e}. \tag{2.43}$$

As evidenced by Eqs. (2.33)- (2.43), the temperature is assumed to be the same for neutrals, ions and electrons, thereby neglecting non-thermalization effects, as is appropriate for the small reduced electric fields encountered in this study [64].

2.3 Chemistry modeling

The present section provides a description of the two chemical mechanisms used in all the calculations presented in this thesis. Afterwards, the difference between the two chemical mechanisms will be highlighted analyzing the ions mass fraction profiles produced in an unstrained premixed methane/air flame.

2.3.1 Reaction mechanism description

All the results presented in the following chapters have been obtained using two different chemical mechanisms. Both the mechanisms are based on the well-known

TABLE 2.1: Chemi-ionization mechanism proposed by Belhi et al. [4]. $\mathcal{A}_j$ is reported in $\mathrm{cm}^3/(\mathrm{mol\,s})$ and $E_{a,j}$ in kJ.

Num.	**Reaction**			$\mathcal{A}_j$	n_j	$E_{a,j}$	**Ref.**
1	$CH + O$	$\longrightarrow$	$HCO^+ + e^-$	2.512×10^{11}	0.00	7.12	[81]
2	$HCO^+ + H_2O$	$\longrightarrow$	$CO + H_3O^+$	1.506×10^{15}	0.00	0.00	[107]
3	$H_3O^+ + e^-$	$\longrightarrow$	$H_2O + H$	1.144×10^{17}	0.00	0.00	[82]

GriMech 3.0 [98] for the computation of the neutral species production rates. This detailed reaction mechanism is optimized to predict the natural gas combustion, including NO formation and reburn chemistry. It contains 325 reactions among 53 neutral species and it has shown very good agreement with the experimental data in a wide range of applications [105, 108, 111, 124]. However, the choice of chemical kinetics made above represents a compromise solution between accuracy and computational cost. As discussed in the introduction (Chapter 1) and as it will be shown in the comparison with the experimental data, this choice is most likely not the optimum one in terms of accuracy, since other more extensive mechanisms such as the ones in Refs. [69, 110] might improve the predictions of the CH and O radicals and consequently assist in reducing the discrepancies of order unity observed in the saturation current with respect to experimental results (i.e., see Sections 3.5.1 and 3.3 for further details). Those extended mechanisms would, however, incur a computational cost that is untenable with the present numerical method because of a number of additional species that would need to be transported. The two mechanisms employed in the present work differ for the chemi-ionization reactions.

The first chemi-ionization mechanisms is that proposed by Belhi et al. [4] and it is summarized in Table 2.1. It is probably the most reduced chemi-ionization reaction mechanism present in the literature and, in fact, it consists of only three irreversible reactions. The only ionization pattern considered by the mechanism is through the reaction (R1.1) presented in Section 1.3. The very high pre-exponential reaction rate and the null activation energy of the reaction 2 in the table guarantee that the produced HCO^+ is rapidly converted in H_3O^+, as suggested by Pedersen and Brown [81]. According to Prager et al. [91], the produced ions should recombine through the following dissociative recombination reactions:

$$\mathrm{H_3O^+ + e^- \longrightarrow H_2O + H;} \tag{R2.1}$$

$$\mathrm{H_3O^+ + e^- \longrightarrow OH + 2\,H;} \tag{R2.2}$$

$$\mathrm{H_3O^+ + e^- \longrightarrow OH + H_2;} \tag{R2.3}$$

$$\mathrm{H_3O^+ + e^- \longrightarrow O + H + H_2.} \tag{R2.4}$$

On the other hand, the large number of studies present in literature have suggested that the reaction (R2.1) is dominant respect to the others [46, 81, 123]. For this reason, this is the only recombination reaction reported in Table 2.1. In particular, the reaction parameters have been determined in order to match the global recombination rate measured by Peeters and Mahnen [82].

The second chemi-ionization mechanism has been proposed by the same authors [5] but considering the physical mechanisms leading to the formation of heavy

TABLE 2.2: Chemi-ionization mechanism proposed by Belhi et al. [5]. $\mathcal{A}_j$ is reported in $\mathrm{cm^3/(mol\,s)}$ or $\mathrm{cm^6/mol^2/s}$ depending on the number of reactants. $E_{a,j}$ is reported in kJ.

Num.	Reaction			$\mathcal{A}_j$	n_j	$E_{a,j}$	Ref.
1	$CH + O$	$\longleftrightarrow$	$CHO^+ + e^-$	2.512×10^{11}	0.0	7.12	[81]
2	$CHO^+ + H_2O$	$\longleftrightarrow$	$CO + H_3O^+$	1.506×10^{15}	0.0	0.00	[107]
3	$H_3O^+ + e^-$	$\longleftrightarrow$	$H_2O + H$	1.144×10^{17}	0.0	0.00	[82]
4	$O_2 + e^- + O$	$\longleftrightarrow$	$O_2{}^- + O$	3.627×10^{16}	0.0	0.00	[15]
5	$2\,O_2 + e^-$	$\longleftrightarrow$	$O_2{}^- + O_2$	1.523×10^{21}	-1.0	4.99	[15]
6	$O_2 + e^- + H_2O$	$\longleftrightarrow$	$O_2{}^- + H_2O$	5.077×10^{18}	0.0	0.00	[15]
7	$O_2 + e^- + N_2$	$\longleftrightarrow$	$O_2{}^- + N_2$	3.590×10^{21}	-2.0	0.58	[15]
8	$OH + e^- + H_2$	$\longleftrightarrow$	$OH^- + H_2$	1.088×10^{17}	0.0	0.00	[44]
9	$OH + e^- + H_2O$	$\longleftrightarrow$	$OH^- + H_2O$	6.528×10^{17}	0.0	0.00	[44]
10	$OH + e^- + O_2$	$\longleftrightarrow$	$OH^- + O_2$	4.350×10^{16}	0.0	0.00	[44]
11	$OH + e^- + N_2$	$\longleftrightarrow$	$OH^- + N_2$	4.350×10^{16}	0.0	0.00	[44]
12	$OH + e^- + CO$	$\longleftrightarrow$	$OH^- + CO$	8.160×10^{16}	0.0	0.00	[44]
13	$OH + e^- + CO_2$	$\longleftrightarrow$	$OH^- + CO_2$	1.632×10^{17}	0.0	0.00	[44]
14	$OH + e^- + CH_4$	$\longleftrightarrow$	$OH^- + CH_4$	3.264×10^{17}	0.0	0.00	[44]
15	$O + e^- + O_2$	$\longleftrightarrow$	$O^- + O_2$	3.627×10^{16}	0.0	0.00	[15]
16	$2\,O + e^-$	$\longleftrightarrow$	$O^- + O$	3.021×10^{17}	0.0	0.00	[103]
17	$O_2{}^- + OH$	$\longleftrightarrow$	$OH^- + O_2$	6.022×10^{13}	0.0	0.00	[44]
18	$O_2{}^- + O$	$\longleftrightarrow$	$O^- + O_2$	1.987×10^{14}	0.0	0.00	[15]
19	$O_2{}^- + H$	$\longleftrightarrow$	$OH^- + O$	1.084×10^{15}	0.0	0.00	[103]
20	$O^- + H_2$	$\longleftrightarrow$	$OH^- + H$	1.987×10^{13}	0.0	0.00	[107]
21	$O^- + CH_4$	$\longleftrightarrow$	$OH^- + CH_3$	6.022×10^{13}	0.0	0.00	[107]
22	$O^- + H_2O$	$\longleftrightarrow$	$OH^- + OH$	8.431×10^{14}	0.0	0.00	[15]
23	$O^- + CH_2O$	$\longleftrightarrow$	$OH^- + HCO$	5.601×10^{14}	0.0	0.00	[10]
24	$O^- + C_2H_6$	$\longleftrightarrow$	$OH^- + C_2H_5$	6.130×10^{15}	-0.5	0.00	[102]
25	$O_2{}^- + H_2$	$\longleftrightarrow$	$H_2O_2 + e^-$	6.022×10^{14}	0.0	0.00	[91]
26	$O_2{}^- + H$	$\longleftrightarrow$	$HO_2 + e^-$	7.226×10^{14}	0.0	0.00	[103]
27	$OH^- + O$	$\longleftrightarrow$	$HO_2 + e^-$	1.204×10^{14}	0.0	0.00	[10]
28	$OH^- + H$	$\longleftrightarrow$	$H_2O + e^-$	1.084×10^{15}	0.0	0.00	[107]
29	$OH^- + C$	$\longleftrightarrow$	$HCO + e^-$	3.001×10^{14}	0.0	0.00	[107]
30	$OH^- + CH$	$\longleftrightarrow$	$CH_2O + e^-$	3.001×10^{14}	0.0	0.00	[107]
31	$OH^- + CH_3$	$\longleftrightarrow$	$CH_3OH + e^-$	6.022×10^{14}	0.0	0.00	[107]
32	$O^- + C$	$\longleftrightarrow$	$CO + e^-$	3.011×10^{14}	0.0	0.00	[107]
33	$O^- + H$	$\longleftrightarrow$	$OH + e^-$	3.011×10^{14}	0.0	0.00	[107]
34	$O^- + H$	$\longleftrightarrow$	$H_2O + e^-$	4.215×10^{14}	0.0	0.00	[107]
35	$O^- + CH$	$\longleftrightarrow$	$HCO + e^-$	3.011×10^{14}	0.0	0.00	[107]
36	$O^- + CH_2$	$\longleftrightarrow$	$CH_2O + e^-$	3.001×10^{14}	0.0	0.00	[107]
37	$O^- + CO$	$\longleftrightarrow$	$CO_2 + e^-$	3.914×10^{14}	0.0	0.00	[107]
38	$O^- + O$	$\longleftrightarrow$	$O_2 + e^-$	8.431×10^{13}	0.0	0.00	[107]
39	$O^- + C_2H_2$	$\longleftrightarrow$	$CH_2CO + e^-$	7.226×10^{14}	0.0	0.00	[39]
40	$O^- + H_2O$	$\longleftrightarrow$	$H_2O_2 + e^-$	3.613×10^{11}	0.0	0.00	[103]

negative ions. In fact, the ionization and recombination patterns of this mechanism are exactly the same as in the previous case, but it includes 37 additional reversible reactions among 6 ionized species (H_3O^+, HCO^+, e^-, $O_2{}^-$, O^- and OH^-). Thirteen three-body electron attachment reactions (namely from the reaction 4 to 12 in Table 2.2), which can be summarized in the following forms

$$\mathrm{O_2 + e^- + M \longrightarrow O_2{}^- + M}, \tag{R2.5}$$

$$\mathrm{OH + e^- + M \longrightarrow OH^- + M}, \tag{R2.6}$$

$$\mathrm{O + e^- + M \longrightarrow O^- + M}, \tag{R2.7}$$

represent one of the three main interaction mechanisms leading to the formation of $O_2{}^-$, O^- and OH^- from the respective neutral molecules, where M is the collider. Two charge-exchange reactions (17 and 18 in Table 2.2) are included that account for extra formation of O^- and OH^- [39]. The third and last path for producing heavy negative molecules is provided by the charge transfer reactions with rearrangement (from 19 to 24). In these reactions, the $O_2{}^-$ and O^- interact with a neutral molecule, are responsible for the formation of charged particles that correspond to the combination of the two reactants. Electron detachment reactions from 25 to 40 provide a mechanism to free the electrons from the heavy molecules, which can then recombine with the hydronium through the reaction (R2.1).

The presence of the heavy negative ions in the second mechanism has two main effects on the electrical behavior of the flame. The first effect is due to the lower electrical mobility of the heavy negative charges with respect to the electrons. For this reason, the momentum exchange between the negative particles and the flow can be largely increased in the regions where the electrons attachment reaction rates are high. Moreover, the presence of the heavy negative particles increases the total amount of charge present in the mixture. This effect is due to the absence in the second mechanism of any charge recombination reaction between the heavy ions. In fact, the rate of these reactions is expected to be very small because their reactants are minor charged species that are not considered by this mechanism [5]. In this regard, the formation of the $O_2{}^-$, O^- and OH^- reduces the amount of free electrons present in the mixture, inhibiting the recombination reaction (R2.1).

For sake of simplicity, the mechanism of Belhi et al. [4] will be after referred in this work as mechanism "A", whereas that of Belhi et al. [5] as mechanism "B".

2.3.2 Comparison of the ionization mechanisms

Although a validation of these two mechanisms has been already provided in Belhi et al. [4, 5], the results for a stoichiometric unstrained flamelet of methane in air without any applied difference of potential are presented in order to further clarify the effects of the different chemi-ionization mechanisms. The calculations have been performed using the freely distributed C++ code FlameMaster V3.3.10 [87] and imposing the electrical neutrality of the mixture. This is a common approximation when no difference of potential is imposed, since it reduced the complexity of the problem avoiding the solution of the electric potential field and of the electron mass fraction equation. The local concentration of the electrons in the mixture is computed from the other charged species mass fractions in order to maintain the local

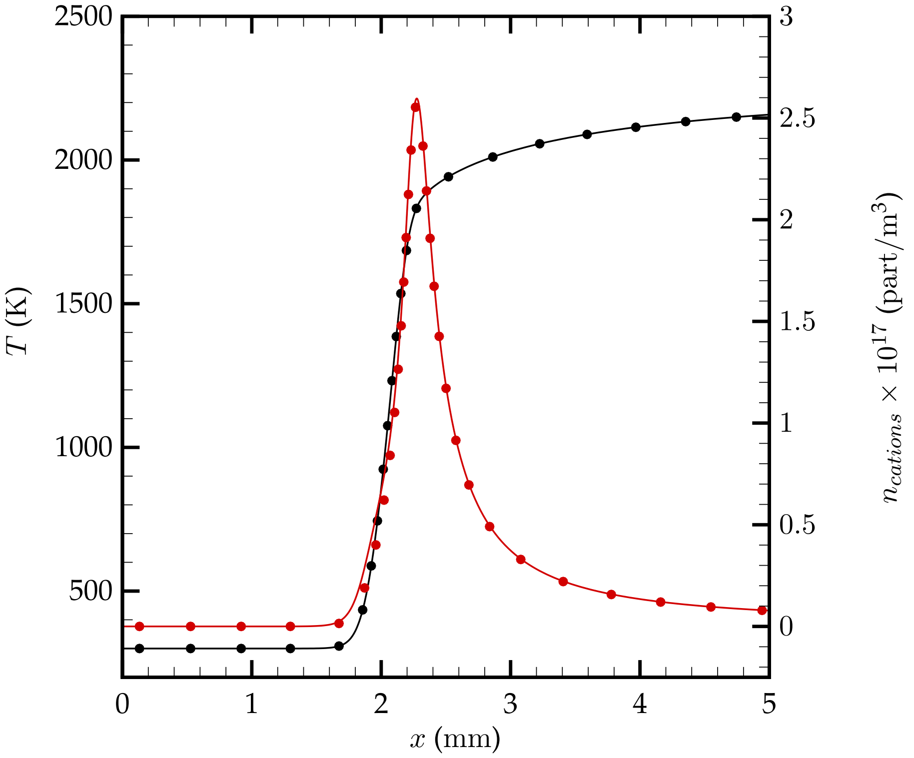

FIGURE 2.1: Unstrained premixed stoichiometric methane/air flamelet solution of temperature (black) and number density of the positive ions (red) for the mechanism "A" (symbols) and the mechanism "B" (continuous line).

electric charge density equal to zero. In particular,

$$n_{e^-} = n_{cations} - n_{anions}, \tag{2.44}$$

where the number of particles per unit of volume (n) is computed as

$$n_i = N_a \rho \frac{Y_i}{W_i}. \tag{2.45}$$

The Figure 2.1 shows temperature and total positive particle concentration profiles for both the mechanisms. The two temperature profiles coincide, demonstrating that the ionization mechanism has a negligible influence on the combustion process. Indeed, the charged species constitute only a minor part of the mixture and there are two or, in some cases, three orders of magnitude between the molar fractions of the combustion radicals and those of the anions and cations. On the other hand, the peak value of positive particle concentration, which, as expected, is located close to the flame-front for both mechanisms, is slightly lower for the reduced mechanism. The difference between the two peak values is about 1% and is due to the employment of the electrons in the production of the heavy charged species.

The Figure 2.2 shows the breakdown of the negative species produced by the two mechanisms, in order to observe their influence on the transport properties of the

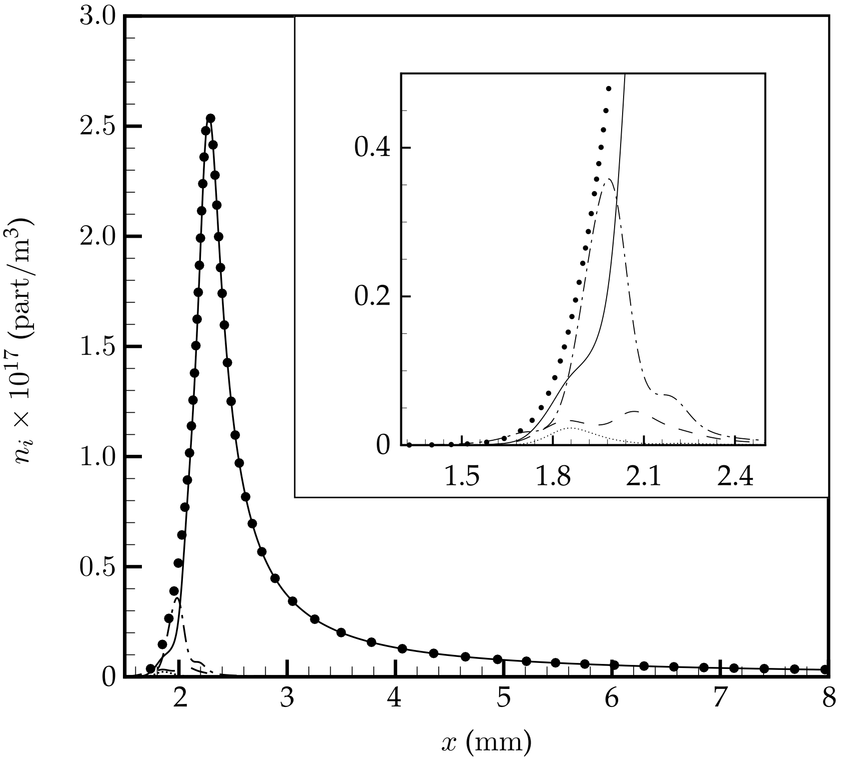

FIGURE 2.2: Unstrained premixed stoichiometric methane/air flamelet solution for the number density of electrons obtained using the mechanism "A" mechanism (symbols); number density of e$^-$ (——), of $O_2{}^-$ (- - -), of OH^- (-·-·-) and of O^- (·······) obtained using the mechanism "B". A close-up view of the lower left corner of the graph is shown by the inset.

charged particles. As expected the main negative species for the detailed mechanism is the electron, whose number density has a profile almost identical to that predicted by the other. The main difference between the two profiles is in the upstream part the flame front, which is shown in the inset. In this region, the dominant negative species in the mixture is OH^-, whose density is in some points even higher than that of the electrons. For this reason, the average mobility of the negative species is much lower for the mechanism that considers the heavy ions, entailing that this flame would have a different response to an applied electric field.

Chapter 3

Counterflow flame simulations

Counterflow laminar diffusion flames represent a cornerstone of nonpremixed turbulent combustion modeling [85]. However, the interactions of those with electric fields have been the focus of only a few studies to date. From the computational standpoint, and in contrast to premixed combustion, the effects of electric fields on counterflow diffusion flames have generally received much less attention, although progress has been recently made in simplified models for the interaction with axial electric fields [41]. The experimental works of Dayal and Pandya [24, 25] employed an electric field generated by two electrodes surrounding each orifice exit of the two opposing nozzles, and showed that the electric interaction shifted the ethyl alcohol/oxygen flame position by ∼5-6% toward the oxidizer side and increased the flame temperature by about 60 K from the nominal unelectrified values. The results were interpreted on the basis of a prevailing chemical effect induced by the electric field on the flame, in that free electrons, produced by the flame and energized by the electric field, enable dissociation reactions that would be impossible otherwise, thereby producing oxygen and hydrogen radicals that imbalanced the unelectrified flame structure. More recently, Park et al. [78] studied a similar experimental configuration but included Particle Image Velocimetry (PIV) visualizations of the flow, a technique that has been early recognized as challenging to deploy in electrified flames due to potential self-charging of the tracers (e.g., see discussion in Ref. [59, Ch. 7]). They used two mesh electrodes, which produced an electric field aligned with the axis of the burner that traversed the diffusion flame. The results included intensity/voltage curves revealing differences with respect to previously reported electric responses of premixed flames, such as the emergence of an overcurrent at intermediate voltages. Additionally, the PIV measurements suggested that the dominant electric effect pertained to the momentum coupling with the neutral particles in the form an ionic wind, which appeared to vastly modify the flow structure to the extent that the results suggested the occurrence of extra stagnation planes induced by the electric interactions. The numerical simulation of the experimental configuration employed by Park et al. [78] is the focus of the present chapter with the goal of elucidating the nature of those flow modifications.

In contrast with the current state-of-the-art in non-electrified laminar flames, for which a well-established combustion theory is available [114], a much less complete landscape appears when fundamental explanations of electrically induced phenomena in flames are sought in the literature. For instance, widespread theories of aerodynamic extinction of counterflow diffusion flames exist [62]. Similarly, the effects of the stretch, which are important for the propagation of turbulent premixed flames, have been widely characterized in earlier works [58]. However, how these fundamental theories need to be modified to account for electric effects remains an active topic of research. The success and tractability of theories for addressing these complex phenomena necessarily rely on the derivation of reduced chemical kinetic models for hydrocarbon combustion including ionic pathways, which represents a relatively unexplored problem.

A number of important barriers, which are clearly manifested also in the present study, hinder the development of theoretical and computational studies of electrified flames. These are related to: (a) the multi-scale nature of the electric/aero-thermo-chemical coupling phenomena, including the existence of a large disparity in time scales of electron and neutrals; (b) the complexities associated with the description of the molecular transport of charged species; and (c) the absence of accurate descriptions of ionic chemistry. Each of those barriers has a corresponding effect on the calculations. Firstly, the wide range of time scales typically leads to an exceedingly high computational cost, particularly in configurations such as the one treated here where the fluid mechanics of the bulk gas plays an important role. Specifically, the chemical kinetics of charged species and the motion of the electrons occur in characteristic time scales that are much shorter than those of convection and diffusion of the bulk gas, thereby causing severe numerical stiffness in the integration of the conservation equations. In the present investigation, a pseudo-time stepping algorithm is developed for a fast approach to a steady solution. Secondly, the molecular transport of charged species requires consideration of electric drift velocities, whose intensities are characterized by electric mobility coefficients that remain largely uncertain in the available literature and therefore lead to potentially different results. The present study employs values of the electron mobility recently updated by Bisetti and El Morsli [8] albeit for planar premixed flames, since studies related to this quantity are even more scarce for counterflow diffusion flames. Lastly, the ionization chemistry of electrified flames relies on the correct prediction of minor neutral intermediates and on the accurate representation of reaction rates for the chemical conversion of charged species. The former requires appropriate mechanisms for the neutrals that can predict minute quantities of radicals such as CH and O, which, in the methane flames addressed here, are believed to be responsible for initiating the ionized radical chains. This is typically attempted by using detailed mechanisms such as the GRIMech 3.0 [98] employed in this study, although this choice appears to be insufficient as suggested by the results presented below. The detailed mechanism for the neutrals requires coupling with a sub-mechanism for ionized species, such as the relatively complex one provided by Belhi et al. [5] for lifted jet diffusion flames and which has been used in the present work. To the best of the author's knowledge, the present study is the first one addressing these challenges in the context of counterflow diffusion flames and quantifying the resulting discrepancies with respect to experiments.

The numerical simulations presented in this chapter mainly focus on a counterflow burner, whose geometrical details and operating parameters are provided in Section 3.4, operated at a set of operating parameters involving a wide range of electric voltages and different mixture compositions. The results include axial distributions of electric potentials, charge densities, species molar fractions, electric forces, axial velocities, and scalar dissipation rates, along with intensity-versus-voltage curves and two-dimensional visualizations of flow streamlines and mass-fraction contours. From a fluid-mechanical standpoint, the present study suggests that the most important effect of the incident electric field is the generation of a bi-directional ionic wind that interacts with the two opposing jets of fresh reactants and modifies in a non-negligible way the strain-rate around the diffusion flame. This effect is particularly important for operating regimes involving air and pure fuel streams, in which the spatial shift of the flame from the mid-section of the burner, as required by stoichiometry, exacerbates the overall force imbalance. The main consequence is a decrease in the local strain rate, and consequently, a decrease in the local scalar dissipation rate, which becomes skewed toward the oxidizer side in a way that depends on the applied voltage.

The remainder of this chapter is structured as follows. The computational model employed in these simulations is described in Section 3.1, which includes the conservation equations and the numerical method used to integrate them. Sections 3.2 and 3.3 provide a supplementary validation against the simulations and experiments run by Goodings et al. [38, 39] and Speelman et al. [100], respectively, on premixed flames without and with an impinging electric field. The computational set-up of the counterflow burner is described in Section 3.4 along with the boundary conditions imposed to the transport equations. Finally, the simulation results are analyzed in Section 3.5, which includes comparisons between the present simulation results and the experiments by Park et al. [78].

3.1 Computational model

In order to limit as much as possible the number of assumptions applied during the calculation procedure, the results presented in this chapter are obtained using the governing equations of the physical system as they are reported in Equations (2.21)-(2.26). Since all the results presented in this chapter are related to steady-state laminar flames, the time derivatives present on the LHS of the Equations (2.21)-(2.24) are omitted from the present formulation. Moreover, the effect of buoyancy is also neglected in the RHS of the momentum conservation equation (2.22). The chemical kinetics of the ionized species is evaluated using the sub-mechanism proposed by Belhi et al. [5], therefore considering the presence of heavy negative ions in the mixture. In the absence of conclusive values for diffusion flames, the electron mobility k_{e^-} is set in all the following simulations to $0.4\,\mathrm{m}^2/(\mathrm{s\,V})$ as recommended by Bisetti and El Morsli [8] in the context of premixed CH_4-air flames, although the structures of those are expected to be different from the structures of the diffusion flames analyzed in this investigation. It is noteworthy that the value of k_{e^-} considered here is much larger than that used in earlier numerical studies [4, 5] and based on the scaling proposed by Delcroix and Bers [26] (i.e., $k_{\mathrm{e}^-} \sim 0.018\,\mathrm{m}^2/(\mathrm{s\,V})$). This aspect influences the simulation cost, being the electric drift diffusion time scale of the electrons inversely proportional to the electric mobility value, but also illustrates the large uncertainties associated with k_{e^-} that exist in the available literature.

3.1.1 Numerical method

The conservation equations provided above are integrated using a numerical method that consists of an extended version of the finite-difference fractional-step method described by Desjardins et al. [27], which has been employed in a number of earlier studies to compute chemically reacting flows [55, 70, 73]. The present study incorporates modifications to address electric interactions in combustion problems and to palliate the significant numerical stiffness caused by the ionic chemistry and electron transport as follows.

Motivated by the moderate Reynolds numbers associated with this configuration, this study aims at obtaining steady solutions to the conservation equations. However, although there is yet no clear general criteria available as to the voltage conditions under which flow unsteadiness may develop as a result of electrically-induced combustion instabilities, the experiments of Park et al. [78] suggest the existence of flame oscillations within a narrow interval of voltages near saturation conditions (i.e., $|\Delta\Phi_{ref}| \sim 1.1 - 1.3$kV for the case $Z_{st} = 0.5$), while steady conditions are observed for all other tested voltages. In this context, time-resolved simulations of unsteady behavior are challenging due to the small time steps of order $\Delta t = L\Delta x/(k_{\mathrm{e}^-}|\Delta\Phi_{ref}|) = \mathcal{O}(0.1\,\mathrm{ns})$ that would be required to advance the transport equation for the electrons, which, when compared to the characteristic flow times $A^{-1} \sim 2L_{ref}/u_{ref} = \mathcal{O}(10\,\mathrm{ms})$ under consideration, would result in an unfeasible large number of simulation steps of order 10^{-8}. For these reasons, and since the experimental voltage interval reported as prone to triggering flame instabilities is not directly probed by these simulations, in the present formulation unsteady effects are neglected, and each conservation equation is discretely advanced using a pseudo-time increment in order to efficiently arrive at a steady-state solution. The pseudo-time stepping algorithm adds an extra derivative with respect to a pseudo-time τ in the conservation Equations (2.21)-(2.24), each equation having its own pseudo-time step due to inherent limitations related to the participating time scales.

In addition to the fast transport of electrons, exceedingly short time scales of chemical conversion are also found within the set of reactions involving charged species. This also contributes to the stiffness of the employed system of partial differential equations requiring a special implicit treatment of the evolution of the chemical sources terms. For these reasons, the conservation equations for species (2.23) and thermal energy (2.24) are cast into the Ordinary Differential Equation (ODE) forms

$$\frac{d}{d\tau}[Y_i, T] = \frac{\nabla \cdot F^0}{\rho^0} + \left[\dot{\omega}_i, \frac{\dot{\omega}_T}{c_p}\right], \tag{3.1}$$

for $i = 1, \dots, N_s$, where $\dot{\omega}_T = -\sum_{i=1}^{N_s} h_i\dot{\omega}_i$ is the chemical heat release. In Equation (3.1), F^0 represents advective and diffusive fluxes based on the solution of the previous pseudo-time step, ρ^0 is the mixture density computed at the previous pseudo-time step, while the chemical sources ($\dot{\omega}_i$, $\dot{\omega}_T$) and c_p are evaluated implicitly. These equations are solved point-wise and coupled between all variables using a Newton-based implicit method over a pseudo-time interval determined as the maximum value among the pseudo-time step of the temperature ($\Delta\tau_T$) and of all the species mass fraction equations ($\Delta\tau_i$), $\Delta\tau = \max(\Delta\tau_T, \Delta\tau_1, \dots, \Delta\tau_{N_s})$. In particular, the pseudo-time step for the transport of thermal energy is chosen as $\Delta\tau_T = \min(\Delta x/|u_x|, \Delta r/|u_r|)$, whereas the corresponding value for the species transport is set to $\Delta\tau_i = \min(\Delta x/|u_x + \mathcal{S}_i k_i E_x|, \Delta r/|u_r + \mathcal{S}_i k_i E_r|)$, where the subindexes $_x$ and $_r$ are employed to denote velocity and electric-field components in the axial and radial directions, respectively. Note that the $\Delta\tau_i$ for the neutral species ($\mathcal{S}_i = 0$) is equal to $\Delta\tau_T$ because their electric drift velocities vanish. In this way, the intermediate solutions $Y_i(\tau + \Delta\tau)$ and $T(\tau + \Delta\tau)$ emerging from the numerical integration of (3.1) only account for the time evolution of the chemistry over the longest interval $\Delta\tau$ among all the different pseudo-time steps. These intermediate solutions are stored during the integration and are employed to define the species averaged chemical source terms

$$\overline{\dot{\omega}_i} = \frac{Y_i(\tau + \Delta\tau_i) - Y_i(\tau)}{\Delta\tau_i} - \frac{\nabla \cdot F^0}{\rho^0}, \tag{3.2}$$

```
Compute $\Delta\tau_i$;
Update $\nu$, $\alpha_i$, $k_i$, $\lambda$ and $c_p$;
Compute $\overline{\dot{\omega}_i}$;
for $i \leftarrow 1$ to $10$ do
    Advance $Y_i|_{\mathcal{S}_i=0}$ and $T$;
    for $j \leftarrow 1$ to $5$ do
        Advance $Y_i|_{\mathcal{S}_i\neq 0}$;
        Solve electric potential field;
    end
    Update $\rho$;
    Advance momentum conservation equations;
    Solve pressure field;
    Perform velocity correction;
end
```

FIGURE 3.1: Pseudo-time step algorithm.

with $\overline{\dot{\omega}_i} = \dot{\omega}_i$ being satisfied in the steady state. The averaged chemical heat release per mass unit is then computed as $\overline{\dot{\omega}_T} = -\sum_{i=1}^{N_s} h_i \overline{\dot{\omega}_i}$. The resulting computational cost of the implicit integration described above scales as N_s^2.

The algorithm employed for the advancement of all the governing equations of the system over a single pseudo-time step, shown in form of pseudo-code in Figure 3.1, starts with the evaluation of the $\Delta\tau_i$ and $\Delta\tau_T$. Afterwards, the transport properties are computed based on the previous pseudo-time step solution of the species and temperature transport equations and the averaged chemical source terms are obtained by the procedure described above. The conservation Equations (2.23)-(2.24) for the neutral species and thermal energy are then advanced using $\Delta\tau_T$ as pseudo-time step and incorporating the effects of the advection and diffusion fluxes, for which the semi-implicit formulation in Desjardins et al. [27] is used. The advection fluxes in the species and thermal-energy conservation equations are discretized with a third-order weighted essentially-non-oscillatory scheme. The rest of the differential terms are computed using a second-order centered scheme. The linear system derived from the discretization of transport equations is solved using an alternate-direction algorithm. A subiterative loop is then performed to solve the Poisson equation for the electrostatic potential in conjunction with the species transport equation for the charged particles (integrated over the corresponding pseudo-time steps $\Delta\tau_i$) to ensure consistency of the electric field with the electric charge. Note that the disparity in pseudo-time steps between the charged and neutral species acts as a diagonal preconditioning in the integration, with the ratio of the advection to drift velocities as the approximate values of the diagonal elements. At this point, the newly computed species mass-fractions and temperature fields are used to update the local mixture density field from the equation of state (2.15). Lastly, the momentum conservation equation is time advanced using the pseudo-time step $\Delta\tau_T$ (i.e., limited by the flow velocity) in conjunction with the solution to the Poisson

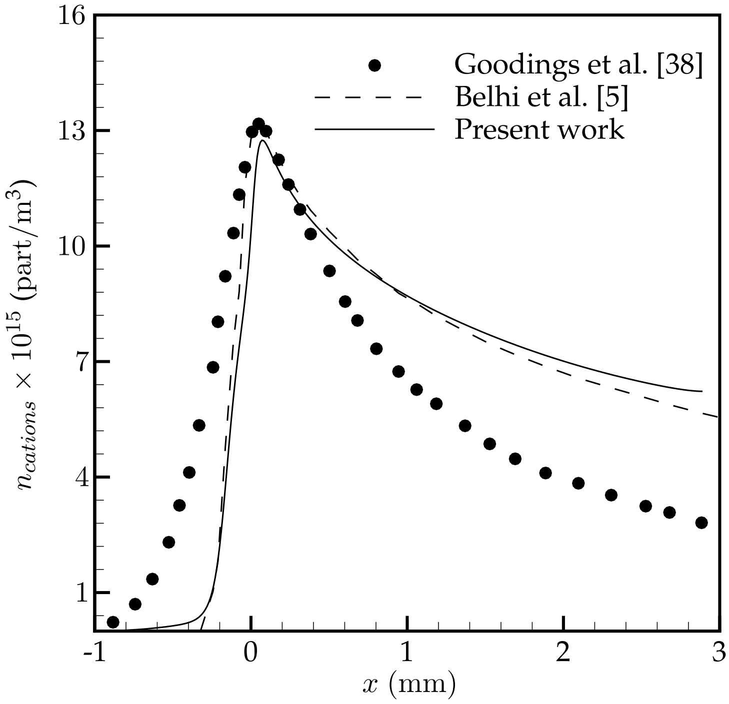

FIGURE 3.2: Comparison of the number density profiles for positive charged species obtained with the detailed model and the literature sources [5].

equation for the hydrodynamic pressure. Both Poisson equations for the hydrodynamic pressure and electrostatic potential are solved using a multi-grid preconditioned GMRES method. The algorithm steps covering from the advancement of the neutral species mass-fractions fields to the hydrodynamic pressure are repeated up to 10 times at each corresponding pseudo-time step in order to converge the density and keep the numerical method stable.

The convergence of the simulations is monitored using the L_∞ norm of a residual vector composed of the pseudo-time derivatives of the temperature, velocity components and species mass fractions, normalized with their maximum values based on the pseudo-time increment. Each of the 9 different computational cases described below in Section 3.5 involves approximately 70,000 CPU hrs on 128 cores.

3.2 One-dimensional validation without imposed electric field

The mathematical model and the numerical method described in the previous section have been tested with the one-dimensional test case of Goodings et al. [38, 39]. This configuration consists in premixed flame of methane with oxygen (ϕ = 0.2) that burns at atmospheric pressure. It has been chosen since it is one of the most common set of experimental data used by many studies in literature [42, 81, 91] in order to evaluate the predictions of chemical mechanisms. In this study, the results of the model described earlier will be compared with the results of Belhi et al. [5], obtained

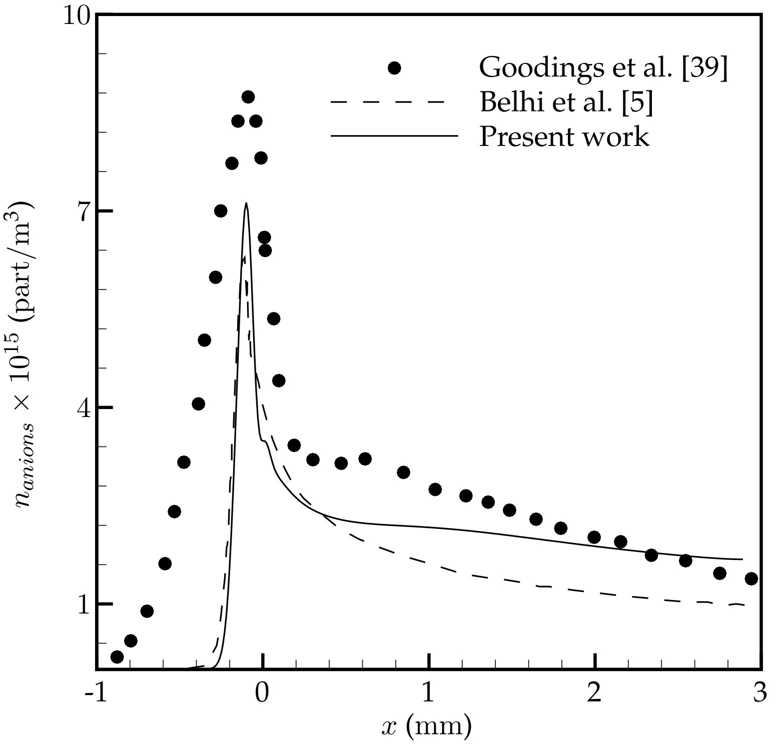

FIGURE 3.3: Comparison of the number density profiles for heavy anions obtained with the detailed model and the literature sources [5].

with the same chemical mechanism. It is noteworthy that in in the present work simulations the electrons are transported in the mixture, whereas they are computed to impose electrical neutrality in Belhi et al. [5].

The flame has been simulated using a one-dimensional $6\,\mathrm{mm}$ long domain discretized with 601 evenly spaced points. The calculation has been initialized imposing in the middle of the domain a sudden change of properties of the mixture (from unburned to burnt). The first point of the grid has been treated using a Dirichlet boundary condition imposing the laminar flame speed and the unburnt mixture properties, whereas the last point has been solved using a convective outlet.

Figures 3.2 and 3.3 show a comparison of the obtained profiles of positive and negative species (except for electrons) number density along the domain with the experimental data [38, 39] and the previous calculations [5]. The two numerically obtained profiles are in good agreement with each other for both the negative and the positive species. Looking at the positive species profile (Figure 3.2), marginal differences are present in the preheat zone ($-0.8\,\mathrm{mm} \leq x \leq -0.3\,\mathrm{mm}$), where the present work profiles are slightly higher and closer to the experimental data. On the other hand, the peak of the number density, corresponding to the reacting region of the flame, is better predicted by the dashed line which is slightly closer to the experimental data for the entire high-temperature region ($0.8\,\mathrm{mm} \leq x$). An opposite behavior is observed for the negative species. The two profiles are closer in the preheat region of the flame and they depart in the reacting layer. In this case, the continuous line (present study) presents a higher peak, closer to the experimental data, and a better prediction of the high-temperature region. The differences between the profiles are ascribed to the completely different behavior that the electrons have in the two considered simulations. In that proposed by Belhi et al. [5] the electrons are not transported, therefore their diffusivity does not come into play in the determination of the chemical equilibrium of the flame. On the other hand, the present study uses a transport equation for the electrons as for all the other species and takes into account the electric field generated by the difference in diffusive flux between the various charged species. This entails that the chemical equilibrium is now also determined by the diffusivity and electrical mobility of the electrons. Moreover, the present simulations predict the well-known higher potential region around the flame produced by the higher diffusive flux of the electrons (not shown here for sake or brevity). The predicted difference of potential is of about $1.0\,\mathrm{V}$, which is in good qualitative agreement with the measurement present in the literature [1, 68, 75].

3.3 One-dimensional validation with imposed electric field

In order to further verify the accuracy of the model presented in the previous sections, a series of simulations with different values of the electric potential has been carried out using the configuration proposed by Speelman et al. [100]. It consists of a burner stabilized premixed methane-air flame immersed in an electric field aligned with the flow direction. In particular, the flame is obtained using a cylindrical nozzle with a diameter of $6\,\mathrm{cm}$, which injects a flow at $298\,\mathrm{K}$ in an ambient at atmospheric pressure, with a velocity equal to the laminar burning velocity of the mixture. The exit of the burner is kept at a temperature of $350\,\mathrm{K}$ in order to stabilize the flame. Two electrodes are positioned at the exit of the nozzle and $1\,\mathrm{cm}$ downstream of it, respectively, applying a difference of electric potential, which is varied between $-250\,\mathrm{V}$ and $250\,\mathrm{V}$. With the purpose of validating the present model, it has been decided to analyze only the flame produced by a stoichiometric mixture among the various equivalence ratios analyzed by Speelman et al. [100]. This validation test case has been chosen because it has already been studied numerically using models similar to the present one and, therefore, it is easier to compare the behavior of the proposed approach not only with respect to the experimental data but also to state-of-the-art numerical models.

The simulation has been performed using a one-dimensional computational grid discretizing the region between the two electrodes by means of 800 evenly spaced points. At the upstream boundary, Dirichlet boundary conditions have been imposed for the velocity, neutral species, temperature and electric field. In particular, the temperature has been imposed equal to the burner temperature in order to generate the heat flux which stabilizes the flame. On the other hand, the downstream boundary has been modeled with a convective outflow condition for the flow and the neutral species. The electric potential, whose value is known, has been imposed with a Dirichlet condition. The charged-species boundary conditions are imposed using Dirichlet (equal to zero) or Neumann conditions depending on whether the species is attracted or repelled by the boundary, respectively [5, 100, 101].

Figure 3.4 shows the plot of electric current (I) versus the difference of potential applied to the electrodes. The continuous line represents the experimental values provided by Speelman et al. [100]. The dashed line is, instead, obtained by the same authors numerically, employing the chemical mechanism proposed by Belhi et al. [4] and a transport model based on the Stockmayer potentials in conjunction with the procedure proposed by Ern and Giovangigli [30]. The dash-dotted line provides the results of the model described in the previous sections.

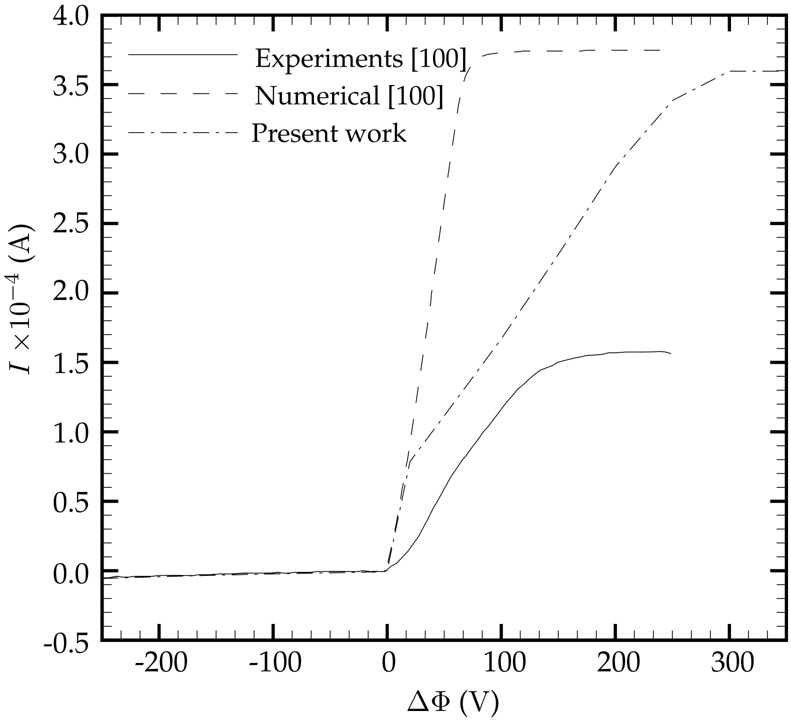

FIGURE 3.4: Electric current as function of the applied potential evaluated with the experiments, model of Speelman et al. [100] and with the present approach.

Both the numerical solutions presented in the figure predict an amount of charged species produced by the chemi-ionization process much higher than the experimental data. The reasons of this mismatch can be found in the neutral chemistry and in the chemi-ionization mechanisms. In fact, the entire charged-species production depends on the reaction (R1.1) and therefore is dominated by the presence in the mixture of the radical CH and O. These radicals have usually very small molar fractions if compared with the main species involved in the combustion process and a mechanism which is based on a reduced number of species such as the GriMech 3.0 [98] may not be adequate to accurately reproduce this very sensitive aspect of the system. Moreover, the ionization mechanism employed in this system also relies on a reduced number of species and reactions if compared with the mechanism of Prager et al. [91]. Despite these limitations, it has been decided to avoid the computational overhead associated with the use of more complex chemical mechanisms in view of employing the present model in a two-dimensional configuration.

Figure 3.4 also shows that the transport properties chosen for the charged species and the introduction of the negative ions in the mixture provide a more accurate evaluation of the sub-saturated regime of the flame with respect to the numerical results of Speelman et al. [100]. In fact, the present solution has a lower slope for the entire range of applied voltage reaching the saturation current between 250 V and 300 V. This value of saturation voltage is higher than the outcome of the experiments, but the overall electric current distribution represents a large improvement with respect to the calculations presented by Speelman et al. [100], especially in the

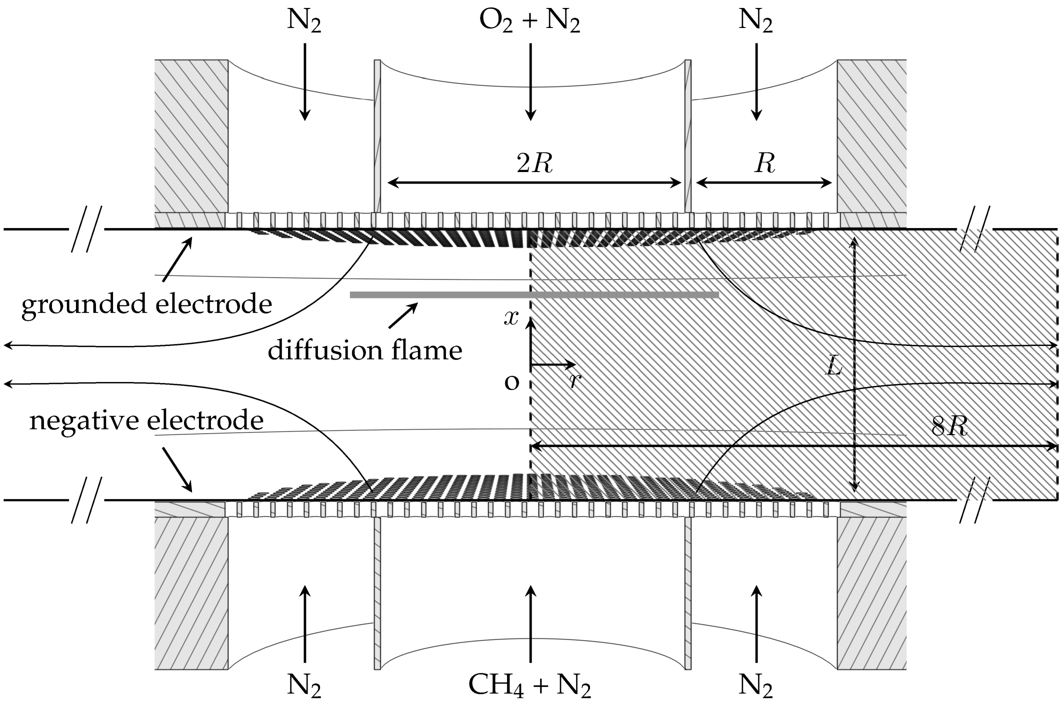

FIGURE 3.5: Sketch of the burner geometry and computational set-up (not to scale). The computational domain is denoted by the hatched region, while the two electrodes are represented by the horizontal thick solid lines. The axysimmetric coordinate system $\{x, r\}$ is placed at mid distance between the two orifice exits.

sub-saturated region.

3.4 Counterflow burner set-up

In this investigation, axisymmetric numerical simulation results are presented for electric-field interactions with counterflow laminar diffusion flames at atmospheric pressure in the configuration depicted in Figure 3.5, which is similar to that studied experimentally in Park et al. [78]. Specifically, the burner consists of two axisymmetric opposing nozzles surrounded by a sheath of molecular nitrogen (N_2). The cylindrical nozzles have a diameter $2R = 1\,\mathrm{cm}$ and are separated a distance $L = 1\,\mathrm{cm}$, as depicted in Figure 3.5. A cylindrical coordinate system is defined where x and r refer to the axial and radial distances, respectively, with the origin set at the geometric center of the gas layer between the two nozzles. The fuel nozzle exit is located at $x = -L/2$ and injects a gaseous methane (CH_4) diluted with N_2. Similarly, the oxidizer nozzle exit is placed at $x = -L/2$ and provides an oppositely flowing gaseous stream composed of a tunable mixture of molecular oxygen (O_2) and N_2. In the absence of electric interactions, both streams are ejected radially outwards after having merged forming a stagnation plane located at an axial distance from the origin that is solution of the problem. A diffusion flame is formed near the stagnation plane, within the mixing layer formed by the chemical reactants, that has a mostly flat shape near the axis. Electric interactions are enabled by two perforated circular

TABLE 3.1: Counterflow test case main parameters and dimensionless numbers.

Parameters	**Diluted configuration**	**Undiluted configuration**
X_i fuel jet	$X_{\mathrm{CH_4}} = 0.222$, $X_{\mathrm{N_2}} = 0.778$	$X_{\mathrm{CH_4}} = 1$
T fuel jet (K)	300	300
U fuel jet (m/s)	0.2	0.2
X_i oxidizer jet	$X_{\mathrm{O_2}} = 0.527$, $X_{\mathrm{N_2}} = 0.473$	$X_{\mathrm{O_2}} = 0.274$, $X_{\mathrm{N_2}} = 0.746$
T oxidizer jet (K)	300	300
U oxidizer jet (m/s)	0.2	0.2
$\Delta\Phi_{ref}$ (kV)	0.0-2.0	0.0-2.4
Z_{st}	0.5	0.07
A (1/s)	40	40
Re_L	252	252
Ξ	0.0-3.62	0.0-5.39

electrodes located at $x = \pm L/2$ covering each nozzle exit and extending radially outwards to 8 times the radius of the main injection orifices. A DC voltage difference is applied between a grounded anode at $x = +L/2$ and a cathode at $x = -L/2$, resulting in an axial electric field primarily directed from the oxidizer to the fuel side. The involved velocities are much smaller than the speed of sound and warrant moderately large Reynolds numbers within the laminar regime, in such a way that the flow remains axisymmetric and mostly steady with some exceptions in particular cases which are outlined below.

The computations presented in this study use the same geometry and operation parameters as the experiments of Park et al. [78]. The computations are conducted on an axisymmetric $\{r, x\}$ domain given by $-L/2 \leq x \leq +L/2$ and $0 \leq r \leq 8R$. The grid is Cartesian and uniformly meshed with $N_x \times N_r = 256 \times 512$ points in the axial and radial directions, respectively, which were observed to be effective in resolving the reaction layer. The resulting grid spacings are $\Delta x = L/N_x = 39\,\mu\mathrm{m}$ and $\Delta r = 8R/N_r = 78\,\mu\mathrm{m}$.

The upper ($x = +L/2$) and lower ($x = -L/2$) nozzles inject, respectively, O_2/N_2 and CH_4/N_2 mixtures whose relative compositions can be varied to study the effect of shifting the flame position in composition and physical spaces. In particular, two sets of mixtures are addressed in this study. The first set consists of a 27.4% O_2 / N_2 (on a molar basis) oxidizer mixture flowing against a pure CH_4 fuel stream, which renders a stoichiometric mixture fraction $Z_{st} = 0.07$. Conversely, the second set is based on a fuel-leaner flow whereby a 52.7%O_2 / N_2 oxidizer mixture is employed along with a 22.2%CH_4 / N_2 diluted fuel mixture, which gives $Z_{st} = 0.50$, in such a way that the flame is shifted toward the negative electrode. In both cases, the gases are injected at temperature $T = 300\,\mathrm{K}$ at an axial velocity $U = 20\,\mathrm{cm/s}$, thereby producing a characteristic strain rate $A \sim 2U/L = 40\,\mathrm{s}^{-1}$. The associated Reynolds number is $\mathrm{Re}_L = 2UL/\nu_{ref} \sim 252$ in both cases, where ν_{ref} is the kinematic diffusivity of the oxidizer stream, which in principle warrants a mostly laminar steady flow in the burner. Near the stagnation plane created by the two opposing streams, a convective-diffusive mixing layer of characteristic thickness $\delta_m/L = \mathrm{Re}_L^{-1/2} = 0.063$ is formed, within which combustion chemical reactions take place. This mixing layer is resolved by $\delta_m/\Delta x \sim 16$ grid points across. It should be noted that this estimate for δ_m is based on ν_0 and therefore does not account for temperature-dependent effects on the kinematic viscosity, which tend to thicken the mixing layer. The main configuration parameters and dimensionless numbers are reported in Table 3.1.

In the experiments, the nozzles are mounted downstream of convergent sections that reaccelerate the flow and decrease the thickness of the boundary layers at the injection planes. As a result, in the computations, the inflow profiles of velocity are assumed to be uniform. Similar cross-sectional uniformity at injection is assumed for the temperature and composition fields. Standard convective outflow conditions are employed at the outlet plane of the computational domain.

The fuel and oxidizer nozzles are placed concentrically inside two other cylindrical nozzles of diameter $4R = 2\,\mathrm{cm}$, which create a nitrogen sheath that stabilizes the mixing layer and prevents chemical reactions with ambient air. The velocity and temperature of the N_2 injected in the sheath is the same as in the main nozzles, with uniform profiles being assumed for all quantities.

To incorporate the electrodes in a parallel arrangement to the diffusion flame, the experiments feature two perforated metallic plates of diameter $8.0\,\mathrm{cm}$ that are positioned at the injection plane of the nozzles and have a high density of holes ($79/\mathrm{cm}^2$) and a small diameter per hole ($0.8\,\mathrm{mm}$). In the simulations, the electrodes are assumed to be perfectly permeable, in that the injected gas flows through them without significant pressure loss and in the absence of wake effects due to the small Reynolds numbers involved. Additionally, the two annular portions of the electrodes between the edge of the N_2-sheath injector and the outlet of the computational domain (i.e., $R < r \leq 8R$ at $x = \pm L/2$) are treated, for simplicity, as adiabatic non-slip walls.

The two electrodes are connected to a DC power source that provides a constant voltage difference across the burner in the axial direction. Whereas the electrode in the oxidizer nozzle is grounded, the one in the fuel nozzle is set to a negative electric potential whose magnitude ranges from 0 to $2.4\,\mathrm{kV}$ depending on the case considered. Correspondingly, Equation (2.26) for the electric potential Φ is integrated subject to Dirichlet boundary conditions at the electrodes along with zero-gradient conditions on all other boundaries. In analogy with the one-dimensional test case described in Section 3.3, the boundary conditions for the ionized species are imposed as follows. If the charge of the ionized species is such that they are electrostatically attracted to the electrode, a zero-gradient condition is imposed there on the corresponding mass fraction in order to avoid molecular diffusion of that component into the electrode. In this way, only the electrically-induced drift velocity is active on the electrode surface, which is associated with the ion current entering the electrode. Conversely, if electrostatic repulsion prevails on the electrode surface for a given component, its mass fraction is set to zero there to prevent any unrealistic flux of opposite-sign ions released by the electrode.

The transfer of momentum between charged and neutral particles is represented by the electric force ($\rho_q\mathbf{E}$) in the momentum conservation equation (2.22). This interaction, which, as shown in Section 3.5, primarily occurs outside the mixing layer in the inviscid region along distances of order L, is typically referred to as ionic wind. It represents a two-way coupled effect that can locally modify the flow field of the neutral gas and is quantified by the dimensionless parameter Ξ corresponding to the ratio of the characteristic electric force $\rho_{q0}E_{ref}$ to the characteristic convective acceleration $\rho_{ref}AU$ in Equation (2.22). In these simulations, Ξ is a small parameter at small voltage differences (i.e., $\Xi \sim 0.2$ at $|\Delta\Phi_{ref}| = 0.5\,\mathrm{kV}$), it increases with the applied voltage, and becomes an order unity parameter at the upper end of the range of voltages considered here (i.e., $\Xi \sim 3.7$ at $|\Delta\Phi_{ref}| = 2.0\,\mathrm{kV}$, and $\Xi \sim 5.4$ at

$|\Delta\Phi_{ref}| = 2.4\,\mathrm{kV}$), thereby highlighting the relevance of this mechanism in altering the flow field in the selected regimes.

3.5 Results

This section focuses on the results obtained from numerical integrations of the formulation described above. The results include analyses of the voltage/intensity response curve as well as characterizations of the influences of the electric field on the velocity field and on the distribution of charged species.

3.5.1 Electric characteristics of the diffusion flame

In non-reacting conditions, the voltage difference $\Delta\Phi_{ref}$ imposed on the electrodes induces a uniform constant electric field $E_{ref} = |\Delta\Phi_{ref}|/L$ across the burner in the $-x$ direction, thereby yielding a linearly varying electric potential $\Phi_{ref}(x) = \Delta\Phi_{ref}(2x/L - 1)$. However, combustion chemical reactions in the diffusion flame alter significantly the distribution of electric field, as shown in Figure 3.6. In particular, at low voltages compared to a saturation voltage introduced below, the diffusion flame resembles a Faraday cage that blocks the external electric field by the shielding action of abundant electric charges steered outwardly from the reaction region.

The flame-induced screening of the electric field is quantitatively shown by the flattened electric-potential distributions corresponding to $\Delta\Phi_{ref} = -0.5\,\mathrm{kV}$ and $-1.0\,\mathrm{kV}$ in Figure 3.6, and occurs independently of the levels of fuel dilution considered here. In this low-voltage regime, the charges are produced at a plentiful rate by the ionic chemical pathways described in Section 2.3 relative to their drift rate of removal from the reaction layers. As a result, the charges become spatially segregated along high concentration layers surrounding a central zone of much smaller charge where the chemical reactions responsible for producing charged species are important. As shown in below in Section 3.5.2, in this plateau, the mixture partially conserves the quasi-electroneutrality that characterized the unelectrified case. The two peaks of charge density lead to a dipole of opposite polarity to the external field, as shown in Figure 3.7, in a way that makes the diffusion flame to behave as a quasi-perfect conductor with nearly-zero electric field inside. These considerations resemble the mechanism of charge redistribution observed in electrified one-dimensional premixed flames [43]

The configuration with undiluted fuel yields stoichiometric conditions closer to the oxidizer injector and, therefore, creates a diffusion flame that acquires an equilibrium potential closer to that of the anode, as observed in Figure 3.6a. In contrast, Figure 3.6b indicates that intermediate values of the electric potential are attained at the diffusion-flame location when fuel dilution is employed since the latter displaces stoichiometry toward the fuel orifice. In both cases, a small peak of positive charge is observed in the reacting region in the $-0.5\,\mathrm{kV}$ case, which is caused by a small local excess of the concentration of hydronium, namely the major positive ion. The distributions of charged species are analyzed later in Section 3.5.2.

As the absolute value of the applied voltage is increased, the magnitude of the positive and negative peaks of the charge density increases and their separation distance decreases. This behavior, however, is non-monotonic with the voltage, as observed in Figure 3.7. Specifically, as $|\Delta\Phi_{ref}|$ is increased above $1\,\mathrm{kV}$, the electric field is increasingly less shielded by the charges, which tend to become spatially reorganized more uniformly across the burner, as evidenced by the broader and

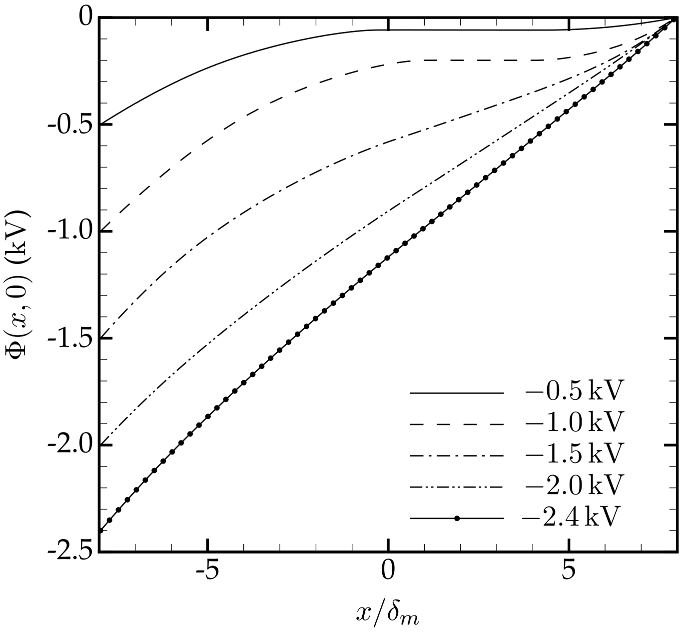

(a) $Z_{st} = 0.07$

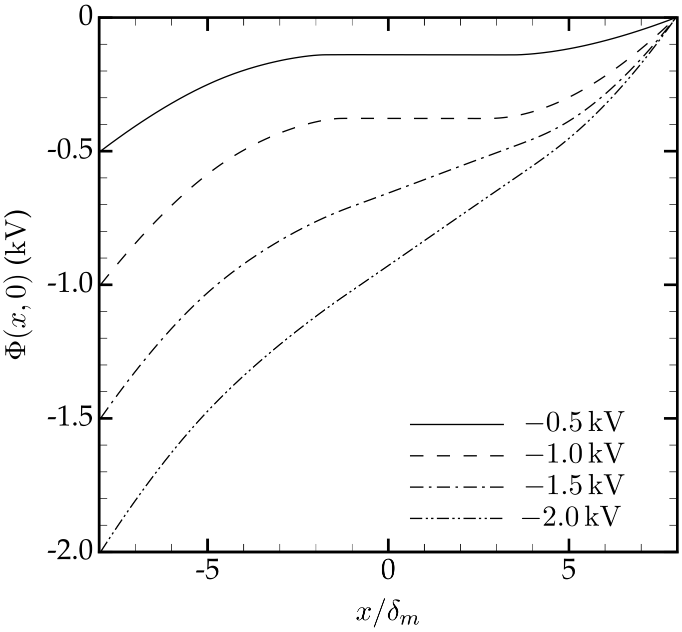

(b) $Z_{st} = 0.50$

FIGURE 3.6: Dimensional electric potential profiles along the axis of the burner for $Z_{st} = 0.07$ and $Z_{st} = 0.50$.

shallower distributions of the charge density shown in Figure 3.7. This results in an increasingly linear distribution of electric potential engendering an electric field that pierces into the diffusion flame and eventually reaches values close to the non-reacting uniform distribution E_{ref} at the largest voltage differences sampled here. Under these conditions, the characteristic production rates of heavy ions are slower than the rates of removal of these by the electric drift term in the diffusion velocity

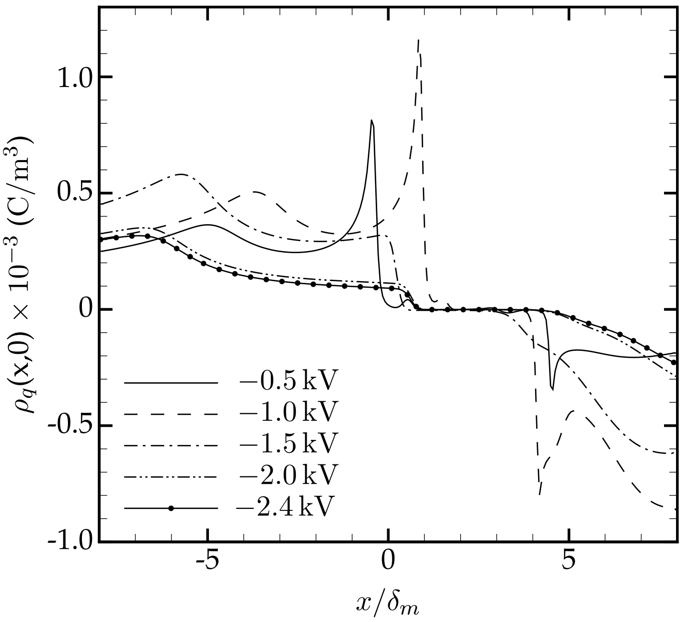

(a) $Z_{st} = 0.07$

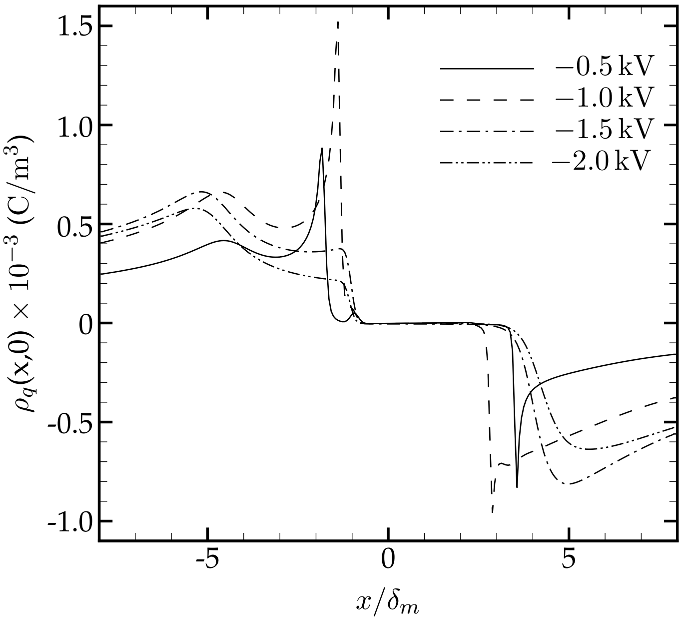

(b) $Z_{st} = 0.50$

FIGURE 3.7: Dimensional charge density profiles along the axis of the burner for $Z_{st} = 0.07$ and $Z_{st} = 0.50$.

(Equation (2.19)). As a result, a plateau of nearly-zero charge is also observed in the electric-charge distribution, although here the rapid electric drift suppresses the charge peaks observed above at smaller voltages.

The aforementioned changes in the distributions of the electric field and charge density as the applied voltage increases are closely related to the occurrence of a saturation in the rate of production of charges in the diffusion flame, which intrinsically limits the current density across the burner as follows. In the absence of combustion chemical reactions, the burner behaves as an open circuit when DC voltage is applied to the electrodes. In contrast, the presence of electric charges generated by chemical reactions in the diffusion flame produces a non-zero electric current across the burner, which is predominantly directed downwards along the axial coordinate x and depends on the voltage difference $\Delta\Phi_{ref}$. In particular, Figure 3.8 provides the voltage dependence of the intensity leaving the top (anode) electrode at $x = L/2$, namely

$$I = \int_0^{8R} 2\pi r \sum_{i=1}^{N_s} \rho_{q,i}(u_x + V_{i,x}) dr, \tag{3.3}$$

divided by the flame area πR_f^2, in a similar way as it is reported in the experiments by Park et al. [78], with $V_{i,x}$ and $\rho_{q,i}$ the radial distributions of the axial diffusion velocities and charge densities, respectively, as prescribed by Equations (2.19) and (2.17). Specifically, Park et al. [78] measured the current between the two electrodes and divided it by an estimated flame area πR_f^2, with R_f a radius determined by the flame luminosity. The corresponding experimental intensity values, which were reported only for the diluted case $Z_{st} = 0.5$, are reproduced here in Figure 3.8b. Conversely, in these simulations, R_f is determined by the radial extent of the distribution of the mass fraction of CH (i.e., $r \leq R_f$ where $Y_{\mathrm{CH}} \geq 10^{-9}$), since the chemical mechanism utilized here does not include any of the radiation-emitting species such as OH* or CH*. The resulting flame radius is of order $12\,\mathrm{mm}$ and $9\,\mathrm{mm}$ for the cases Z_{st} = 0.50 and Z_{st} = 0.07, respectively, and remains mostly independent of the applied voltage. Since the system is in steady state, the time variations of the total charge in the burner volume are zero. Consequently, charge conservation requires the flux of current density to be the same on each electrode, thereby leading to equal intensities there.

The voltage dependence of the intensity provided by Equation (3.3) has a qualitative structure that in principle does not depend on the dilution. In particular, the intensity increases monotonically for small voltages in a sub-saturated regime (zone A in Figure 3.8a), in which the incident electric field is screened by a shield of charges there are produced abundantly and surround the diffusion flame, as described above and shown in Figures 3.6 and 3.7. The intensity reaches a saturation value near the upper limit of the voltage interval studied here (i.e., at $|\Delta\Phi_{ref}| \sim 2.0\,\mathrm{kV}$; zone C in Figure 3.8a), where the incident electric field supersedes recombination in removing ions, thereby limiting the current by the rate of ionization. A third or overcurrent regime at intermediate voltages (zone B in Figure 3.8a), where a peak in intensity occurs, is observed in the experiments for the configuration with $Z_{st} = 0.5$ and numerically in the $Z_{st} = 0.07$ case. In the simulations of the $Z_{st} = 0.50$ case, this overcurrent appears to be absent perhaps due to undersampling in voltage space.

The overcurrent regime is not typically observed in one-dimensional premixed flames [43, 59, 63, 100, 101]. There, the baseline profiles of the radicals starting the ionic chemistry chain remain mostly unaffected by the electric field. As a result, the current increases with the applied voltage up to a saturation voltage where the finite rate of production of charged species becomes the limiting process. In these conditions, a saturation plateau in the electric current occurs where, despite the large electric fields, the electric drift diffusion flux remains limited by how many charges are produced per unit time. In contradistinction, as described later in Section 3.5.4, in the present problem the profiles of the radicals starting the ionic chemistry, along with the rates of production of ionized species, are all closely coupled to the strain-rate field. Since the latter is sensitive to the incident electric field, the dependence of the ion-current intensity on the applied voltage does not have to be necessarily monotonic. In this particular case, the presence of the overcurrent is the result of a drop in the limiting current as saturation conditions are approached (i.e., $-2.0\,\mathrm{kV}$) due to the decrease in the local scalar dissipation rate there, which leads to overall faster chemistry and correspondingly smaller concentrations of charged species.

The comparison between experimental and numerical values of the intensity for the $Z_{st} = 0.5$ case in Figure 3.8b reveals some important limitations of the formulation described above. Although the sub-saturated and saturated regimes are present in both experiments and simulations, the simulations tend to overpredict the intensity approximately by a factor of 2.5 with respect to the experimental values, including the saturation range, where the current only depends on the charge-production modeling capability of reaction (R1.1) (see related discussions, albeit for premixed flames, in Ref. [43]). A similar offset with respect to the experimental measurements carried out by Speelman et al. [100] is observed in the supplementary simulations of the premixed burner-stabilized premixed flame provided in the Section 3.3. The magnitude of these mismatches in saturation currents are standard in the general literature of premixed flames and jet flames under electric fields [100, 101, 123] and suggest that the chemical mechanism discussed in Section 2.3 also underperforms in counterflow diffusion flames. The root cause of this shortcoming resides in the coupling between neutral and ionic chemistries, including inaccuracies in the prediction of CH and O radicals generated from neutral production pathways, and in the large uncertainties associated with the rates of the chemical steps participating in the ionized radical chains. Potential improvements to this framework could include the utilization of extended chemical mechanisms [69, 91, 110] or case-specific optimizations of ionization rates in the submechanism for the charged species [100], although these are aspects that are subject of future research.

3.5.2 Effects of the incident electric field on the flame structure

The general structure of non-electrified, methane counterflow diffusion flames has been extensively studied in the past [85, 95] and remains qualitatively unaltered in the range of voltages studied here. The most relevant effect of the incident electric field, however, is to alter significantly the distribution of minor charged intermediates, whose momentum exchange with the neutral molecules through the electric force ultimately leads to non-negligible disturbances of the hydrodynamic field around the diffusion flame, as described below.

The temperature along the axis of the burner in the presence of electric fields is shown in Figure 3.9. It is worth mentioning that the maximum temperature undergoes only small increments in all cases, although the location of the peak fluctuates around the unelectrified one in a manner that does not appear to have a straightforward explanation, particularly in the undiluted case $Z_{st} = 0.07$ depicted in Figure 3.9a. For instance, the curves corresponding to the subsaturated regime (i.e., 0.0 and $-0.5\,\mathrm{kV}$) indicate a shift of the temperature profile toward the fuel side as the voltage increases, while the shifting pattern thereon becomes less clear, especially across the overcurrent zone B of the intensity-voltage curve (Figure 3.8a). Multiple phenomena contribute to the displacement and the shape modification of the flame temperature profiles. For instance, the positive and negative ions exert forces on the mixture, which are oriented in opposite directions. The balance between the two forces may not be null because of the different mobility of the charged species involved in the problem and of the different distance between the flame front and the two electrodes [25]. Such an imbalance leads to a displacement of the equilibrium positions of the stagnation plane and of the flame inside the burner. Moreover, as shown below in Section 3.5.4, the flow near the axis becomes increasingly two-dimensional as the voltage increases because of the fluid mechanical disturbances

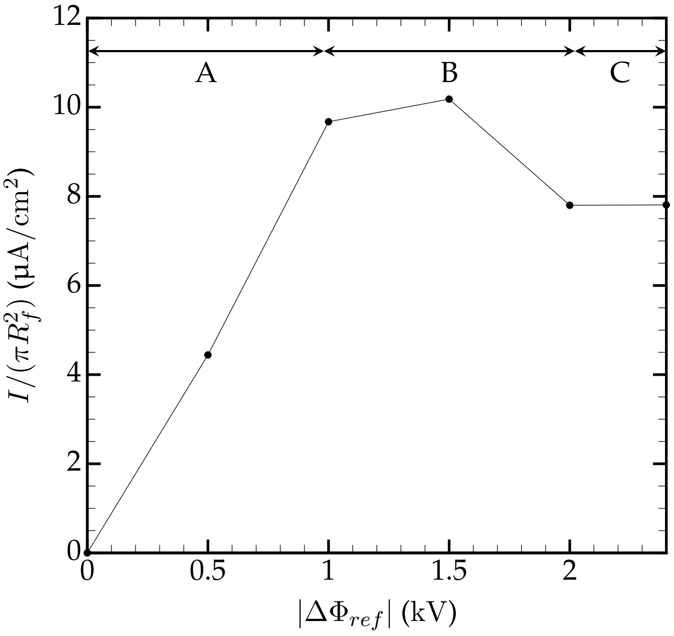

(a) $Z_{st} = 0.07$

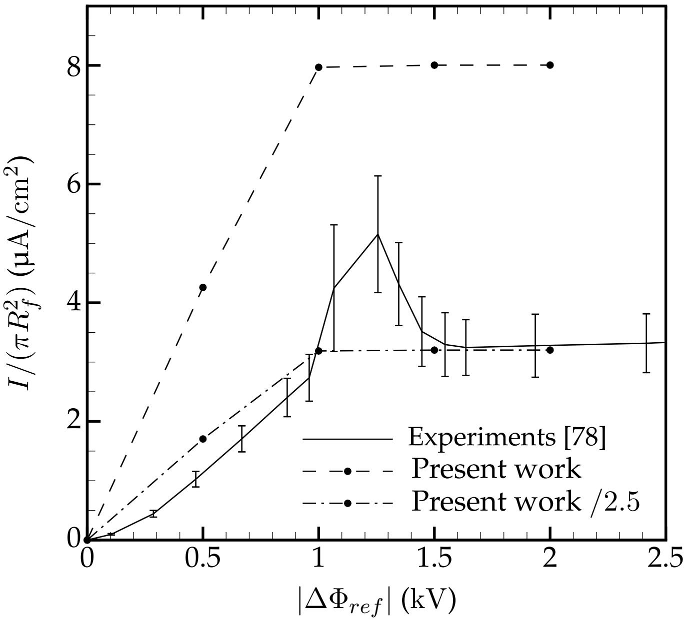

(b) $Z_{st} = 0.50$

FIGURE 3.8: Intensity per unit flame area measured at the top electrode as a function of the voltage difference $|\Delta\Phi_{ref}|$ for $Z_{st} = 0.07$ and $Z_{st} = 0.50$. In panel (b), the experimental data and the associated uncertainty bars are based on Ref. [78].

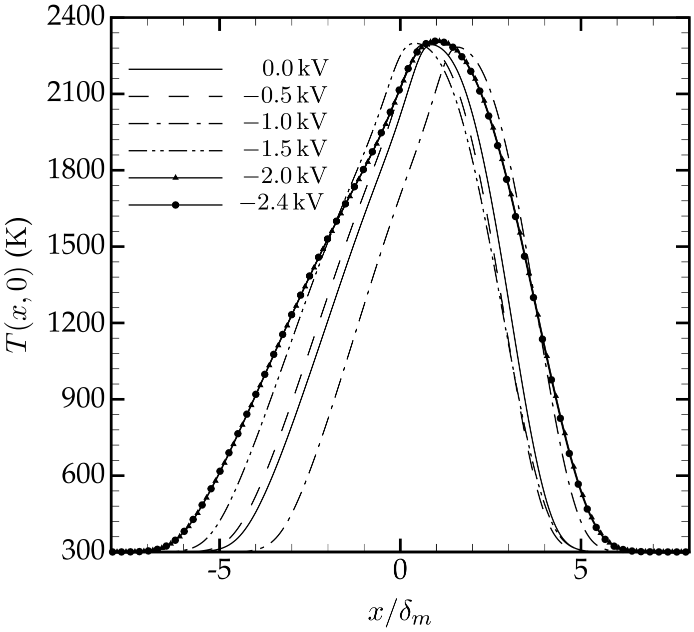

(a) $Z_{st} = 0.07$

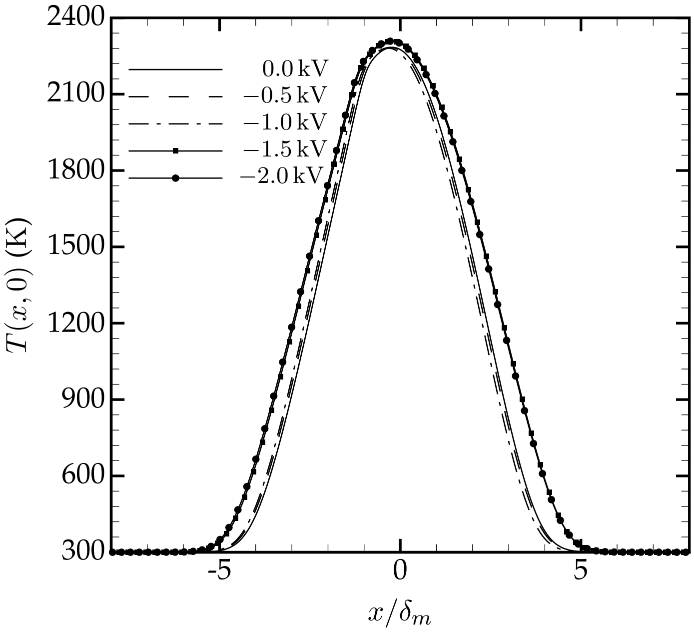

(b) $Z_{st} = 0.50$

FIGURE 3.9: Temperature profiles along the axis of the burner for $Z_{st} = 0.07$ and $Z_{st} = 0.50$.

introduced by the electric force, which complicates the interpretation of the complex patterns of one-dimensional variations observed along the burner axis. More importantly, the temperature profile widens as the voltage is increased as a result of the decreased flow strain rate and of the increased current across the burner, which induces an Ohmic dissipation (i.e., the last term on the RHS of Equation (2.24)) that heats up the gas flow on both sides of the mixing layer. The phenomena contributing to the displacement and the shape modification of the axial profiles, including the cause of the decrease in the strain rate, involves the interaction of ionic winds with the incoming flow of the neutral mixture and is discussed further below.

In the diluted case $Z_{st} = 0.5$ provided in Figure 3.9b, the location of the temperature peak remains mostly the same independently of the applied electric field, and the temperature increment on the flanks of the mixing layer is less intense. In contrast to the non-trivial pattern of variations observed in the undiluted case in Figure 3.9a, the curves in the diluted case can be easily grouped into subsaturated (i.e. 0.0, -0.5, and $-1.0\,\mathrm{kV}$) and saturated (i.e. $-1.5\,\mathrm{kV}$ and $-2.0\,\mathrm{kV}$) subsets indicating a negligible shift of the temperature peak as the voltage increases. The decreased shift of profiles and the collapse of the curves into those two subsets are observed as well for other bulk quantities such as major neutral concentration profiles, flow velocities and scalar dissipation rates, as shown later in Section 3.5.4.

The general structure of the concentration profiles of major reactants and products undergoes only small variations under electric fields. This is shown in Figure 3.10, which provides the molar-fraction profiles of the major neutral species CH_4, O_2 and H_2O along the burner axis. The CH_4 is attacked by H radicals in the diffusion flame in a chain-breaking reaction to form CO, which oxidizes to CO_2 in a broader oxidation layer that lies on the O_2-side of the diffusion flame (profiles not shown here for brevity). The overall effect of the electric field is to spatially shift these profiles in a manner analogous to that observed for the temperature in Figure 3.9. Concurrent with the latter, a broadening of the mixing layer is observed in Figure 3.10 due to the corresponding increase in kinematic viscosity.

A minor but relevant intermediate included in Figure 3.10 is CH, which, together with O, participate in the chemi-ionization reaction (R1.1) that starts the ionic-chemistry pathways. In all cases, the CH layer is thin (it is computationally solved by ~ 8 grid points), and is located on the fuel-rich side of the diffusion flame. As the applied voltage increases, the peak molar fraction of CH, which is of order 10^{-4}, decreases and shifts in accordance with the temperature and the profiles of the other major neutral species displayed in the figure. Under fuel dilution, the modifications introduced by the electric field in the major neutral species profiles in Figure 3.10b are consistent with the experimental observations in Park et al. [78]. Specifically, the distributions in the two top panels, which correspond to sub-saturated conditions, are almost coincident. The same is observed in the two bottom panels where the diffusion flame reaches electrical saturation. In these two saturated cases, the diffusion flame is slightly shifted towards the fuel side and the CH molar fraction decreases in a similar manner as in the undiluted case in Figure 3.10a. Once saturation conditions are attained, it is shown below in Section 3.5.4 that the local strain rate in the vicinity of the flame location decreases as a result of the flow displacement created by the ionic wind, and, as a consequence, the local diffusion time increases, thereby elevating the peak temperature albeit in small amounts, as observed in Figure 3.9. The subsequent attainment of increasingly faster overall chemistry generally decreases the content of all intermediates, including CH and the ionized species, as shown below.

The distribution of molar fractions of the six charged species participating in the ionic chemical description provided in Section 2.3, namely H_3O^+, CHO^+, $O_2{}^-$, O^-, OH^-, and e^-, are shown in Figure 3.11 along the burner axis. It is worth mentioning that, under zero incident electric fields, as in the top left panels of Figure 3.11a and b, there exists a self-induced, quasi-electroneutral distribution of charged species in the diffusion flame that nonetheless leads to vanishingly small potentials of order

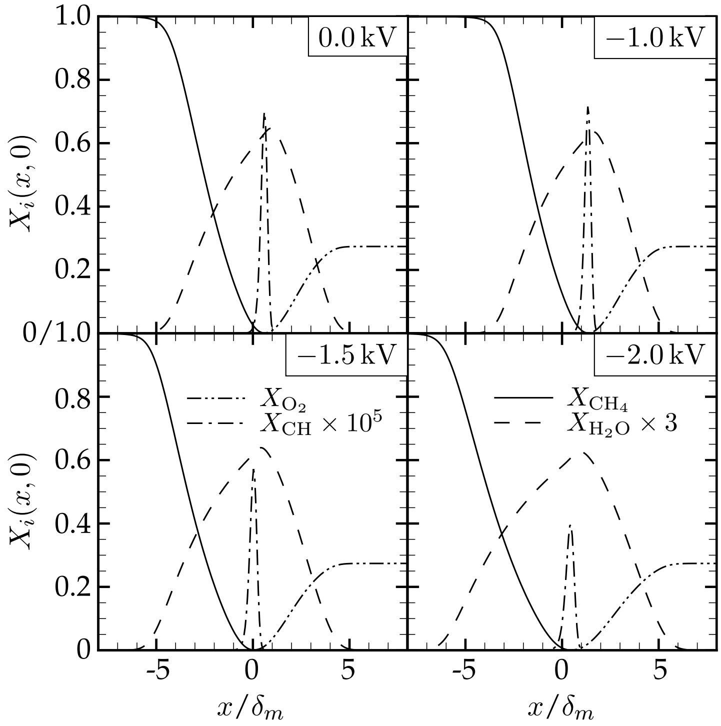

(a) $Z_{st} = 0.07$

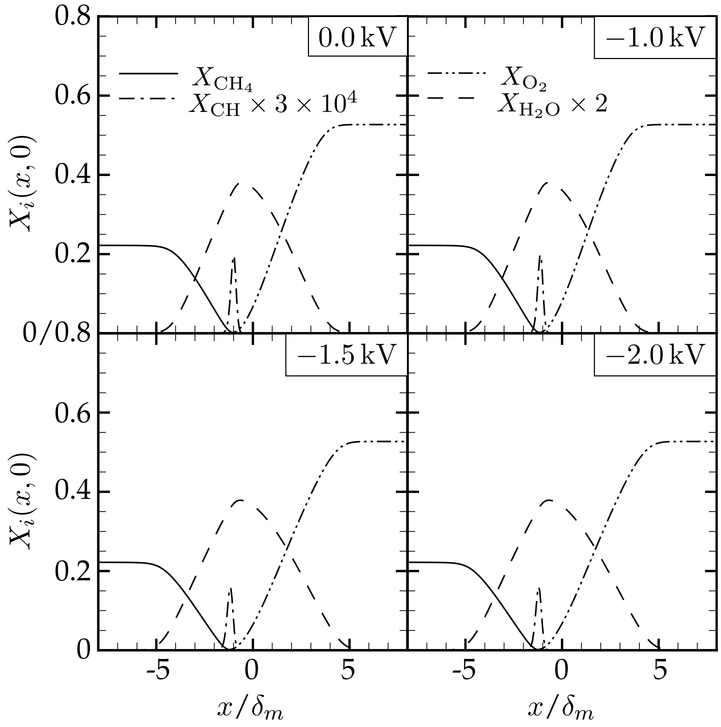

(b) $Z_{st} = 0.50$

FIGURE 3.10: Molar fraction profiles of the neutral species along the axis of the burner for $Z_{st} = 0.07$ and $Z_{st} = 0.50$.

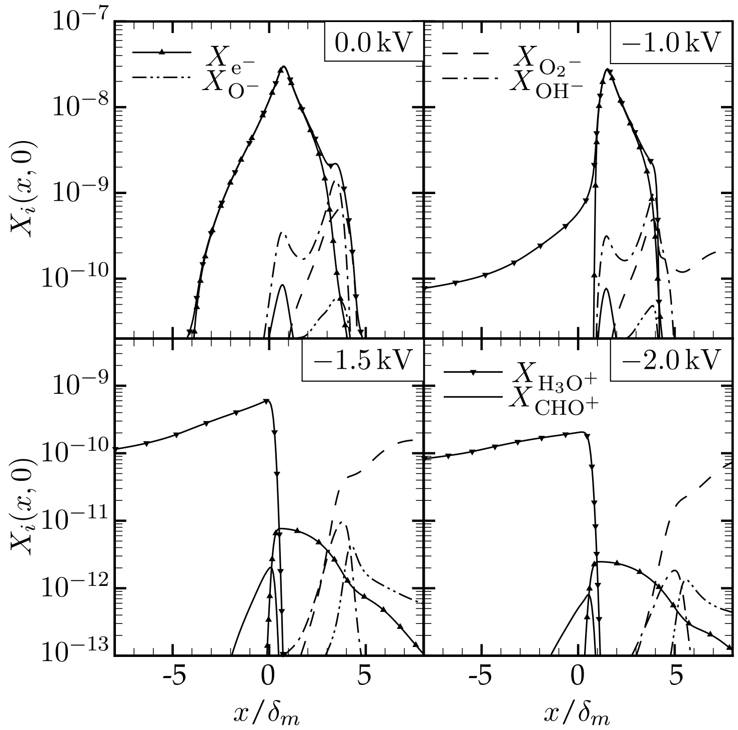

(a) $Z_{st} = 0.07$

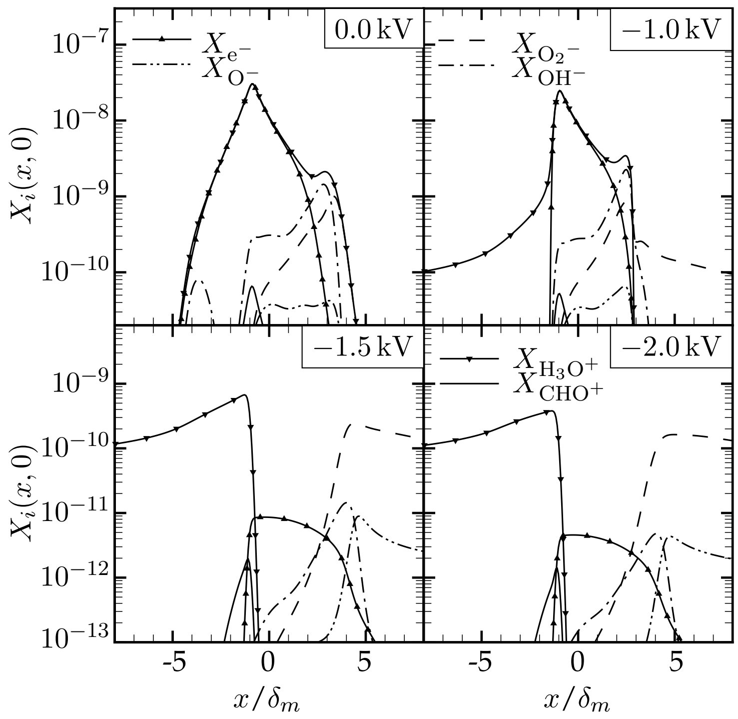

(b) $Z_{st} = 0.50$

FIGURE 3.11: Molar fraction profiles of charged species along the axis of the burner for $Z_{st} = 0.07$ and $Z_{st} = 0.50$.

10 V, which are caused by small mismatches between hydronium and electron concentrations. The general structure of the charged species in the unelectrified cases, however, reveals some important physical phenomena that are to be disturbed when the external voltage is applied. In particular, for $\Delta\Phi_{ref} = 0$, it is observed that the H_3O^+ produced by the charge-transfer reaction (R1.2) represents the major ion in the diffusion flame, whose peak concentration location coincides with that of CH in Figure 3.10. In contrast, the CHO^+ produced by the chemi-ionization step (R1.1) is present only in relative fractional amounts as a result of its rapid conversion into H_3O^+ through the step (R1.2). The molar fraction of hydronium is mostly everywhere matched by that of the electrons, and, consequently, the positive charge of H_3O^+ is correspondingly neutralized, with small positive differences of order $X_{\mathrm{H_3O^+}} - X_{\mathrm{e^-}} = O(10^{-12})$ being responsible for the small self-induced voltages as a result of the larger diffusivity of the electrons. However, near the oxidizer side, the concentration of electrons decreases rapidly and is unaccompanied by a decrease in H_3O^+, as it would be expected if the process involved the dissociative recombination reaction (R2.1). Instead, the electrons are invested in the attachment steps (R2.5)-(R2.7), which produce the major participating anions ${O_2}^-$, OH^-, and O^-. Eventually, these heavy anions are responsible for the portion of the bi-directional ionic wind that flows in the opposite direction to the incident electric field.

Upon applying an external electric field in the $-x$ direction, Figure 3.11 indicates that the H_3O^+, along with the CHO^+ to a much lesser extent, are steered toward the cathode while the cloud of negative charges is steered toward the anode. It is worth highlighting that the chosen polarity of the electric field efficiently leads to this distortion as opposed to a field applied in the $+x$ direction, in that the negative charges are prominently produced on the oxidizer side of the flame and therefore can be easily steered toward the anode placed on that side. Among the negative charges, the ${O_2}^-$ overwhelmingly dominates the charged concentration profiles on the oxidizer side in both undiluted and diluted cases because of the locally high temperatures and the prevalence of O_2 there, which mediates in the production of ${O_2}^-$ through the electron-attachment reaction (R2.5).

Until the voltage for the onset of the overcurrent zone is applied, the central distribution of charged species in the diffusion flame is marginally influenced by the incident electric field, as shown in the right upper panels of Figure 3.11a and b. In this way, the net electric charge density remains everywhere small in this region. However, a noticeable electric drift of ions occurs that creates long tails in the distributions of molar fractions of H_3O^+ and ${O_2}^-$ lasting until the surface of the electrodes. As a result, positive and negative charge imbalances occur, respectively, on the fuel and oxidizer sides of the mixing layer, which, in conjunction with the decreasingly small values of ionic mobilities attained as low temperatures are approached in the periphery of the flame, lead to the charge density spikes shown in Figure 3.7 and to the subsequent screening of the incident electric field. Additionally, as explained later in Section 3.5.3, this excess of ions outside the mixing layer, which is accompanied by an outward motion as prescribed by the incident electric field, is responsible for the bi-directional ionic wind, the alteration of surrounding hydrodynamic field along distances of order L, and the modification of the flame axial position in the burner.

In saturated conditions corresponding to the bottom panels in Figure 3.11a and b, the amount of produced charges is not sufficiently large to shield the reacting region from the incident electric field. In these conditions, the electric field is able to steer a large amount of charged species away from the reaction zone before they are replenished by their corresponding production steps. This leads to the occurrence of an upper limit in the electric intensity across the burner, as shown in Figure 3.8. As a result, a large decrease (i.e., by one to two orders of magnitude) in the molar fraction of charged species in the diffusion flame is observed with increasing voltages. On the other hand, the concentration of charges near the electrodes is relatively more robust to variations in the voltage.

The depletion of electrons in the diffusion flame predicted as the voltage is increased beyond sub-saturation conditions is comparatively more evident than for other ions because of the large values of the mobility k_{e^-}. In particular, the electrons undergo a fast depletion once transported to the oxidizer edge of the mixing layer, where they are rapidly transformed in other anionic species through electron-attachment reactions. In addition, as the voltage increases, the increasing drift of electrons towards the anode inhibits the spatial overlap between the $X_{\mathrm{H_3O^+}}$ and X_{e^-} distributions, which largely suppresses the dissociative recombination step (R2.1). Consequently, this favors the onset of saturation, in which the removal of charged species relies on the electric drift towards the electrode.

3.5.3 Distribution of electrically-induced ionic winds

The incident electric field induces a displacement of charges axially outwards from the flame, as quantitatively shown in Figures 3.7 and 3.11. In particular, the major ions that prevail on the fuel and oxidizer sides are, respectively, H_3O^+ and $O_2{}^-$. Despite the small sub-ppm concentration of these ions near the electrodes, an electric force that scales with the characteristic convective acceleration $\rho_{ref}\ A\ U$ of the flow outside the mixing layer is generated across the burner on both oxidizer and fuel streams, as shown in Figure 3.12 for both undiluted and diluted cases. This force, which gives rise to the bi-directional ionic wind, acts primarily in the axial direction and tends to displace the gas axially outwards away from the diffusion flame. The flow displacement effect is favored by the lower temperatures and the subsequent decrease in the mixture density outside the mixing layer. These considerations are in qualitative agreement with the experiments in Park et al. [78].

As indicated in its definition (Equation (1.1)), the electric specific force is given by the multiplication of the charge density ρ_q by the electric field $\mathbf{E}$. In particular, the variations of electric force with the applied voltage in Figure 3.12 are qualitatively similar to those of the electric charge in Figure 3.7. In the undiluted case, the electric force increases with the applied voltage for the most part of the spatial domain up to the overcurrent voltage $-1.5\,\mathrm{kV}$. Saturated conditions are attained for $-2.0\,\mathrm{kV}$ that flatten and broaden the charge distribution and the electric-force profile. Under fuel dilution, the electric force increases monotonically almost everywhere with the applied voltage, as shown in Figure 3.12b. In all cases, and in the scales of the vertical axis utilized to draw Figure 3.12, a plateau of vanishingly small values is observed in the electric force density that coincides spatially with a similar plateau of vanishing electric charge density observed in Figure 3.7, and which corresponds to the layer where the chemical reactions in the diffusion flame develop.

In connection with the effect of the incident electric field on the bulk flow, a qualitative aspect worthy of discussion is the asymmetry of the electric-force profiles with respect to the flame. For instance, the undiluted case in Figure 3.12a is characterized by a clear asymmetry in the profiles that is induced by the tendency of chemical reactions to develop closer to the oxidizer side because there is where overall stoichiometric conditions occur. In contrast, the fuel-diluted case in Figure 3.12b has a comparatively more symmetric distribution of electric force. Asymmetric profiles of

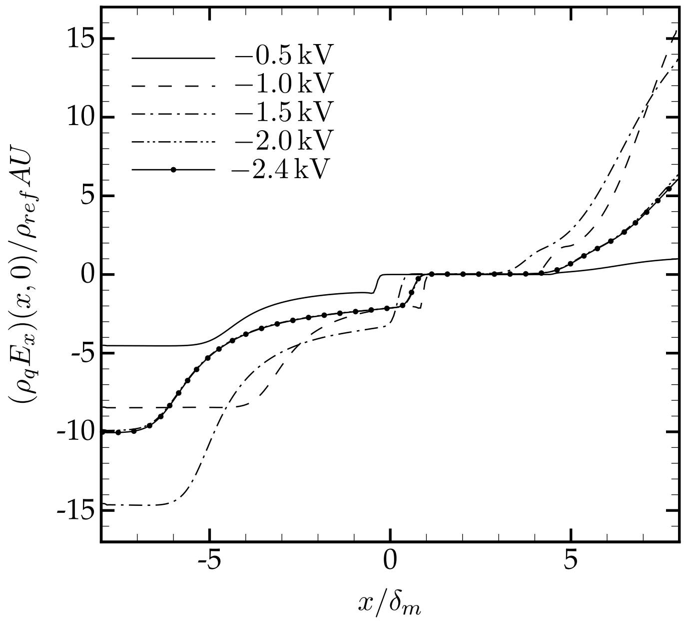

(a) $Z_{st} = 0.07$

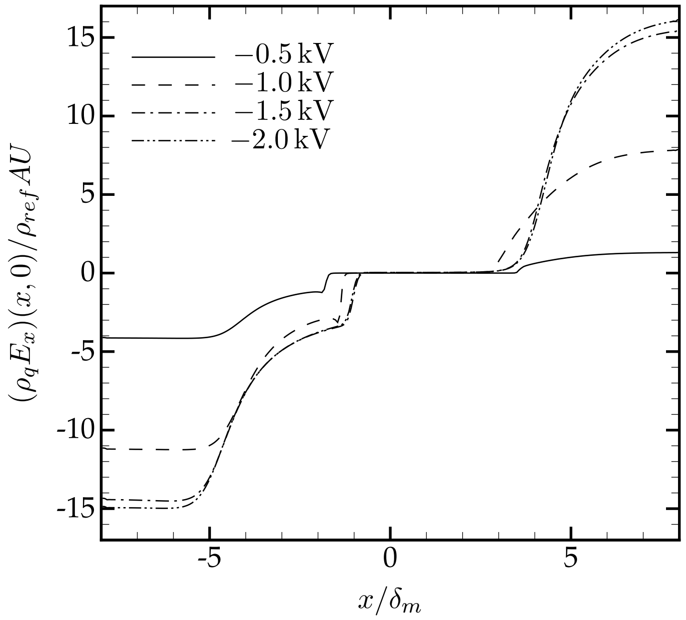

(b) $Z_{st} = 0.50$

FIGURE 3.12: Axial component of the non-dimensional electric force profiles along the axis of the burner for $Z_{st} = 0.07$ and $Z_{st} = 0.50$. In panel (a), the lines corresponding to -2.0 and -2.4 kV are almost coincident.

ionic winds as in Figure 3.12a lead to more significant distortions of the position of the stagnation plane, which is pushed downwards to the fuel side.

3.5.4 Effects of the incident electric field on hydrodynamics and mixing

The numerical results presented above provide evidence of a bi-directional ionic wind that is directed outwards from the diffusion flame and which emerges from the distortion induced by the incident electric field on the distribution of charged species. The transfer of momentum and energy from the ionic wind to the bulk gas is significant and generates modifications of the velocity and mixing fields, as shown below.

The local scalar dissipation rate in the vicinity of the flame, whose inverse represents a relevant time scale of diffusion of reactants across the mixing layer, and which is inversely proportional to the local strain rate, is observed to remain mostly unaltered in the range of sub-saturated voltages, but decreases across the overcurrent and saturation regimes, thereby strengthening the flame. The first evidence of this electrically induced phenomenon in both diluted and undiluted cases is shown by the axial distributions of axial velocities provided in Figure 3.13. Consider first the undiluted case in Figure 3.13a. The velocity profile in the unelectrified case differs from the quasi-linear one expected in constant-density non-reacting flows, in that it displays a rapid acceleration of the axial flows of fuel and oxidizer towards the flame due to thermal expansion. As shown in Figure 3.13a, the maximum temperature is located on left side of the vertical velocity maximum. Incrementing the voltage across the sub-saturated conditions $|\Delta\Phi_{ref}| = 0.5$ and $1.0\,\mathrm{kV}$ has the effect of displacing the diffusion flame jointly with the stagnation plane first toward the fuel side and then toward the oxidizer side without extensive deformation of the axial velocity profile along the burner axis and in a manner that correlates well with the shifts in the temperature profiles in Figure 3.9.

Two-dimensional visualizations of these variations are provided in Figure 3.14, which shows flow streamlines along with contours of CH mass fractions. In interpreting these two cases, it is worth noting that the shift toward the oxidizer side in the $-1.0\,\mathrm{kV}$ case is actually the result of a significant convex curvature of the stagnation plane, which curves downwards as the ionic wind pushes it toward the fuel side as observed in the second panel in Figure 3.14. At the overcurrent voltage, $|\Delta\Phi_{ref}| = 1.5\,\mathrm{kV}$, the stagnation plane moves farther to the fuel side jointly with the flame, but the axially outwards flow displacement made by the increasingly stronger ionic wind decreases the radial velocity and makes the axial velocity profile shallower, thereby decreasing the effective strain rate in the flame vicinity.

Correspondingly, the stoichiometric value χ_{st} of the scalar dissipation rate

$$\chi(Z) = 2\alpha_Z |\nabla Z|^2, \tag{3.4}$$

evaluated at $Z = Z_{st}$ decreases by approximately 50% as the voltage is increased to the saturation value, as shown in Figure 3.16.

In Equation (3.4), the diffusivity α_Z is taken equal to the local thermal diffusivity of the mixture. Additionally, as proposed by Pitsch and Peters [88] and standardly done in flamelet modeling, Z is a mixture fraction obtained by computing the solution to the sourceless advection-diffusion equation

$$\nabla \cdot (\rho \mathbf{u} Z) = \nabla \cdot (\rho \alpha_Z \nabla Z) \tag{3.5}$$

subject to $Z = 0$ and $Z = 1$ on the oxidizer and fuel streams, respectively, with zero-gradient conditions being applied everywhere else along the boundaries of the computational domain. A reference scalar dissipation rate can be obtained by integrating (3.5) assuming negligible variations of Z in the radial direction, constant

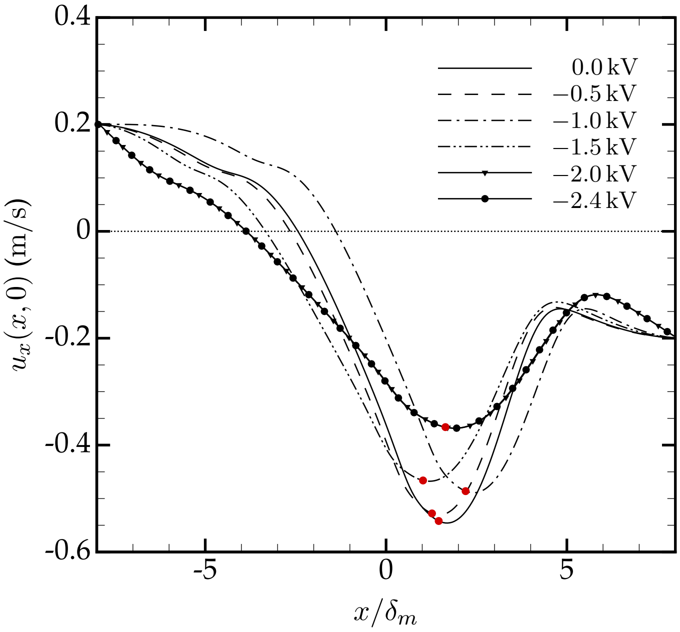

(a) $Z_{st} = 0.07$

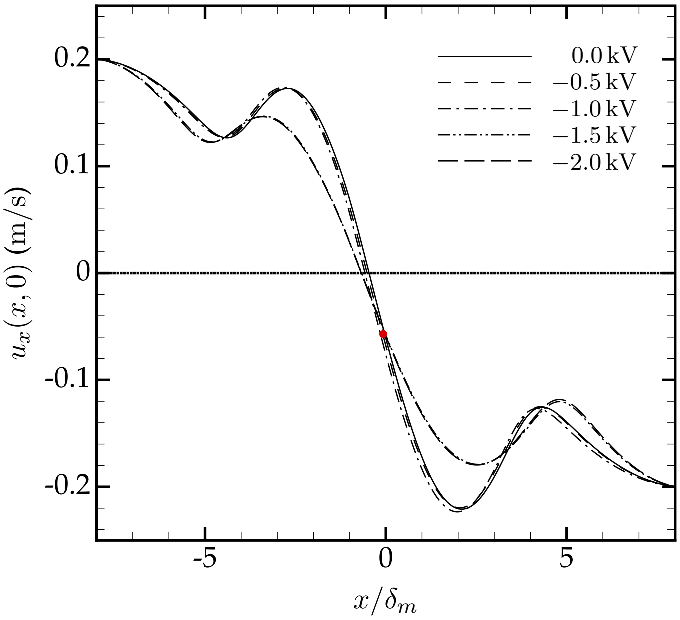

(b) $Z_{st} = 0.5$

FIGURE 3.13: Axial velocity profiles along the axis of the burner for $Z_{st} = 0.07$ and $Z_{st} = 0.5$. The red points represent the flame locations determined using the peak of the CH molar-fraction.

values for ρ and α_Z, infinitely far boundaries located at $x = \pm\infty$, along with a linear velocity distribution $u_x = -Ax$. The resulting expression is [62, 85]

$$\chi(Z) = \frac{A}{\pi} \exp\left\{ - \left[\sqrt{2} \mathrm{erfc}^{-1}(2Z) \right]^2 \right\}, \tag{3.6}$$

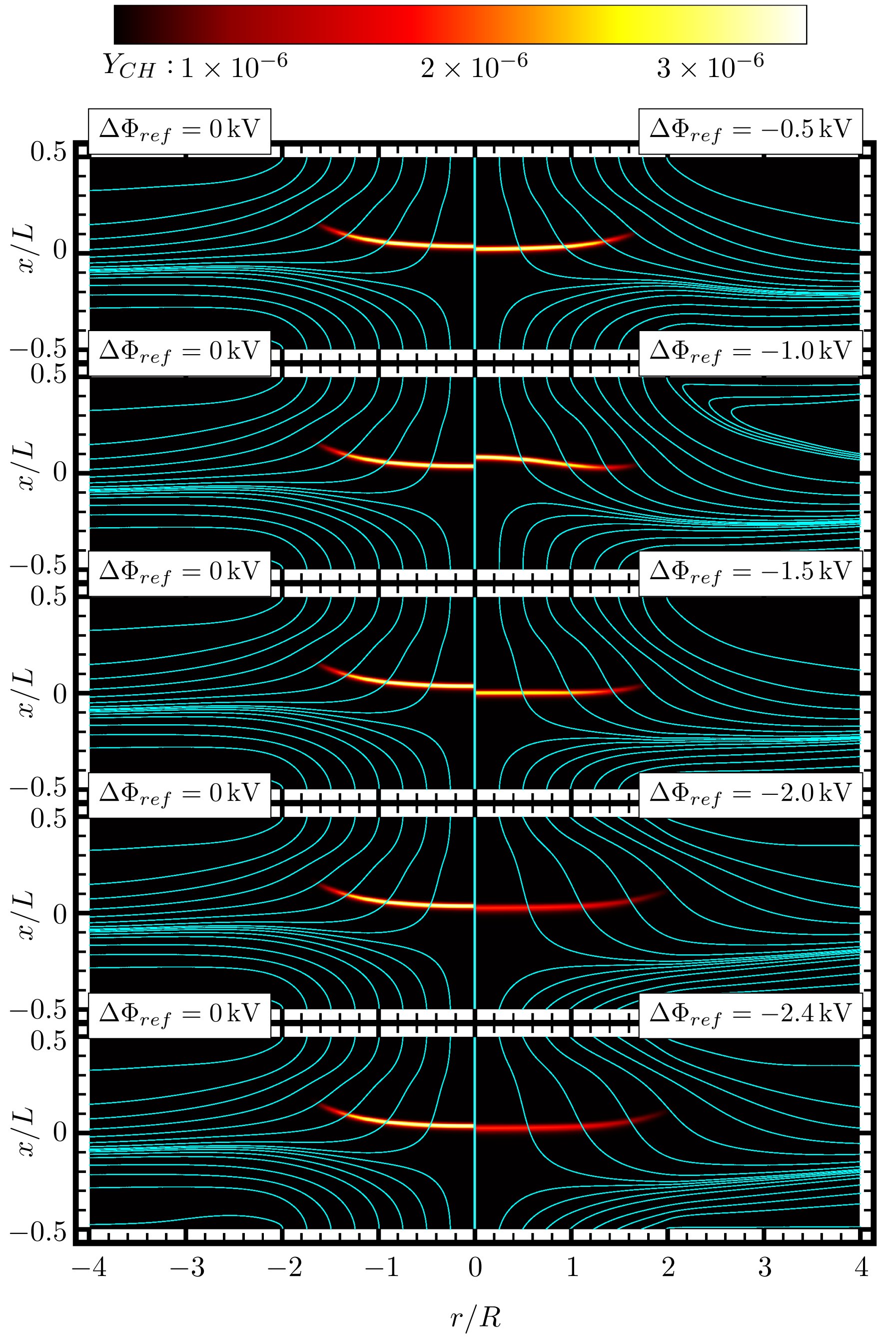

FIGURE 3.14: Flow streamlines overlaid on CH mass-fraction contours for $Z_{st} = 0.07$. The unelectrified case $\Delta\Phi_{ref} = 0\,\mathrm{kV}$ is provided on the left panels to facilitate direct comparison with the corresponding electrified case.

which corresponds to a symmetric bell-shaped curve centered at $Z = 0.5$.

The reference scalar dissipation rate in Equation (3.6) is compared in Figure 3.17 to the scalar dissipation arising from the numerical solution of Equation (3.5) for the present problem. Note that the scalar dissipation rate of the unelectrified case does not match the reference value (3.6) due to the temperature dependence of α_Z and to

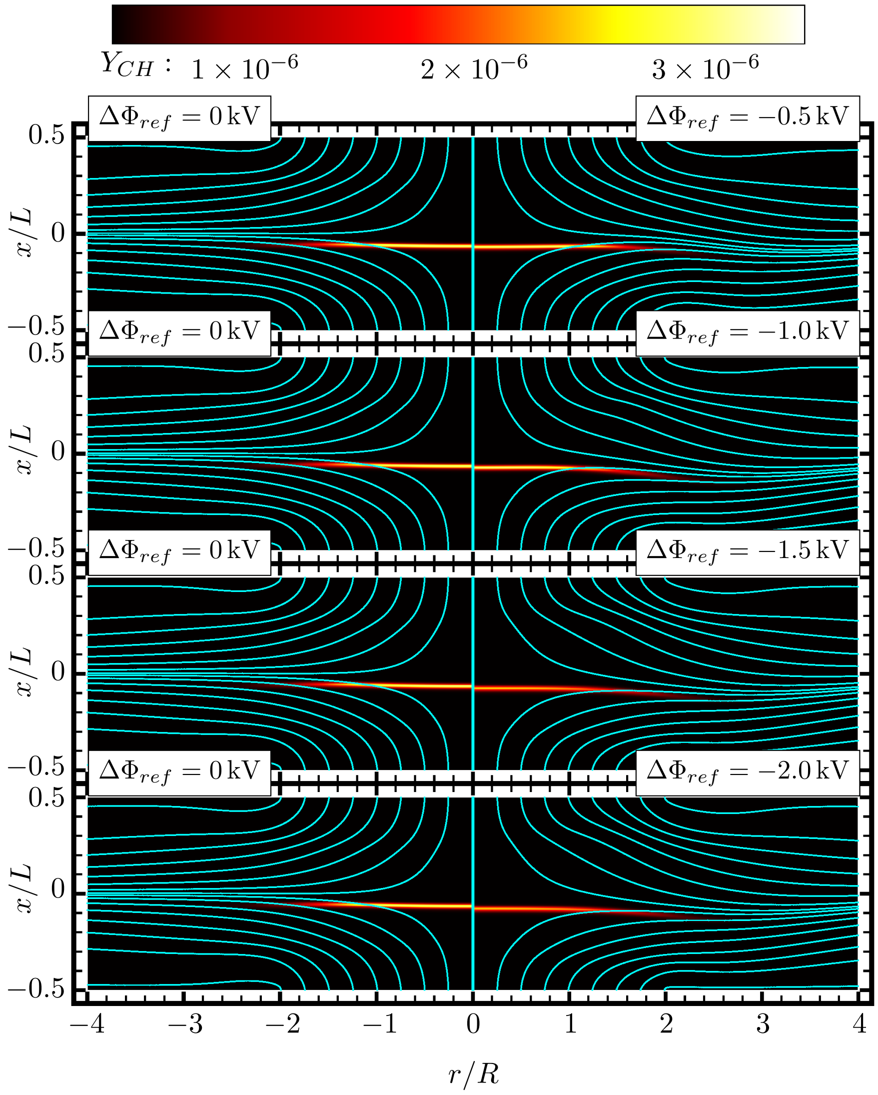

FIGURE 3.15: Flow streamlines overlaid on CH mass-fraction contours for $Z_{st} = 0.50$. The unelectrified case $\Delta\Phi_{ref} = 0\,\mathrm{kV}$ is provided on the left panels to facilitate direct comparison with the corresponding electrified case.

thermal expansion effects. More importantly, in the undiluted case in Figure 3.17a, as the voltage is increased, the scalar dissipation rate becomes increasingly skewed to the fuel side due to the augmentation of composition gradients there as a result of the downward displacement of the stagnation plane.

As saturation conditions are approached, $|\Delta\Phi_{ref}| \geq 2.0\,\mathrm{kV}$, the strength of the ionic wind becomes limited by the rate of production of charged species. In this limit, an equilibrium configuration is attained in a strain-rate field that shows little to no sensitivity to the applied voltage, as shown by the lower plateau attained by the stoichiometric scalar dissipation rate in Figure 3.16.

The hydrodynamic interactions described above are much more limited in the fuel-diluted case $Z_{st} = 0.50$, which generally leads to a diffusion flame positioned closer to the stagnation plane as required by the modified spatial location of the

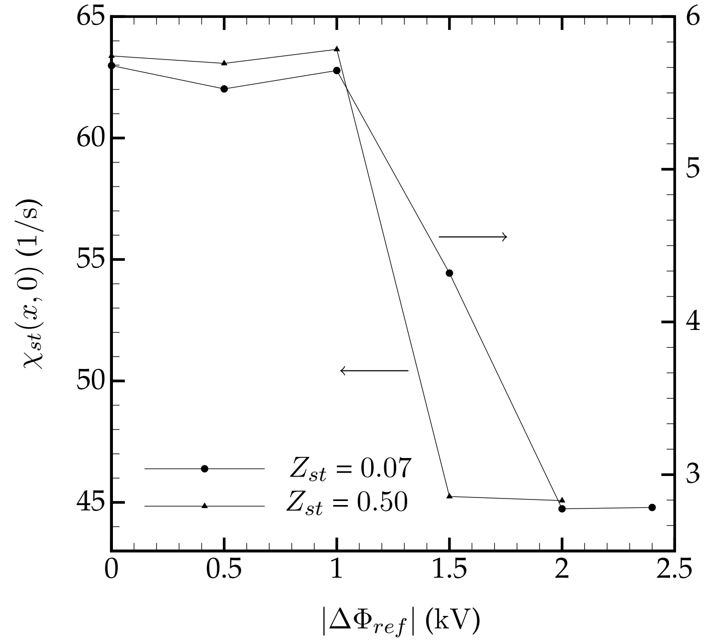

FIGURE 3.16: Stoichiometric scalar dissipation rate plotted versus the applied voltage.

stoichiometric conditions. The resulting axial velocity profile remains mostly symmetric about the mid section of the burner, as shown in Figure 3.13b. In addition, the increased symmetry of the electric force, in this case, leads to negligibly small shifts of the position of the stagnation plane, as observed in the two-dimensional visualizations in Figure 3.15. Although the overall effect of the incident electric field at saturation is to decrease χ_{st} by approximately 30%, the distribution of the scalar dissipation rate in mixture-fraction space remains close to that of the unelectrified case, as shown in Figures 3.16 and 3.17b.

3.5.5 Comparisons between numerical and experimental flow fields

The experimental flow visualizations by Park et al. [78] suggest strong modifications of the velocity field at similar voltages to the ones addressed in this study. In contrast, the numerical results presented here indicate that the modifications are rather moderate. This section provides a brief discussion about possible sources of these discrepancies.

A comparison between experimental and numerical profiles of the axial velocity are provided in Figure 3.18 for the undiluted case $Z_{st} = 0.07$. Although the general trends of both experimental and numerical profiles are the same as the voltage is increased, including the axial shift of the stagnation plane toward the fuel side, the comparisons reveal significant quantitative discrepancies. The first noteworthy aspect relates to the first measured point near the fuel orifice, where the measured velocity is approximately $10\,\mathrm{cm/s}$ larger than the numerical one, despite the fact that the fuel mass flow rate was experimentally controlled in Ref. [78] to yield the same value of injection velocity as the one utilized in the present study. This mismatch may be caused by the area constriction of the holes on the perforated plate and the corresponding local acceleration of the flow there [79].

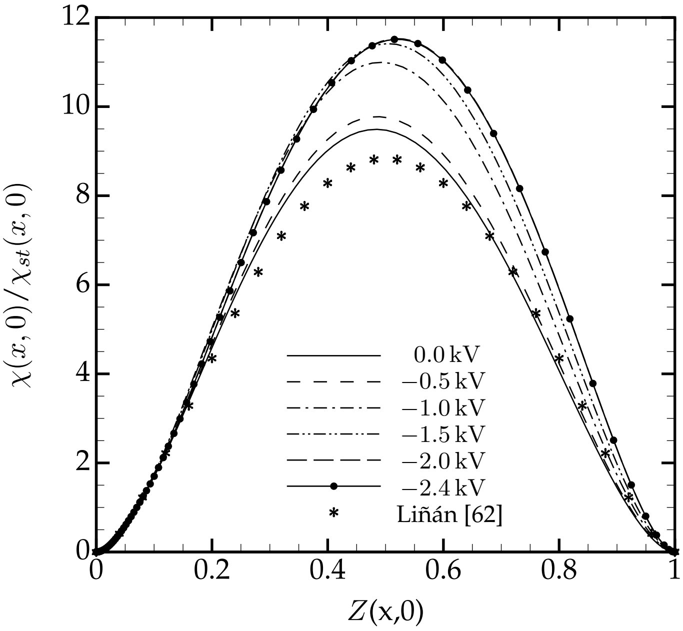

(a) $Z_{st} = 0.07$

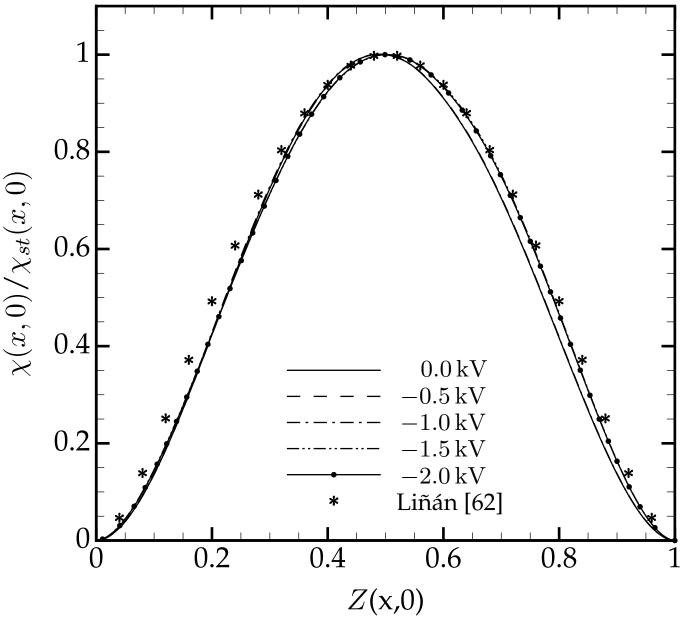

(b) $Z_{st} = 0.50$

FIGURE 3.17: Normalized scalar dissipation rate profiles along the axis of the burner for $Z_{st} = 0.07$ and $Z_{st} = 0.50$. The curves for -2.0 and -2.4 kV (in panel a), 0.0, -0.5 and -1.0 kV (in panel b), and -1.5 and -2.0 kV (in panel b) are almost coincident.

A second important aspect of the comparison made in Figure 3.18 relates to the discrepancies in the electrified cases, where the numerical values of the axial velocity on the oxidizer side are significantly larger than the experimental ones. In particular, the smaller values observed in the experiments appear to be linked with the significant flow blockage caused by the ionic wind on the oxidizer side, which,

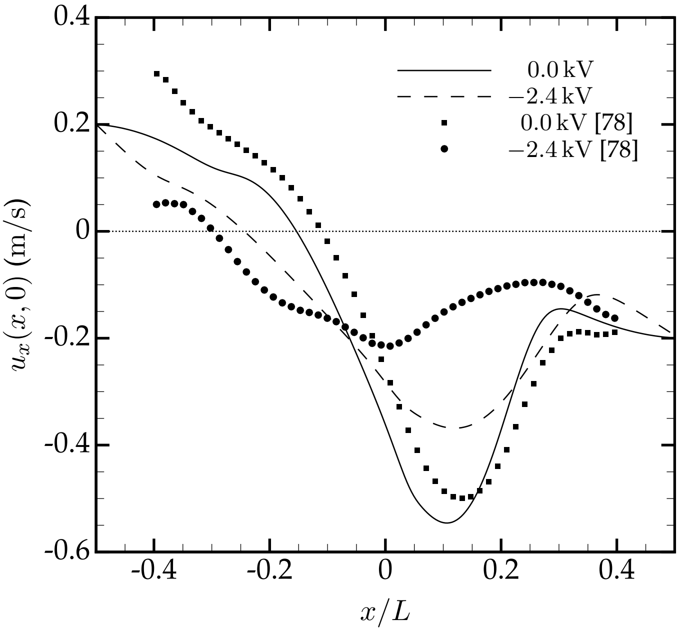

FIGURE 3.18: Comparison between numerical simulations and experimental measurements [78] of the axial velocity profiles along the axis of the burner for Z_{st} = 0.07.

in the experimental cases utilizing propane as fuel, may even lead to the occurrence of a second stagnation plane near the oxidizer injector (e.g., see Fig. 5e in Ref. [78]). Note however that such intense flow modifications were not observed in the present study. One cause of these differences could be related to the effects of the electric charge inadvertently acquired by the tracer particles employed in the PIV to measure experimentally the axial velocity profiles. To see this, consider a number of inertial point particles of TiO_2 with the similar physical properties to those used in the experiments by Park et al. [78], and which are to be seeded below in a one-way-coupled way into the numerical flow fields in a manner analogous to the role played by the PIV tracers in the experiments. In particular, the particles are characterized by their radius $a_{p,i} \sim 0.1\,\mu\text{m}$, material density $\rho_{p,i} \sim 4230\,\text{kg/m}^3$, and electric charge $q_{p,i}$, the latter being treated here as an adjustable parameter since it cannot be easily measured. The associated Stokes number of the particles is $\text{St}_i = (2/9)(\rho_{p,i}/\rho_{ref})a_{p,i}^2 A/\nu_{ref} \sim 5 \times 10^{-4} \ll 1$, indicating that they are mostly tracers of the flow field if their charge is negligible.

The position of the particles, $\mathbf{x}_{p,i}$, is computed from the trajectory equation

$$\frac{d\mathbf{x}_{p,i}}{dt} = \mathbf{u}_{p,i}, \tag{3.7}$$

where the velocity of the particles, $\mathbf{u}_{p,i}$, is obtained by integrating the second Newton's law

$$\frac{4}{3}\pi\rho_{p,i}a_{p,i}^3\frac{d\mathbf{u}_{p,i}}{dt} = 6\pi\rho(\mathbf{x}_{p,i})\nu(\mathbf{x}_{p,i})a_{p,i}\left[\mathbf{u}(\mathbf{x}_{p,i}) - \mathbf{u}_{p,i}\right] + q_{p,i}\mathbf{E}(\mathbf{x}_{p,i}) \tag{3.8}$$

individually for every particle. In Equation (3.8), the last term on the right-hand side refers to the electric force exerted on a charged particle by the incident electric

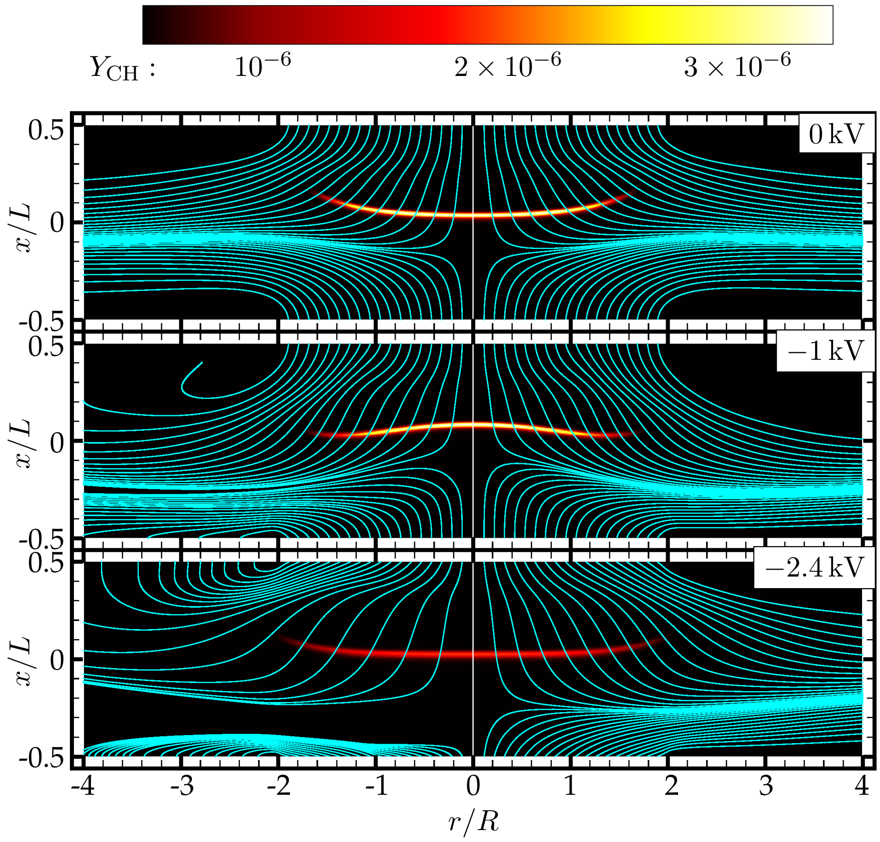

FIGURE 3.19: Comparison of the trajectories of uncharged (right hand side of the figures) and charged (on left hand side) particles for three values of applied voltage on the configuration at $Z_{st} = 0.07$.

field, which in principle makes the particle depart from the trajectories followed by a fluid particle. Additionally the symbol "$(\cdot)(\mathbf{x}_{p,i})$" is associated with the evaluation of the corresponding Eulerian field at the position of the particle. This evaluation is performed using a bi-linear interpolation inside the grid cell containing the particle. Interactions between particles are neglected because of the high dilution employed. The particles are seeded in kinematic equilibrium with the flow at the fuel and oxidizer orifice. The values of $q_{p,i}$ employed in the simulations are $q_{p,i} = \pm 10^{-17}$ C for $Z_{st} = 0.07$, and $q_{p,i} = \pm 1.6 \times 10^{-17}$ C for $Z_{st} = 0.50$, which amount approximately to just 200 elementary charges per particle, with positive and negatively charged particles being injected at the fuel and oxidizer inlets, respectively.

Figures 3.19 and 3.20 provides the particle trajectories $\mathbf{x}_{p,i}$ obtained by simultaneously integrating Eqs. (3.7)-(3.8), and illustrates the sensitivity of the solution to the electric charge $q_{p,i}$. For instance, for zero charge, the particles become tracers of the flow field independently of the applied voltage, as easily observed by comparing the right panels in Figures 3.15 with those in Figure 3.20. In contrast, when the particles are charged, the trajectories differ significantly from the streamlines in both undiluted and diluted cases, as observed in the left panels in Figures 3.19 and 3.20. Note that the particle charge has been chosen to lead to comparable values of the characteristic values of the electric force, $q_{p,i}|\Delta\Phi_{ref}|/L$, and the viscous force based on the injection velocity, $6\pi\rho_{ref}\nu_{ref}a_{p,i}U$. The ratio of these two forces is associated

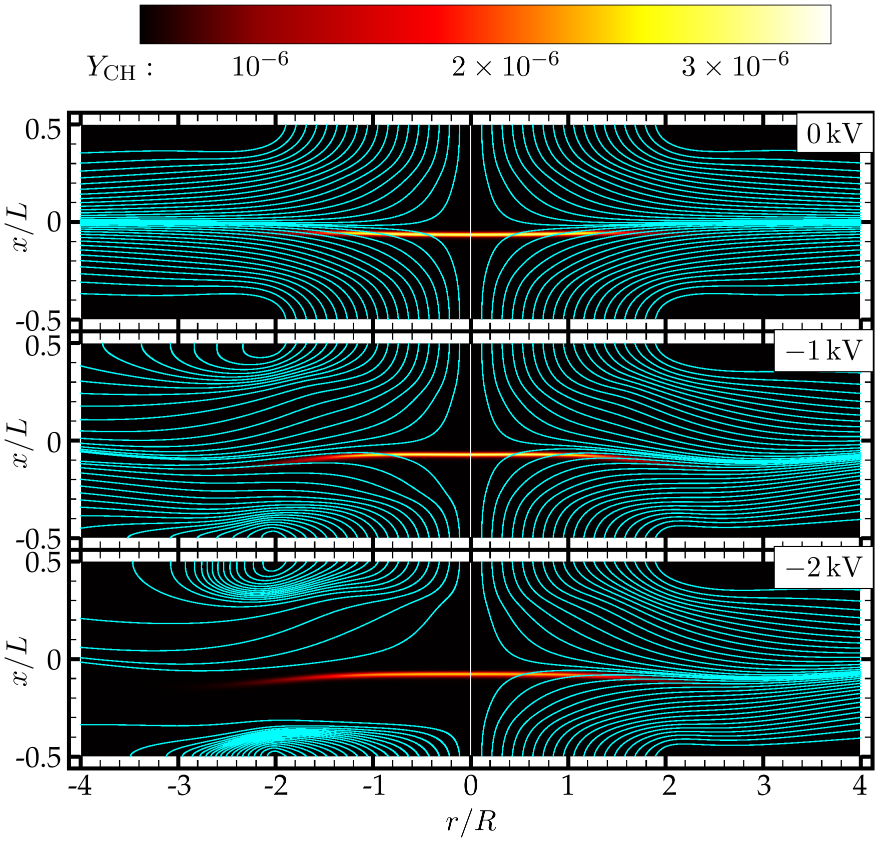

FIGURE 3.20: Comparison of the trajectories of uncharged (right hand side of the figures) and charged (on left hand side) particles for three values of applied voltage on the configuration at $Z_{st} = 0.5$.

with an electric Stokes number,

$$\mathrm{St}_{el} = |q_{p,i}||\Delta\Phi_{ref}|/(6\pi\rho_{ref}\nu_{ref}a_{p,i}UL), \tag{3.9}$$

whose value is within the range $\mathrm{St}_{el} \sim 0.07 - 0.34$ in the present calculations, thereby indicating that the electric force becomes of the same order as the aerodynamic force on the particles even outside the mixing layer. As shown in Figures 3.19 and 3.20, this particular choice of parameters leads to rolled-up trajectories of the negatively charged particles injected on the oxidizer side, and creates a pattern of fictitious streamlines that curves upwards (on the oxidizer side) and downwards (on the fuel side) and is reminiscent of the ones observed in the experiments (e.g., see Fig. 12b in Ref. [78]). These considerations highlight the outstanding challenges related to performing PIV in the type of electrified flows studied here, in which a rather small amount of electric charge attached to the tracer particles can deflect their trajectories and turn them into non-tracers.

Chapter 4

Electrified flamelet model in the mixture fraction space

The previous chapter provided a detailed analysis of the thermo-chemical, hydrodynamic and electrical properties of a counterflow flame. These results were obtained using a detailed model, which inevitably leads to high computational cost for each calculation. In view of making the computation of this kind of flames more affordable, it has been decided to develop a reduced order model.

Previous numerical studies present in the literature about counterflow impinged by an electric field were also based on reduced order models but, conversely with the work that is going to be presented in this chapter, they are derived from experimental evidence of the phenomenon rather than from analytical derivation from the governing equations. In fact, the model proposed by Guerra-Garcia and Martinez-Sanchez [41] is based on a potential flow description of the flow around the flame, where a charged porous disk is used to account for the electric force generated by the flame. Even though the model provides a two-dimensional description of the flow field and gives a good qualitative agreement with the experimental data, it is not suitable to evaluate most of the effects that are present inside a counterflow flame. In fact, the thermo-chemical aspects of this interaction are completely ignored by this model. The approach of Guerra-Garcia and Martinez-Sanchez [41] does not resolve the chemistry of the combustion, imposing the amount of charge present in the flame using compatibility arguments for the electric potential field. Similarly, Xiong et al. [121], who were more focused on the electrical response of the flame rather than the hydrodynamics, considered an ionized layer model. This model transports in a one-dimensional computational domain, corresponding to the axis of the burner, only the charged species produced by the flame. In particular, three transport equations are solved: one for the number density of the positive ions, one for the negative ions and one for the electrons. These equations contribute to the determination of the local charge, which is used in the Gauss-law to determine the profiles of electric potential. The transport properties of the species are considered constant in the entire domain with the heavy ions mobility equal to $2.9 \times 10^{-4}\,\mathrm{m}^2/(\mathrm{V\,s})$ [77, 109] and the electron mobility equal to $0.4\,\mathrm{m}^2/(\mathrm{V\,s})$ [8]. These ions are produced in the so-called ionized layer, which is coincident with the flame and consists in a narrow region of the domain where the ionization reaction rate assumes a Gaussian shape. The rate for the ionization and recombination reactions are imposed as an input of the computation and, therefore, they are independent of the local thermo-chemical composition of the mixture, which is by construction unknown during the computational procedure. This model provided good agreement with the experimental data but is clearly not capable to determine the interaction with the hydrodynamic field and the effect of the complex reactions patterns involving the charged species in a complex environment such as a diffusion flame.

On the other hand, the model proposed in this chapter is strictly based on the equations explained in Section 2.1 using the well-known flamelet approach [85, 88, 114]. In particular, the transport equations will be mapped in the frame of reference of the mixture fraction with the derivation presented in the next section. Then the results of this reduced order model will be compared with those presented in Chapter 3 and, finally, taking advantage of the low computational cost of the reduced order model, a preliminary exploration of the phase-space of the electrified steady-state flamelets will be performed.

4.1 Model formulation

Burke and Schumann [14] were probably the first to show that in a diffusive flame with infinitely fast chemistry, therefore with infinitesimal thickness, a coupling function can be defined as a passive scalar from the reactants mass fractions in order to fully describe the reacting region of the flame. In particular, if the entire combustion process is described by the generalized reaction

$$\nu'_{\mathrm{F}}\,\mathrm{F} + \nu'_{\mathrm{Ox}}\,\mathrm{Ox} \longrightarrow \mathrm{P}, \tag{R4.1}$$

the coupling function is than defined as

$$\beta = Y_{\mathrm{F}} - \frac{\nu'_{\mathrm{F}}}{\nu'_{\mathrm{Ox}}} Y_{\mathrm{Ox}}. \tag{4.1}$$

In this way, $\beta \leq 0$ on the oxidizer side of the flame sheet, where $Y_{\mathrm{Ox}} = -\frac{\nu'_{\mathrm{Ox}}}{\nu'_{\mathrm{F}}}\beta$ and $Y_{\mathrm{F}} = 0$, whereas $\beta \geq 0$ on the other side, where $Y_{\mathrm{F}} = \beta$ and $Y_{\mathrm{Ox}} = 0$. Even though such a description has been proposed for infinitely fast chemistry, it has proved to provide valuable information also for finite-rate chemistry [62]. In fact, if the differential diffusion is neglected and the Fick's law is considered for the diffusion term, the advection-diffusion operator $\mathcal{L}$ reads as

$$\mathcal{L} = \rho\frac{\partial}{\partial t} + \rho\mathbf{u}\cdot\nabla - \nabla\cdot(\rho\alpha\nabla), \tag{4.2}$$

where α is the thermal diffusivity of the mixture, which, according to the unity Lewis number assumption, is also employed for the species mass fraction transport. Calling K_{tot} the rate of the reaction (R4.1), it is possible to write the transport equations of the fuel and oxidizer mass fractions as

$$\mathcal{L}(Y_{\mathrm{F}}) = -\nu'_{\mathrm{F}} W_{\mathrm{F}} K_{tot} \tag{4.3}$$

and

$$\mathcal{L}(Y_{\mathrm{Ox}}) = -\nu'_{\mathrm{Ox}} W_{\mathrm{Ox}} K_{tot} \tag{4.4}$$

Considering that the coupling function production rate has to be zero in the entire domain in order to guarantee its transported scalar properties, it is possible to produce a linear combination of the oxidizer and fuel mass fraction such that

$$\mathcal{L}(\beta) = \mathcal{L}\left(\frac{Y_{\mathrm{F}}}{\nu'_{\mathrm{F}} W_{\mathrm{F}}} - \frac{Y_{\mathrm{Ox}}}{\nu'_{\mathrm{Ox}} W_{\mathrm{Ox}}}\right) = 0. \tag{4.5}$$

The property that distinguishes the coupling function and the mixture fraction is that the second is normalized so that it has unity value in the fuel flow and zero in the oxidizer flow [114]. Considering a system with two inlets, one for the fuel and one for the oxidizer, which will be referred with the subscript 1 and 2, respectively, it is possible to normalize the coupling function obtaining the mixture fraction [6]

$$Z = \frac{\beta - \beta_2}{\beta_1 - \beta_2} = \frac{\gamma Y_{\mathrm{F}} - Y_{\mathrm{Ox}} + Y_{\mathrm{Ox},2}}{\gamma Y_{\mathrm{F},1} + Y_{\mathrm{Ox},2}}, \tag{4.6}$$

where $\gamma = \frac{\nu'_{\mathrm{Ox}} W_{\mathrm{Ox}}}{\nu'_{\mathrm{F}} W_{\mathrm{F}}}$. This definition can still be used if this assumption of single step chemistry is relaxed employing multi-step chemistry in the thin reacting layer regime. In fact, the mapping error due to the presence of the intermediate species is confined to a very small region of the flame and does not affect the overall performance of the model. If the detailed chemistry is employed and the thickness of the reacting layer is not negligible in the description of the flame, a more general definition of the mixture fraction is required. Masri et al. [65], considering a skeletal reaction for the combustion process based on the amount of carbon, oxygen and hydrogen atoms composing the mixture, namely

$$\nu'_{\mathrm{C}}\, \mathrm{C} + \nu'_{\mathrm{O}}\, \mathrm{O} + \nu'_{\mathrm{H}}\, \mathrm{H} \longrightarrow \mathrm{P}, \tag{R4.2}$$

defined another coupling function

$$\mathcal{L}(\beta) = \mathcal{L}\left(\frac{Z_{\mathrm{C}}}{\nu'_{\mathrm{C}} W_{\mathrm{C}}} + \frac{Z_{\mathrm{H}}}{\nu'_{\mathrm{H}} W_{\mathrm{H}}} - 2\frac{Z_{\mathrm{O}}}{\nu'_{\mathrm{O}} W_{\mathrm{O}}} \right) = 0, \tag{4.7}$$

where Z_i are the element mass fractions. The renormalization procedure applied in Equation (4.6) leads to the following definition of the mixture fraction:

$$Z = \frac{Z_{\mathrm{C}}/(\nu'_{\mathrm{C}} W_{\mathrm{C}}) + Z_{\mathrm{H}}/(\nu'_{\mathrm{H}} W_{\mathrm{H}}) + 2(Z_{\mathrm{O},2} - Z_{\mathrm{O}})/(\nu'_{\mathrm{O}} W_{\mathrm{O}})}{Z_{\mathrm{C},1}/(\nu'_{\mathrm{C}} W_{\mathrm{C}}) + Z_{\mathrm{H},1}/(\nu'_{\mathrm{H}} W_{\mathrm{H}}) + 2Z_{\mathrm{O},2}/(\nu'_{\mathrm{O}} W_{\mathrm{O}})}. \tag{4.8}$$

It is noteworthy that the definition in Equation (4.8) preserves the same stoichiometric value of mixture fraction (Z_{st}), which is commonly used to describe the structure of these flames, as that in Equation (4.6). The limit of all these mixture fraction definitions is that they are based on coupling functions constructed on mixture elements. In fact, if differential diffusion effects are introduced in the model, both the presented coupling functions do not satisfy the $\mathcal{L}(\beta) = 0$, being the diffusion velocity of each species different from the others. For this reason, Pitsch and Peters [88], generalizing the formulation of the flamelet model in the mixture fraction to problems with differential diffusivity, decided to avoid a direct relation between Z and the mixture composition defining the mixture fraction as a passive scalar that is equal to zero in the oxidizer flow, equal to one in the fuel flow and that is solution of the equation

$$\rho \frac{\partial Z}{\partial t} + \rho \mathbf{u} \cdot \nabla Z - \nabla \cdot (\rho \alpha_Z \nabla Z) = 0, \tag{4.9}$$

where α_Z is the diffusivity of the Z in the mixture. In general, this definition has the drawback of changing the value of Z_{st} [88], but this disadvantage can be recovered assuming that the Lewis number of the mixture fraction (defined as $\mathrm{Le}_Z = \lambda/(\rho \alpha_Z c_p)$) is equal to one.

Using the mixture fraction, it is possible to define its scalar dissipation rate (χ), namely

$$\chi(Z) = 2\alpha_Z |\nabla Z|^2. \tag{4.10}$$

It represents the inverse of the diffusion time scale of the mixture fraction and it is commonly used to characterize non-premixed flames, being their reaction rate mainly limited by diffusion [85].

The flamelet formulation employed in this work is based on writing the transport equations of the species mass fractions, temperature and potential in the frame of reference of the mixture fraction. In general, if the three dimensional physical coordinates (x) are defined as $\mathbf{x} = (x_1, x_2, x_3)$, the transformation can be summarized as

$$(t, x_1, x_2, x_3) \rightarrow (\tau, Z(t, \mathbf{x}), Z_2, Z_3), \tag{4.11}$$

where Z_2 and Z_3 are two curvilinear coordinates locally aligned with the stoichiometric surface. Consequently, the transformation rules for the differential operators are

$$\frac{\partial}{\partial t} = \frac{\partial}{\partial \tau} + \frac{dZ}{dt}\frac{\partial}{\partial Z} \tag{4.12}$$

and

$$\nabla = \nabla Z \frac{\partial}{\partial Z} + \nabla_{Z,\perp}, \quad \text{where} \quad \nabla_{Z,\perp} = \left(0, \frac{\partial}{\partial Z_2}, \frac{\partial}{\partial Z_3}\right)^T. \tag{4.13}$$

Peters [83] analytically showed, using a stretched coordinate, that the derivatives obtained through the operator $\nabla_{Z,\perp}$ are of lower order with respect to those taken along the mixture fraction. In particular, he demonstrated that the ratio between the derivatives in the traversal and normal directions with respect to the stoichiometric surface scales with the inverse of the non-dimensional activation energy of the overall combustion reaction. For this reason, considering that the combustion process analyzed in this work deals with a high dimensionless activation energy, the traversal derivatives with respect to the stoichiometric surface will be neglected.

For instance, using the identity

$$\begin{aligned}\nabla^2 \psi &= \nabla Z \frac{\partial}{\partial Z}\left(\nabla Z \frac{\partial \psi}{\partial Z}\right) \\ &= \frac{\partial}{\partial Z}\left(\frac{\chi \rho \mathrm{Le}_Z c_p}{2\lambda}\frac{\partial \psi}{\partial Z}\right) - \frac{1}{2}\frac{\partial}{\partial Z}\left(\frac{\chi \rho \mathrm{Le}_Z c_p}{2\lambda}\right)\frac{\partial \psi}{\partial Z},\end{aligned} \tag{4.14}$$

which relates the Laplacian of a generic scalar quantity ψ to the corresponding differential operator in the mixture fraction space, on the Gauss equation (2.26), it is possible to obtain the following governing equation for the electric potential in the mixture fraction space:

$$\frac{\partial}{\partial Z}\left(\frac{\chi \rho \mathrm{Le}_Z c_p}{2\lambda}\frac{\partial \Phi}{\partial Z}\right) - \frac{1}{2}\frac{\partial}{\partial Z}\left(\frac{\chi \rho \mathrm{Le}_Z c_p}{2\lambda}\right)\frac{\partial \Phi}{\partial Z} = -\frac{\rho_q}{\epsilon_0}. \tag{4.15}$$

Using, instead, Equations (4.12)-(4.14), the transport equation of Z (Equation (4.9)) and the following relation

$$\begin{aligned}\nabla\left(\psi \alpha_Z \nabla Z\right) &= \nabla Z \frac{\partial}{\partial Z}\left(\psi \alpha_Z \nabla Z\right) \\ &= \frac{1}{4}\left[\frac{d}{dZ}(\psi \chi) + \rho \chi \mathrm{Le}_Z \frac{c_p}{\lambda}\frac{d}{dZ}\left(\frac{\psi \lambda}{\rho c_p \mathrm{Le}_Z}\right)\right],\end{aligned} \tag{4.16}$$

it is possible to write the species mass fraction conservation equation (Equation (2.23)) in the new frame of reference as:

$$
\begin{aligned}
\rho\frac{\partial Y_i}{\partial \tau} = {} & \underbrace{\frac{\rho\chi}{2}\frac{\mathrm{Le}_Z}{\mathrm{Le}_i}\frac{\partial^2 Y_i}{\partial Z^2}}_{1.} + \underbrace{\rho\dot{\omega}_i}_{2.} + \underbrace{\frac{\rho\chi}{2}\frac{\mathrm{Le}_Z}{\mathrm{Le}_i}\frac{Y_i}{W}\frac{\partial^2 W}{\partial Z^2}}_{3.} \\
& - \underbrace{\frac{\rho\chi Y_i}{2}\sum_{k=1}^{N_s}\left[\frac{\mathrm{Le}_Z}{\mathrm{Le}_k}\frac{\partial^2 Y_k}{\partial Z^2} + \frac{Y_k}{W}\frac{\mathrm{Le}_Z}{\mathrm{Le}_k}\frac{\partial^2 W}{\partial Z^2}\right]}_{4.} \\
& + \underbrace{\frac{1}{2}\frac{\partial Y_i}{\partial Z}\rho\chi\frac{\partial}{\partial Z}\left(\frac{\mathrm{Le}_Z}{\mathrm{Le}_i}\right)}_{5.} \\
& + \underbrace{\frac{1}{4}\frac{\partial Y_i}{\partial Z}\left(\frac{\mathrm{Le}_Z}{\mathrm{Le}_i} - 1\right)\left[\frac{\partial}{\partial Z}(\rho\chi) + \rho\chi\mathrm{Le}_Z\frac{c_p}{\lambda}\frac{\partial}{\partial Z}\left(\frac{\lambda}{c_p\mathrm{Le}_Z}\right)\right]}_{5.} \\
& + \underbrace{\frac{1}{2}\frac{\partial W}{\partial Z}\rho\chi\frac{\partial}{\partial Z}\left(\frac{\mathrm{Le}_Z}{\mathrm{Le}_i}\right)\frac{Y_i}{W}}_{6.} \\
& + \underbrace{\frac{1}{4}\frac{\partial W}{\partial Z}\frac{\mathrm{Le}_Z}{\mathrm{Le}_i}\left[\frac{\partial}{\partial Z}\left(\rho\chi\frac{Y_i}{W}\right) + \rho\chi\frac{\mathrm{Le}_Z c_p}{\lambda}\frac{Y_i}{W}\frac{\partial}{\partial Z}\left(\frac{\lambda}{c_p\mathrm{Le}_Z}\right)\right]}_{6.} \\
& - \underbrace{\sum_{k=1}^{N_s}\frac{1}{2}\frac{\partial Y_k}{\partial Z}\rho\chi Y_i\frac{\partial}{\partial Z}\left(\frac{\mathrm{Le}_Z}{\mathrm{Le}_k}\right)}_{7.} \\
& - \underbrace{\sum_{k=1}^{N_s}\frac{1}{4}\frac{\partial Y_k}{\partial Z}\frac{\mathrm{Le}_Z}{\mathrm{Le}_k}\left[\frac{\partial}{\partial Z}(\rho Y_i\chi) + \rho\chi\mathrm{Le}_Z\frac{c_p}{\lambda}\frac{\partial}{\partial Z}\left(\frac{Y_i\lambda}{c_p\mathrm{Le}_Z}\right)\right]}_{7.} \\
& - \underbrace{\sum_{k=1}^{N_s}\frac{1}{2}\frac{\partial W}{\partial Z}\rho\chi\frac{Y_i Y_k}{W}\frac{\partial}{\partial Z}\left(\frac{\mathrm{Le}_Z}{\mathrm{Le}_k}\right)}_{8.} \\
& - \underbrace{\sum_{k=1}^{N_s}\frac{1}{4}\frac{\partial W}{\partial Z}\frac{\mathrm{Le}_Z}{\mathrm{Le}_k}\left[\frac{\partial}{\partial Z}\left(\rho\frac{Y_i Y_k}{W}\chi\right) + \rho\chi\mathrm{Le}_Z\frac{c_p}{\lambda}\frac{\partial}{\partial Z}\left(\frac{Y_i Y_k\lambda}{W c_p\mathrm{Le}_Z}\right)\right]}_{8.} \\
& + \underbrace{\frac{\partial}{\partial Z}\left[\frac{\rho c_p\mathrm{Le}_Z\chi}{2\lambda}\rho Y_i\left(\mathcal{S}_i k_i - \sum_{j=1}^{N_s} Y_j\mathcal{S}_j k_j\right)\frac{\partial \Phi}{\partial Z}\right]}_{9.} \\
& - \underbrace{\frac{1}{2}\frac{\partial}{\partial Z}\left(\frac{\rho c_p\mathrm{Le}_Z\chi}{2\lambda}\right)\rho Y_i\left(\mathcal{S}_i k_i - \sum_{j=1}^{N_s} Y_j\mathcal{S}_j k_j\right)\frac{\partial \Phi}{\partial Z}}_{9.} .
\end{aligned}
\tag{4.17}
$$

The terms 1 and 2 on the RHS of the equation along with the scaled time derivative on the LHS compose the classical formulation of the flamelet equation derived using the Fick's law for diffusion [85]. The term 3 is the correction to the Fick's law in order to include molar diffusion effects. The correction of the diffusion velocity proposed by Coffee and Heimerl [20] is instead taken into account by the term 4. The terms from 5 to 8 modify the diffusion velocity, the molecular diffusion and the two components of the diffusion velocity correction in order to account for the variation of the species Lewis number. All the terms up to the number 8 were already proposed by Pitsch and Peters [88]. The innovative contribution of this work, regarding this equation, lies in the term 9, which account for the electric induced flux of the charged species.

A similar procedure, applied to the energy conservation equation (Equation (2.24)) leads to

$$
\begin{aligned}
\rho\frac{\partial T}{\partial \tau} = & \underbrace{\frac{\rho\chi}{2}\mathrm{Le}_Z\frac{\partial^2 T}{\partial Z^2} + \frac{\rho\chi}{2}\frac{\mathrm{Le}_Z}{c_p}\frac{\partial c_p}{\partial Z}\frac{\partial T}{\partial Z}}_{1.} \underbrace{- \frac{1}{c_p}\sum_{i=1}^{N_s}\rho h_i\dot{\omega}_i}_{2.} + \underbrace{\frac{1}{c_p}\frac{\partial p_{th}}{\partial \tau}}_{3.} + \underbrace{\frac{\rho\chi}{2}\frac{\partial T}{\partial Z}\frac{\partial \mathrm{Le}_Z}{\partial Z}}_{4.} \\
& + \underbrace{\frac{1}{4}\frac{\partial T}{\partial Z}(\mathrm{Le}_Z - 1)\frac{\partial}{\partial Z}\left[\frac{\partial}{\partial Z}(\rho\chi) + \rho\chi\mathrm{Le}_Z\frac{c_p}{\lambda}\frac{\partial}{\partial Z}\left(\frac{\lambda}{c_p\mathrm{Le}_Z}\right)\right]}_{4.} \\
& + \underbrace{\sum_{i=1}^{N_s}\frac{\rho\chi}{2}\frac{\mathrm{Le}_Z}{\mathrm{Le}_i}\left(\frac{c_{p_i}}{c_p} - 1\right)\left(\frac{dY_i}{dZ} + \frac{Y_i}{W}\frac{\partial W}{\partial Z}\right)\frac{\partial T}{\partial Z}}_{5.} \\
& + \underbrace{\frac{\rho\chi\mathrm{Le}_Z}{2\lambda}\sum_{i=1}^{N_s}\rho\mathcal{S}_i k_i Y_i\left(\frac{c_{p_i}}{c_p} - 1\right)\frac{\partial \Phi}{\partial Z}\frac{\partial T}{\partial Z}}_{6.} \\
& + \underbrace{\frac{\rho\chi\mathrm{Le}_Z}{2\lambda}\sum_{i=1}^{N_s}\rho_{q,i}\frac{\partial \Phi}{\partial Z}\left[\frac{\lambda}{Y_i\rho c_p\mathrm{Le}_i}\left(\frac{\partial Y_i}{\partial Z} + \frac{Y_i}{W}\frac{\partial W}{\partial Z}\right)\right]}_{7.} \\
& \underbrace{- \frac{\rho\chi\mathrm{Le}_Z}{2\lambda}\sum_{i=1}^{N_s}\rho_{q,i}\frac{\partial \Phi}{\partial Z}\left[\sum_{k=1}^{N_s}\frac{\lambda}{\rho c_p\mathrm{Le}_k}\left(\frac{\partial Y_k}{\partial Z} + \frac{Y_k}{W}\frac{\partial W}{\partial Z}\right)\right]}_{7.} \\
& + \underbrace{\frac{\rho\chi\mathrm{Le}_Z}{2\lambda}\sum_{i=1}^{N_s}\rho_{q,i}\left(\mathcal{S}_i k_i - \mathcal{S}_j Y_j k_j\right)\left(\frac{\partial \Phi}{\partial Z}\right)^2}_{7.} .
\end{aligned}
\tag{4.18}
$$

The term 1 on the RHS of the equation accounts for the Fourier heat transfer split into the two terms, the first employs the thermal diffusivity to treat the transport using a Fick's law and the second considers the variation of the mixture heat capacity. This term, together with the LHS of the equation and the heat release rate (term 2), composes the standard formulation of the unsteady flamelet equation for the temperature [85]. The generalization of the mixture fraction Lewis number leads to the formation of energy fluxes that are accounted by the term 4. The terms 5 and 6 account for the enthalpy flux due to the molecular and electric diffusion of the species. The Joule heating of the mixture is instead represented by the term 7. The original formulation of Pitsch and Peters [88] for the flamelet equations in the presence of differential diffusion effects already contained the terms from 1 to 5, whereas the terms 6 and 7 are shown for the first time in this work.

The main advantage provided by transforming the frame of reference from the physical to the mixture fraction space is in the description of the solved variables transport phenomena with respect to the hydrodynamics of the flow. In fact, a trivial observation that can be made regarding the transport equations in the mixture fraction space is that they do not include any advective transport term involving the flow velocity. This feature arises during the mapping procedure, when it is possible to cancel all the transport terms corresponding to phenomena that are in common between the mixture fraction and the transported variable (such as the hydrodynamic advection) and to retain only the differences between the fluxes of Z and of the transported variable generated by physical phenomena (such as differential and electric diffusion or chemical production) and boundary conditions that are not in common between the two scalars. For this reason, the only coupling factor with the hydrodynamic field retained in the equations is described by the distribution of the scalar dissipation rate, which describes the local intensity of the mixing process. In this way, a solution of the flamelet equations in the mixture fraction space completely describes the flame generated in the mixing layer by all the possible hydrodynamic configurations able to produce the given scalar dissipation rate distribution. Therefore, in the mixture fraction space, the correct estimation of the combustion process is subjected to the correct representation of the Z field through its scalar dissipation rate. If the distribution of χ is known from previous computations of the same flame (as it will be done in Section 4.2) or by experimental measurements, its value can be directly fed in the Equations (4.15)-(4.18). On the other hand, if the scalar dissipation rate is unknown, as it usually happens during the calculations of the flamelet libraries employed in the FPV models, it is necessary to employ scaling of the scalar dissipation profile with respect to its stoichiometric value.

4.1.1 Application to a counterflow diffusion flame

The derivation the Equations (4.15)-(4.18) has been performed without any particular assumption regarding the geometrical and topological features of the studied flame front other than being formed by the combustion of a univocally defined fuel and oxidizer mixtures. In this work, the derived system of equations will be applied to the prediction of a counterflow burner depicted in Figure 4.1. The system is characterized by two inlets (represented by the gray boxes in the figure), one for the fuel and one for the oxidizer mixture, positioned at the opposite sides of the combustion chamber and create two impinging jets toward the center of the combustion chamber, where the injected components mix and form a flat diffusion flame. The position of the diffusion flame inside the combustion chamber mainly depends on the momentum of the jets at the injection point and on their composition. Two flat electrodes are positioned at the injection points in order to create an electric field normal to the diffusion flame. In this system, the mixture fraction has a unit value at the bottom injector and is null in the oxidizer flow. It undergoes a mixing process which is regulated by the local strain rate of the flow and by its local diffusivity and determines a scaling along the axis that has been qualitatively depicted in the plot on the right-hand side of Figure 4.1. In particular, the region of space where the mixing of Z takes place (hatched and delimited by dot-dashed lines in the figure) defines the computational domain inside the combustion chamber where the Equations (4.15)-(4.18) are valid. The axial dimension of this region ($(\Delta x)_Z$) is related to

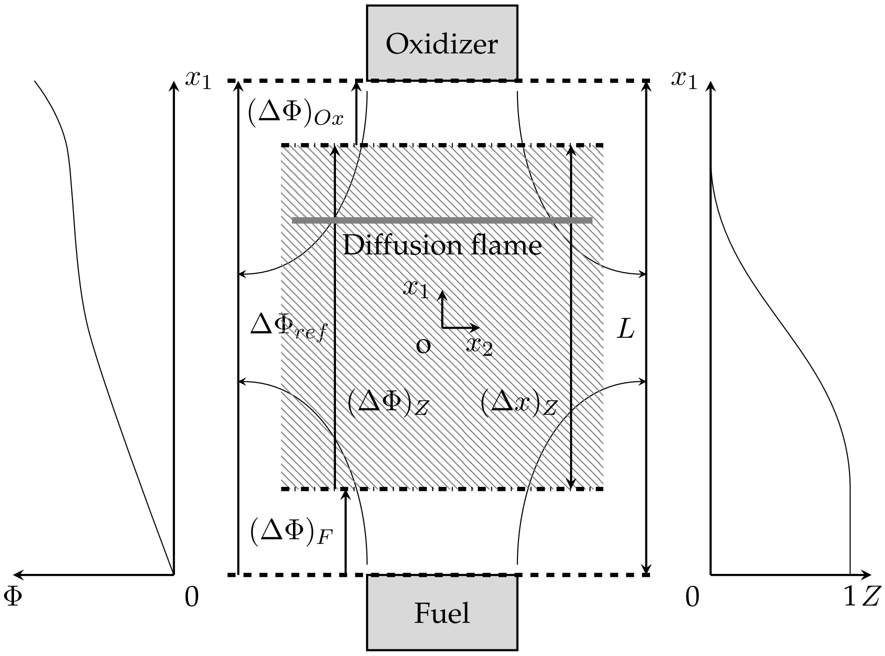

FIGURE 4.1: Schematic of the counterflow diffusion flame configuration with an applied electric field. The dashed lines represent two flat electrodes, whereas the dot-dashed lines delimit the mixing layer of Z.

the mixing layer thickness, defined as $\delta_m = \sqrt{\alpha_{Z,st}/A}$ where $\alpha_{Z,st}$ is the mixture diffusivity at the stoichiometric location along the axis of the burner and A is the strain rate of the flow, considering that the projection of δ_m in the mixture fraction space can be estimated as $(\delta_m)_Z = \sqrt{\chi_{st}/(2A)}$ [85]. To the best of the author's knowledge, Liñán [62] has been the first to provide an analytical solution for the distribution of Z in a counterflow flame in the assumption that the diffusion flame happens inside a potential flow with constant density, unity mixture fraction Schmidt number and unity Chapman-Rubesin parameter (CR $= \rho u/(\rho u)_\infty$). In these assumptions, the local scalar dissipation rate can be computed as

$$\chi(Z) = \frac{A}{\pi} \exp\left[-2\,\mathrm{erfc}^{-1}(2Z)^2\right], \tag{4.19}$$

where erfc^{-1} is the inverse complementary error function [84]. Later, Kim and Williams [53] used an asymptotic analysis in order to obtain a similar expression for variable density flows, namely

$$\chi(Z) = \frac{A}{4\pi} \frac{3\left(\sqrt{\rho_\infty/\rho}+1\right)^2}{2\sqrt{\rho_\infty/\rho}+1} \exp\left[-2\,\mathrm{erfc}^{-1}(2Z)^2\right]. \tag{4.20}$$

The subscript $(\cdot)_\infty$ indicates that the quantity is computed in the oxidizer jet. If the scalar dissipation rate at the stoichiometric location is imposed as an input parameter of the calculation a scaling for the local value of χ can be extracted by one of the two proposed function, closing the system of equations in the mixture fraction space.

Particular attention is required in describing the meaning and limitations of the electric potential modeling in the mixture fraction space. In Chapter 3, it has been pointed out multiple times that the electric potential distribution in the combustion chamber and of its related phenomena evolve with length scales of the order of the outer scales of the problem (such as the electrodes distance or the integral hydrodynamic acceleration). For instance, the electric force profiles along the axis of the burner obtained in the detailed simulations (see Section 3.5.3) are characterized by a plateau of almost null electric force around the flame region, whereas the major contribution of the electric field to the hydrodynamics is located between the edges of the flame and the jets injection points. This led to the use of the outer scales quantities, such as the integral hydrodynamic characteristic acceleration, to perform the dimensional analysis of the phenomenon. Such a behavior of the problem may suggest that the mixture fraction space, which, by construction, is particularly suitable to describe phenomena that happen in the mixing layer, cannot be employed. On the other hand, it is noteworthy that these electric effects, analyzed in Chapter 3, are determined by phenomena, such as the chemi-ionization, that happen inside the reacting layer of the flame, which, instead, is well described in the mixture fraction space. Moreover, considering that this formulation of the problem does not directly involve the hydrodynamics of the flow, which is completely represented by the distribution of the scalar dissipation rate, it becomes clear that the correct representation of the flame in the mixture fraction space becomes just a problem of imposing the appropriate profile of scalar dissipation rate and boundary conditions of the electric potential to the mixture fraction domain. Thanks to the low intensity of the electric forces inside the mixing layer, the scaling of χ is marginally affected by the presence of the electric field (see Section 3.5.4) and, in the absence of more precise data, the scalings in Equations (4.19) and (4.20) can be considered as reasonable approximations. The definition of the boundary conditions for the electric potential at the edge of the mixture fraction domain is less trivial. In non-reacting cases the electric potential would have a linear variation between the two electrodes in the physical space and therefore the voltage applied at the edge of the mixture fraction domain ($(\Delta\Phi)_Z$) could be easily estimated scaling the potential difference applied to the electrodes ($\Delta\Phi_{ref}$) using the ratio $(\Delta x)_Z/L$. When a flame is present between the electrodes, the electric potential field is modified by the charged particles produced inside the reacting region (a qualitative behavior of the electric potential distribution along the axis of the burner is provided in the plot on the left-hand side of Figure 4.1). In particular, the shape of the electric potential field is determined by the position of the flame inside the combustion chamber and by the amount of charged species that flow from the flame toward the electrodes. In the mixture fraction space, it is not possible to account for outer scales quantities such as the distance of the electrodes from the flame. On the other hand, the total applied voltage can be divided in $(\Delta\Phi)_F$, $(\Delta\Phi)_Z$ and $(\Delta\Phi)_{Ox}$ representing the potential differences between the fuel side electrode and the respective mixture fraction domain side, the voltage across the mixture fraction domain and the potential difference between the oxidizer side of the mixture fraction space and the remaining electrode. $(\Delta\Phi)_F$ and $(\Delta\Phi)_{Ox}$ cannot be represented in the mixture fraction space since they happen in a region where the $\nabla Z = 0$, therefore where the relation defined in (4.13) becomes inapplicable leading to the presence of two singularities in the electric potential profiles at the borders of the Z domain. These two electric potential differences are not coincident, by construction, with the mixing layer, therefore they do not directly influence the species distribution in the surroundings of the flame. Consequently, it is possible to solve the electric potential distribution in the mixture fraction space excluding these singularities and imposing the $(\Delta\Phi)_Z$ voltage to the boundaries of the integration domain. Unfortunately, the non-linear physics that determines the charge distribution inside the combustion chamber makes the construction of an analytical relation between $\Delta\Phi_{ref}$ and $(\Delta\Phi)_Z$ impossible. For this reason, previous calculations or experimental data are always required by this model in order to match an experimental configuration imposing the correct electric potential difference in the mixture fraction domain.

4.1.2 Numerical procedure

A modified version of the finite difference flamelet solver provided with the C++ code FlameMaster [87] has been created in order to include the additional terms presented due to the electric diffusion in the mixture fraction space. A second-order centered finite difference scheme is used for all the differential terms of the equations derived in the previous section.

Dirichlet boundary conditions are used to impose the temperature and the mixture composition of the oxidizer and fuel jets to the respective equations. The mass fractions of the remaining neutral species are set to zero. The difference of potential imposed at the mixture fraction layer thickness is imposed considering a Dirichlet boundary condition for the Equation (4.15). According to what has been discussed in Section 3.4 regarding the definition of the electrodes boundary conditions for the charged species transport equations, the mass fractions of these species is set to zero to prevent any unrealistic flux of ions released by the electrode. On the contrary, if the drift velocity of the species is such that it is flowing toward the electrode, its mass fraction is extrapolated with a first-order scheme. The zero gradient condition used in the simulations presented in Chapter 3 has been avoided in this model because it produces unphysical discontinuities on the first derivatives of the charge density profile in the mixture fraction space. Such a difference is justified by the complex differential operator used in the mixture fraction space, which requires non-trivial boundary conditions in order to correctly represent the flux of ions produced through the boundary of the mixture fraction domain by the electric field. Further investigation on this aspect of the model is deferred to future works.

The non-linear system of algebraic equations obtained in this way is solved using a Newton solver. The Jacobian matrix is evaluated numerically using a first-order accurate scheme. A line search algorithm is used in order to dump the oscillations of the solver around the solution, whereas a re-meshing algorithm, based on the averaged second derivative of the resolved variables, is employed in order to minimize the number of grid points. The algorithm is stopped when the norm-L_2 of the relative error across the entire integration domain is lower than 10^{-12}.

4.2 Comparison with the detailed simulations

The accuracy of the model described in the previous section has been tested using the same counterflow configuration described in Chapter 3. All the following simulations will, therefore, be conducted using the same chemi-ionization mechanism and the same transport properties of the previous chapter. In order to match the hydrodynamic field and the effect of the electric force described in Section 3.5, the following calculations in the mixture fraction space have been performed using the profile of scalar dissipation rate measured along the axis of the detailed model simulations. Moreover, since the relation between the electric potential difference between the edges of the mixture fraction domain (sketched in Figure 4.1) cannot

TABLE 4.1: Electric potential boundary conditions employed in the flamelet calculations.

	$Z_{st} = 0.07$		$Z_{st} = 0.5$	
$\Delta\Phi_{ref}$ (kV)	$(\Delta\Phi)_Z$ (kV)	$(\Delta\Phi)_{Ox}$ (kV)	$(\Delta\Phi)_Z$ (kV)	$(\Delta\Phi)_{Ox}$ (kV)
-0.5	-0.230	-0.053	-0.140	-0.107
-1.0	-0.300	-0.192	-0.300	-0.302
-1.5	-0.900	-0.300	-0.770	-0.340
-2.0	-1.600	-0.240	-1.170	-0.390
-2.4	-2.000	-0.250	-	-

be analytically related to the voltage applied to the electrodes because of the non-trivial distribution of charge outside the mixing layer, the potential difference imposed in the flamelet calculations has been obtained by the solution of the detailed model. In particular the values of $(\Delta\Phi)_Z$ and the difference between the electric potential of the mixture fraction domain boundary and the electrode on the oxidizer side $(\Delta\Phi)_{Ox}$ are reported in Table 4.1. It is noteworthy that the applied voltage in the mixture fraction domain has two slopes of increase between the sub-saturated states (-0.5 and $-1.0\,\mathrm{kV}$) and the saturated cases (-1.5, -2.0 and $-2.4\,\mathrm{kV}$). In fact, the saturated cases are characterized by the reduction of the Faraday cage effect of the charge peaks described in Section 3.5. Such a reduction lets the electric field to enter the combustion region increasing the electric potential difference that impinges the reacting region of the flame.

All the calculations presented in this section have been conducted using 501 points unevenly distributed in the one-dimensional mixture fraction domain in order to obtain a higher resolution in the regions where the solution profiles reach the highest curvature.

4.2.1 Neutral species chemistry and temperature profile

The profiles of the mixture temperature obtained with the detailed and the flamelet model are plotted in Figures 4.2 and 4.3. The two sets of profiles are in very good agreement for all the applied voltages and in both the considered chemical configurations. The largest discrepancy is present at the temperature peak positioned inside the flame front of the undiluted case ($Z_{st} = 0.07$). This difference decreases from $36\,\mathrm{K}$ to $17\,\mathrm{K}$ increasing the applied voltage at the chamber electrodes from the reference case ($\Delta\Phi = 0.0\,\mathrm{kV}$) to the $-2.4\,\mathrm{kV}$ configuration. Considering that the calculations in the mixture fraction space have a much higher resolution in the flame region with respect to the detailed model simulations, the reason for this mismatch may be attributed to a lack of resolution of the simulations in the physical space. This hypothesis is also corroborated by the trend of this error with respect to the applied voltage. In fact, the configurations with the higher impinging electric field present a lower scalar dissipation rate, which contributes to a widening of the flame region. Because of this widening, the species and temperature profile gradients in the physical space are lower and therefore better captured by the uniform computational grid used in the detailed simulations. In the diluted configuration ($Z_{st} = 0.50$) the profile of temperature is much smoother than in the undiluted case and the two models proposed in this work provide solutions which are mostly coincident with minor deviations of the order $\mathcal{O}(1\,\mathrm{K})$.

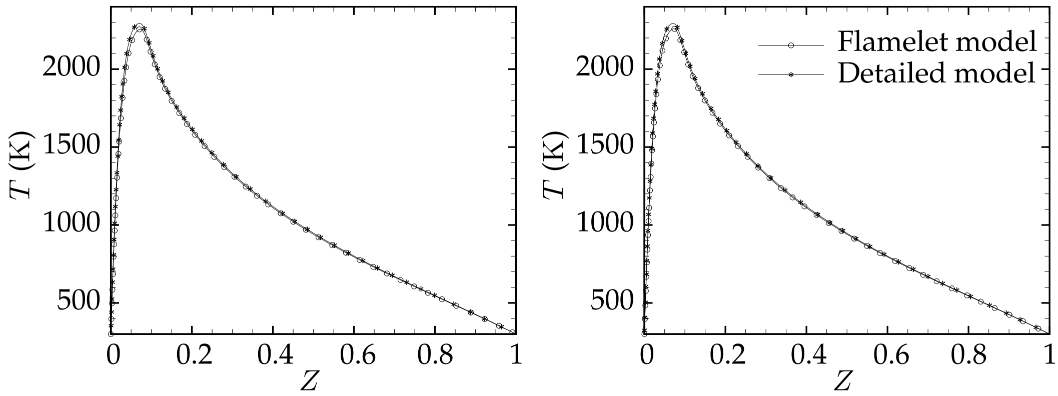

(a) $\Delta\Phi_{ref} = 0.0\,\mathrm{kV}$

(b) $\Delta\Phi_{ref} = -0.5\,\mathrm{kV}$

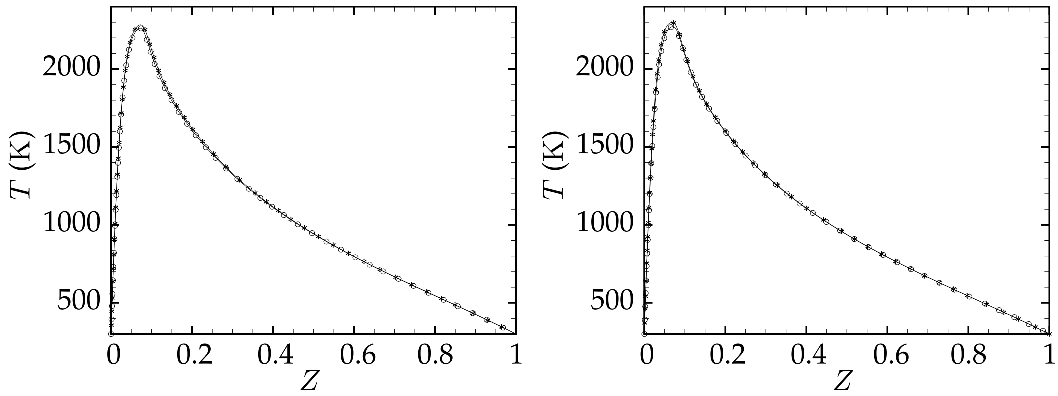

(c) $\Delta\Phi_{ref} = -1.0\,\mathrm{kV}$

(d) $\Delta\Phi_{ref} = -1.5\,\mathrm{kV}$

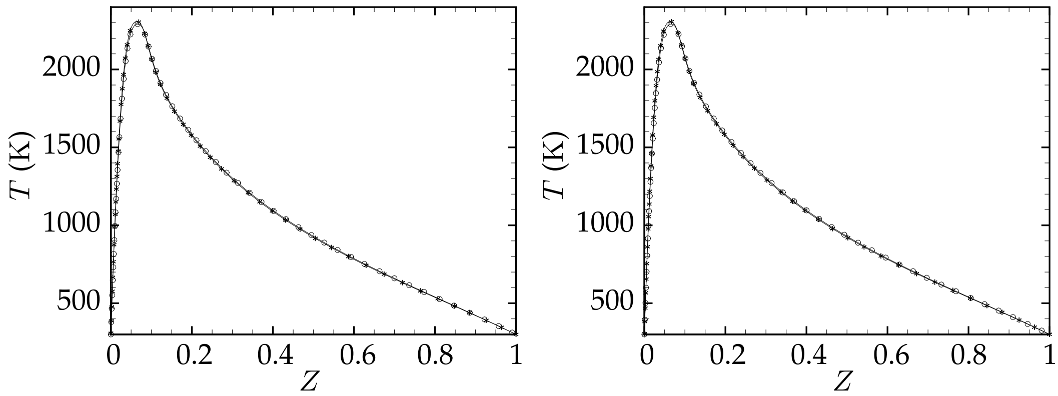

(e) $\Delta\Phi_{ref} = -2.0\,\mathrm{kV}$

(f) $\Delta\Phi_{ref} = -2.4\,\mathrm{kV}$

FIGURE 4.2: Comparison of the temperature profiles obtained with the detail simulation of Chapter 3 and the flamelet model for the configuration with $Z_{st} = 0.07$.

The profiles of the molar fractions of the neutral species analyzed in Section 3.5.2 have been compared with the results of the present flamelet model. The plots in Figures 4.4 and 4.5 show that the proposed flamelet model is able to well recover the results obtained in the physical space even for the neutral mixture components. In the undiluted case, the profiles match the behavior of the reference solution for their entire length. The largest differences, which are hardly noticeable in the plots, are between the O_2 profiles in the configurations at 0.0 and $-0.5\,\mathrm{kV}$ and for the CH

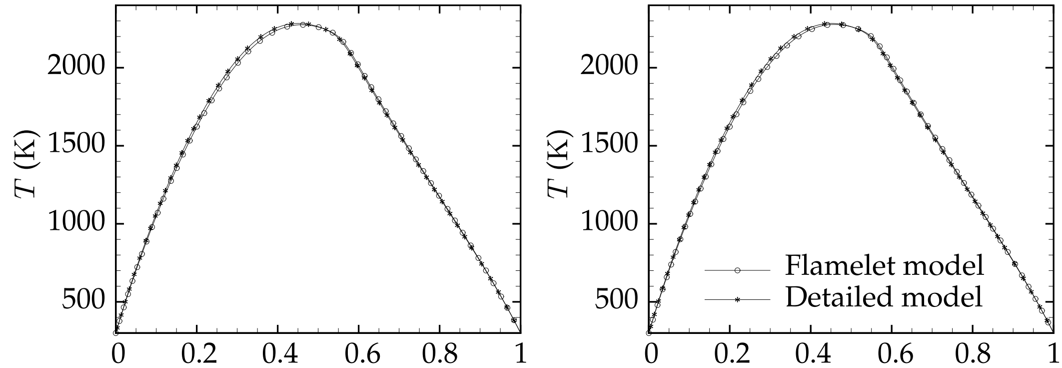

(a) $\Delta\Phi_{ref} = 0.0\,\mathrm{kV}$

(b) $\Delta\Phi_{ref} = -0.5\,\mathrm{kV}$

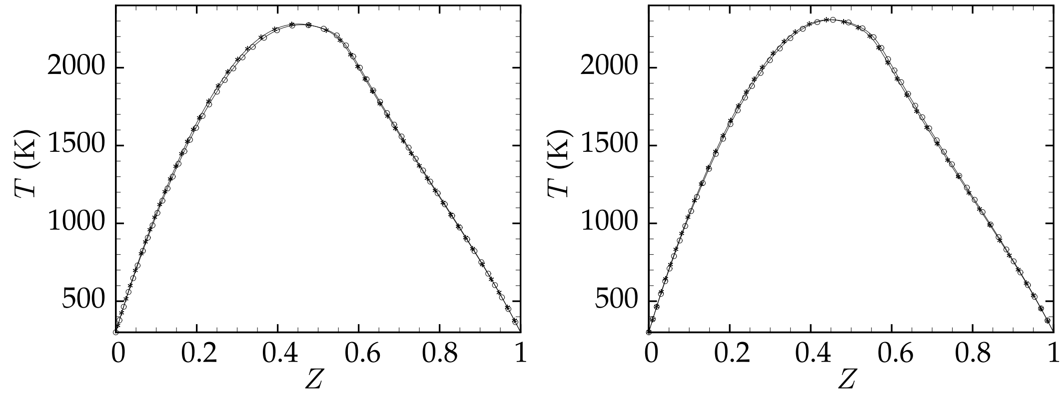

(c) $\Delta\Phi_{ref} = -1.0\,\mathrm{kV}$

(d) $\Delta\Phi_{ref} = -1.5\,\mathrm{kV}$

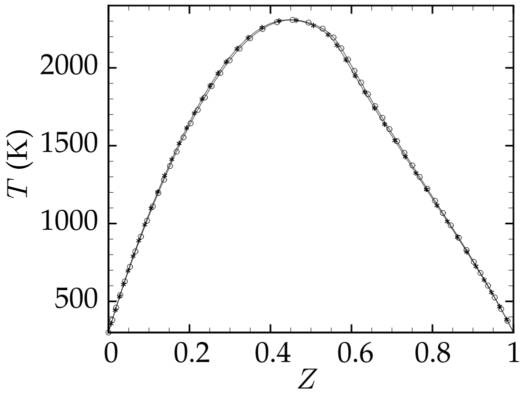

(e) $\Delta\Phi_{ref} = -2.0\,\mathrm{kV}$

FIGURE 4.3: Comparison of the temperature profiles obtained with the detail simulation of Chapter 3 and the flamelet model for the configuration with $Z_{st} = 0.5$.

profiles for the cases at 2.0 and $-2.4\,\mathrm{kV}$. The cases at lower voltage present a small leakage of oxygen from the reacting layer of the order $\mathcal{O}(10^{-4})$. The flamelet model predicts a slightly higher leakage with respect to the computations performed in the physical space, which entails a lower consumption of molecular oxygen in the reacting region. This phenomenon is probably related to differences spotted earlier in the mixture temperature profiles analysis and suggests that the detailed model simulations predict a slightly higher combustion rate for these cases. The profile of the

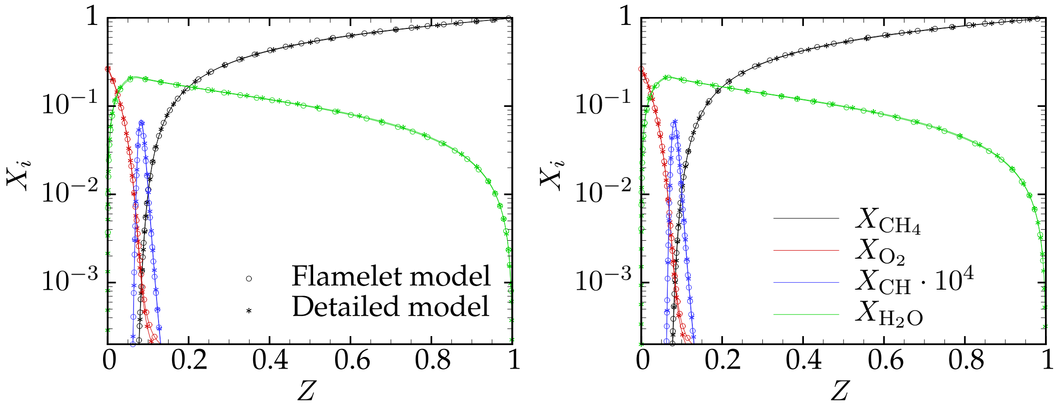

(a) $\Delta\Phi_{ref} = 0.0\,\text{kV}$ (b) $\Delta\Phi_{ref} = -0.5\,\text{kV}$

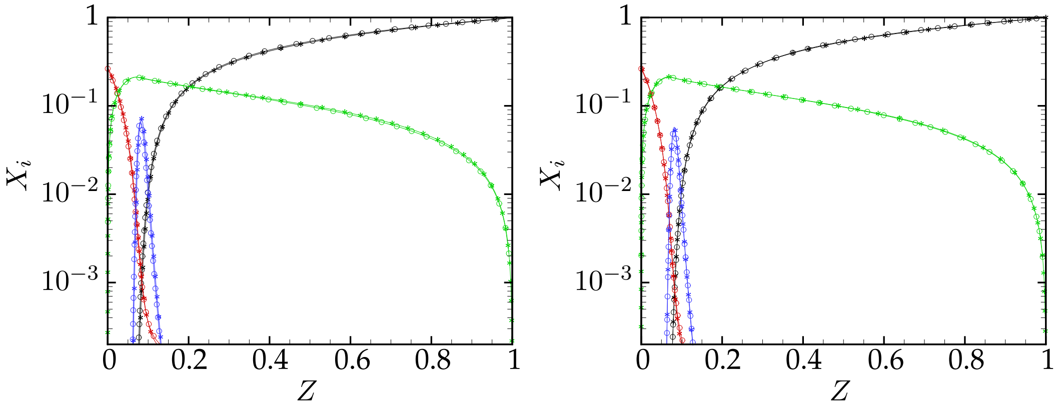

(c) $\Delta\Phi_{ref} = -1.0\,\text{kV}$ (d) $\Delta\Phi_{ref} = -1.5\,\text{kV}$

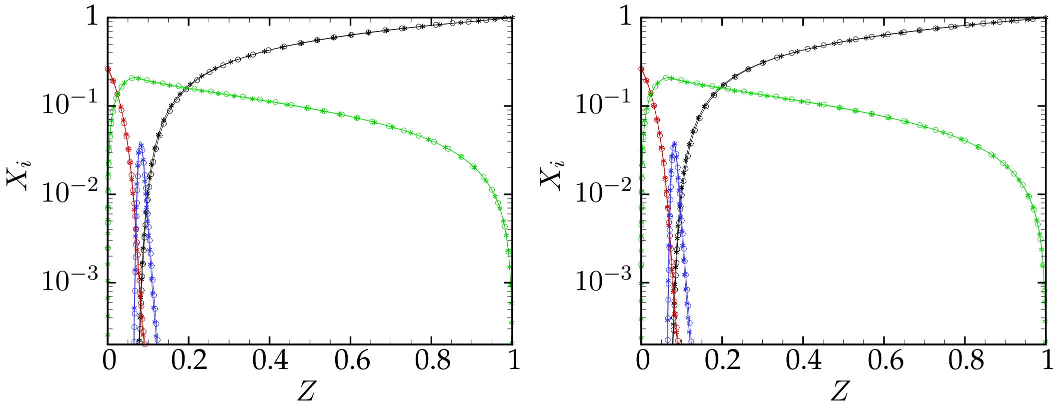

(e) $\Delta\Phi_{ref} = -2.0\,\text{kV}$ (f) $\Delta\Phi_{ref} = -2.4\,\text{kV}$

FIGURE 4.4: Comparison of the main neutral species molar fraction profiles obtained with the detail simulation of Chapter 3 and the flamelet model for the configuration with $Z_{st} = 0.07$.

radical CH, obtained by the decomposition of the methane which looses hydrogen atoms during the oxidation process, is present only in a very narrow region of the domain, coincident with the reacting layer of the flame. An even smaller difference between the two sets of simulations, with respect to what has been described for the oxygen profiles, can be spotted for this species on the right-hand part of its profiles in Figure 4.4e and Figure 4.4f. In fact, the amount of the radical CH predicted by the

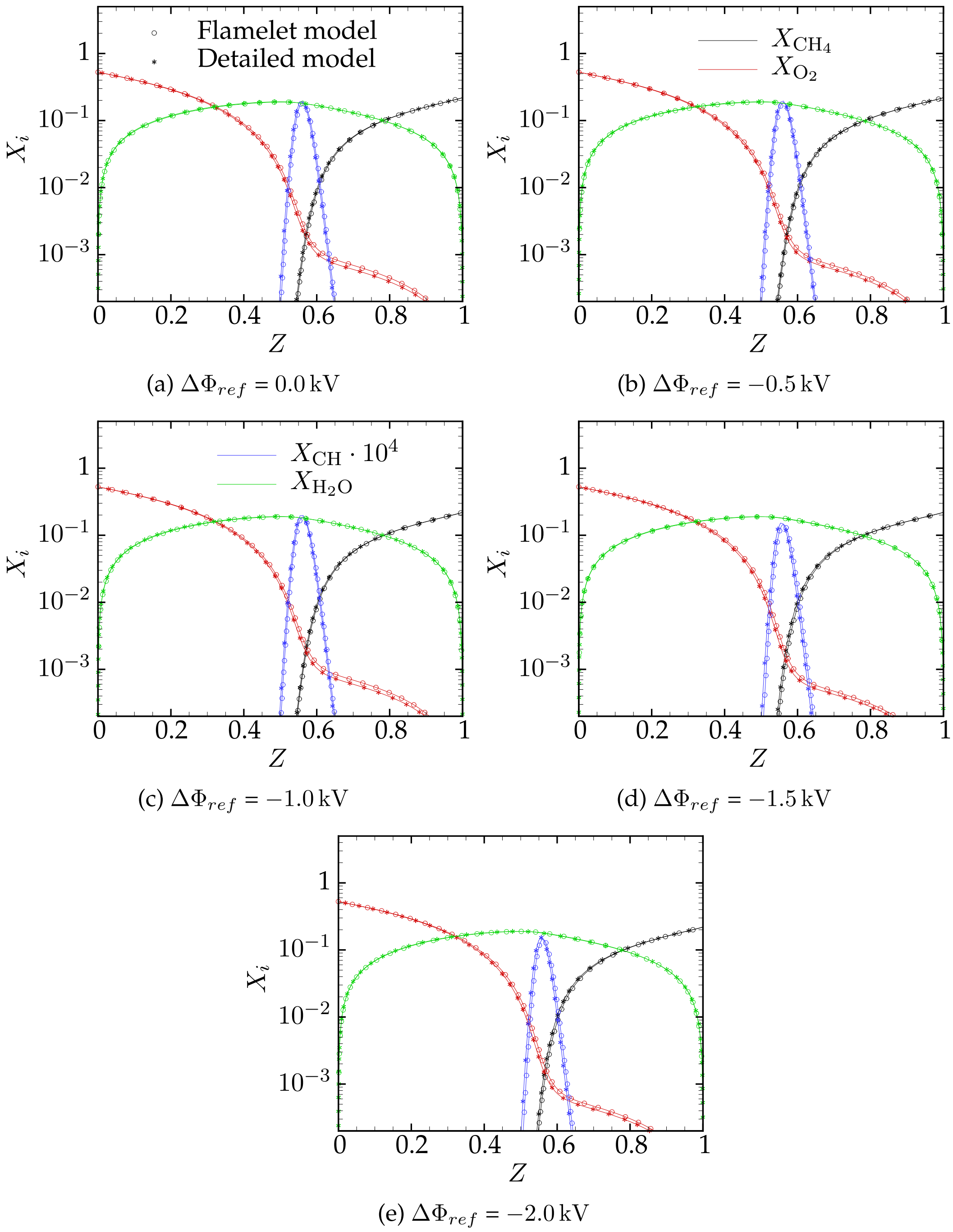

(a) $\Delta\Phi_{ref} = 0.0\,\mathrm{kV}$

(b) $\Delta\Phi_{ref} = -0.5\,\mathrm{kV}$

(c) $\Delta\Phi_{ref} = -1.0\,\mathrm{kV}$

(d) $\Delta\Phi_{ref} = -1.5\,\mathrm{kV}$

(e) $\Delta\Phi_{ref} = -2.0\,\mathrm{kV}$

FIGURE 4.5: Comparison of the main neutral species molar fraction profiles obtained with the detail simulation of Chapter 3 and the flamelet model for the configuration with $Z_{st} = 0.5$.

flamelet calculations seems to be slightly higher than in the detailed model simulations. Similar differences between in the species molar fraction plots are encountered in the diluted configuration. In this case, the leakage of oxygen through the reacting layer is more prominent being it in the order of $\mathcal{O}(10^{-3})$. Also in this case, the flamelet model predicts a slightly higher amount of oxygen on the fuel-rich side of the flame. On the other hand, this difference in the oxygen consumption does not seem to affect the overall combustion process, being the methane and water profiles

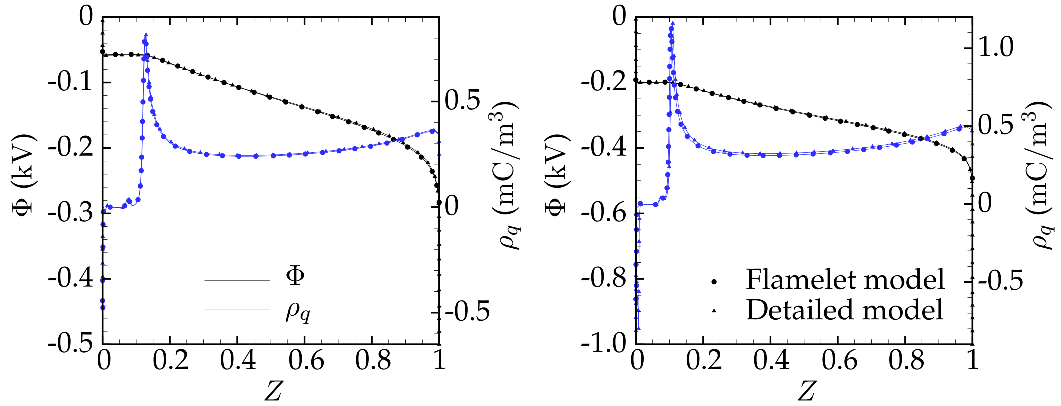

(a) $\Delta\Phi_{ref} = -0.5\,\mathrm{kV}$ (b) $\Delta\Phi_{ref} = -1.0\,\mathrm{kV}$

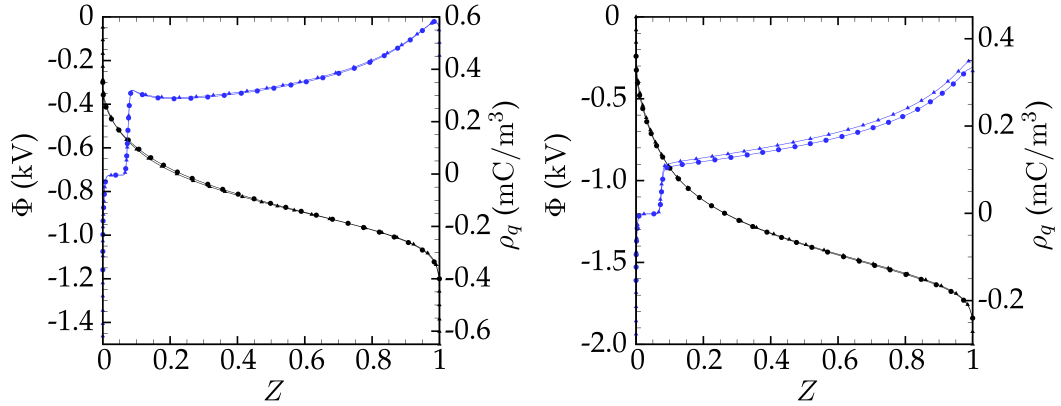

(c) $\Delta\Phi_{ref} = -1.5\,\mathrm{kV}$ (d) $\Delta\Phi_{ref} = -2.0\,\mathrm{kV}$

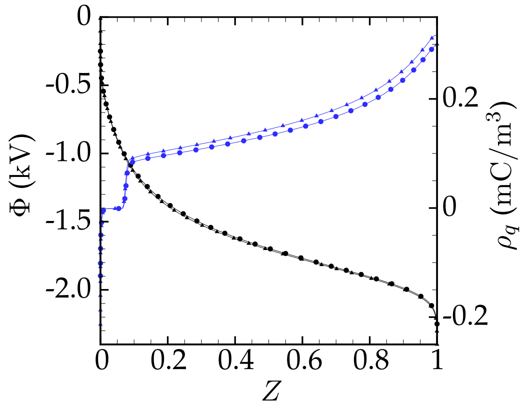

(e) $\Delta\Phi_{ref} = -2.4\,\mathrm{kV}$

FIGURE 4.6: Comparison of the main neutral species molar fraction profiles obtained with the detail simulation of Chapter 3 and the flamelet model for the configuration with $Z_{st} = 0.07$.

perfectly matched. The amount CH produced in the two sets of simulations is very similar between the models, even though a marginal shift of the profile toward the fuel side of the flame can be observed for the flamelet model.

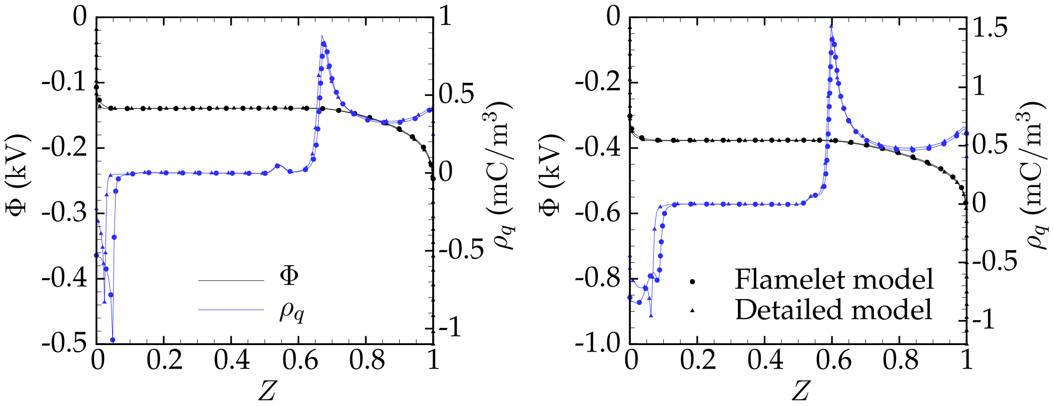

(a) $\Delta\Phi_{ref} = -0.5\,\mathrm{kV}$

(b) $\Delta\Phi_{ref} = -1.0\,\mathrm{kV}$

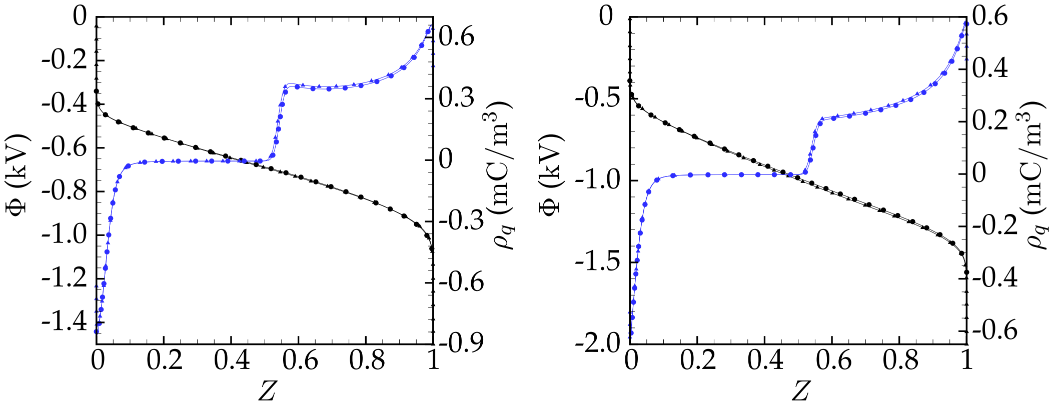

(c) $\Delta\Phi_{ref} = -1.5\,\mathrm{kV}$

(d) $\Delta\Phi_{ref} = -2.0\,\mathrm{kV}$

FIGURE 4.7: Comparison of the main neutral species molar fraction profiles obtained with the detail simulation of Chapter 3 and the flamelet model for the configuration with $Z_{st} = 0.5$.

4.2.2 Charged species profiles

Figures 4.6 and 4.7 show the profiles of electric charge and electric potential obtained with the detailed model and the flamelet formulation for the configuration with $Z_{st} = 0.07$ and $Z_{st} = 0.5$, respectively. A very good agreement between the two model is shown for all the electric potential profiles shown in the figures. Only minor discrepancies are present on the left hand side of the Figures 4.7a and 4.7b corresponding to the subsaturated condition of the configuration with $Z_{st} = 0.5$. These configurations seem to be the most critical for the model in the mixture fraction space since almost the entire electric potential difference applied to the flame is absorbed outside the mixture fraction domain and in a region close to its boundaries. The profile of Φ is, in fact, characterized by a plateau extending from $Z = 0.06$ to $Z = 0.7$. In the region between 0.06 and the left-hand side boundary, the potential profile has a very high curvature linking the horizontal section of the plot with the singularity present on the boundary of the domain. Such a shape of the potential distribution is very demanding from a numerical point of view and probably requires a particular treatment in order to be well captured by the finite difference scheme employed in the present work. In order to preserve the generality of the numerical representation of the system of equations described in the previous section, this solution has been avoided even though it might be a subject of future research. The charge density solutions obtained for the subsaturated conditions ($\Delta\Phi_{ref} = -0.5\,\mathrm{kV}$ and $-1.0\,\mathrm{kV}$) of the case with $Z_{st} = 0.07$ are almost completely superimposed to the solution obtained with the detailed model. In these solutions, it is possible to recognize two positive charge peaks, one located at $Z \sim 0.07$ and the second between $Z \sim 0.12$ and $Z \sim 0.16$, depending on the reference voltage. The first peak is due to the different diffusivity of the electrons with respect to the hydronium and it is coincident with the reacting layer of the flame, where the radical CH is present and the chemi-ionization process takes place. The second peak is instead due to the imposed electric field and it is responsible for the electric potential plateau region present between $Z \sim 0.15$ and the oxidizer boundary of the domain. As shown in Section 3.5.1, these subsaturated configurations are characterized by a negative charge concentration on the oxidizer side of the flame. In the case at $\Delta\Phi_{ref} = -0.5\,\mathrm{kV}$, this charge peak happens outside the mixture fraction domain and, therefore, it cannot be captured by the present flamelet model. The case at $\Delta\Phi_{ref} = -1.0\,\mathrm{kV}$ has, instead, a small portion of the peak inside the mixture fraction boundaries, which is well captured by the flamelet model. The only slight difference between the two models, which can be observed in these two plots, is the slightly lower amount of positive charges present in the case at $\Delta\Phi_{ref} = -1.0\,\mathrm{kV}$ computed with the flamelet model. Considering the entity of this discrepancy between the two models, the error can be attributed to the different resolution employed in the two numerical setups. In the higher voltage conditions of configuration with $Z_{st} = 0.07$ ($\Delta\Phi_{ref}$ from $-1.5\,\mathrm{kV}$ to $2.4\,\mathrm{kV}$) the match between the electric charge profiles of the two models seem to deteriorate increasing the impinging electric field. In fact, the agreement obtained for the case $-1.5\,\mathrm{kV}$ is almost perfect, whereas the flamelet model predicts an increasingly lower concentration of charges for the cases wit $\Delta\Phi_{ref} = -2.0\,\mathrm{kV}$ and $-2.4\,\mathrm{kV}$. This difference between the profiles appears to be determined by the very smooth approach of the electric potential to the singularities present at the boundaries. In fact, in these saturated conditions, the electric potential plot is characterized by a lower curvature distributed in the entire computational domain. Such a curvature increases the complexity associated with the determination of the boundary conditions for the electric potential equation. Considering that the charged species transport in these conditions is dominated by the electric diffusion, a small overestimation of the difference of potential applied to the edge of the mixture fraction domain can easily lead to a lower charged species concentration inside the domain. The subsaturated conditions of the diluted case (Figures 4.7a and 4.7b) show the worst comparison between the two models. All the three charge peaks produced by the flame are resolved in the mixture fraction space but, unlikely the two positive charge peak described earlier, the negative charge density present on the right-hand side of the domain is not well captured by the flamelet model. In the configuration at $\Delta\Phi_{ref} = -0.5\,\mathrm{kV}$, the negative charge concentration is located in the region of $0 \leq Z \leq 0.05$. The proximity of this charge peak to the electric potential singularity on the left boundary determines a wrong estimation of the charge fluxes in the mixture fraction space. This error reflects on the location of the peak and on its intensity. In fact, the solution provided by the flamelet model is characterized by a higher amount of charge located closer to the flame position. This different amount of charge is the reason for the mismatch in the electric potential profiles analyzed earlier. Similar condition is present in the case at $\Delta\Phi_{ref} = -1.0\,\mathrm{kV}$, where the electric charge profiles are coincident far almost the entire mixture fraction domain with the exception of the left end of the domain ($0 \leq Z \leq 0.1$). The agreement between the flamelet and the detailed models is recovered in the saturated configurations of the diluted case ($\Delta\Phi_{ref} = -1.5\,\mathrm{kV}$ and $-2.4\,\mathrm{kV}$) thanks to a better choice of the electric potential boundary conditions with respect to the corresponding configurations of the undiluted case.

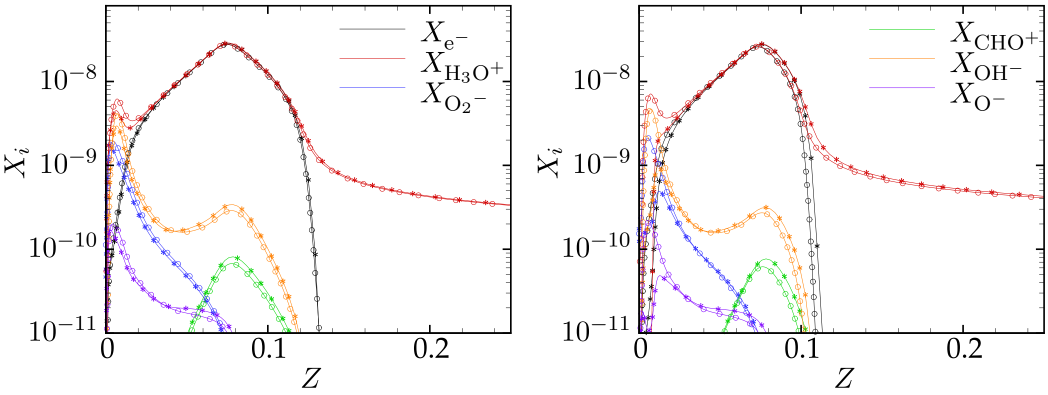

(a) $\Delta\Phi_{ref} = -0.5\,\mathrm{kV}$

(b) $\Delta\Phi_{ref} = -1.0\,\mathrm{kV}$

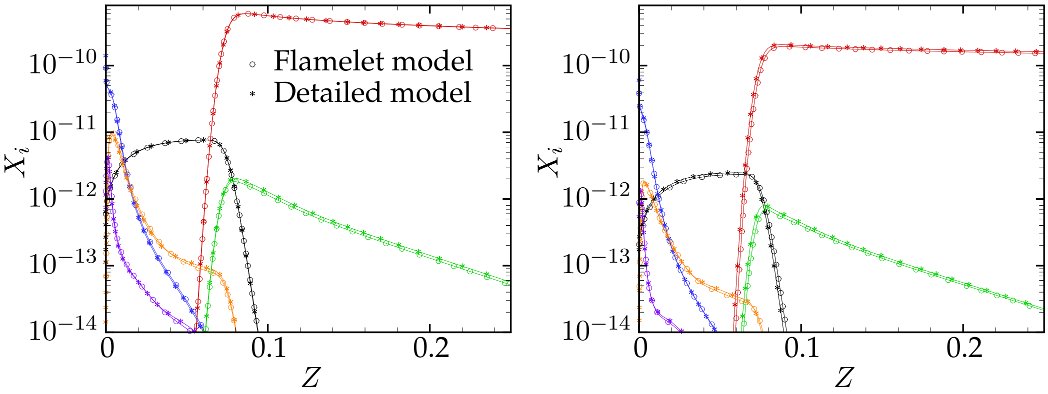

(c) $\Delta\Phi_{ref} = -1.5\,\mathrm{kV}$

(d) $\Delta\Phi_{ref} = -2.0\,\mathrm{kV}$

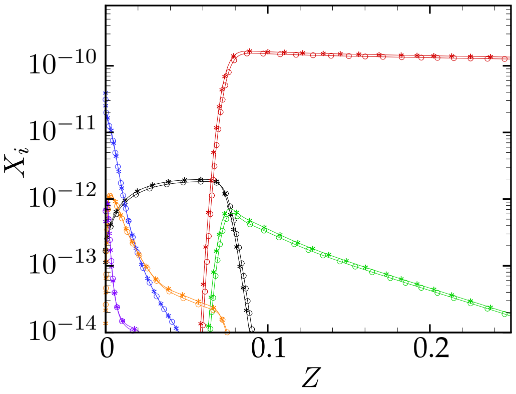

(e) $\Delta\Phi_{ref} = -2.4\,\mathrm{kV}$

FIGURE 4.8: Comparison of the charged species molar fraction profiles obtained with the detail simulation of Chapter 3 and the flamelet model for the configuration with $Z_{st} = 0.07$.

The molar fraction profiles of all the charged species present in the mixture have been provided in Figures 4.8 and 4.9 in order to analyze the contribution of each species to the electric charge density profiles. The match between the two sets of results is better for the saturated regimes in the both the undiluted and diluted cases. In fact, all the species concentration plots are almost coincident in the plots corresponding to the configurations from $\Delta\Phi_{ref} = -1.5\,\mathrm{kV}$ to $-2.4\,\mathrm{kV}$ for the case with

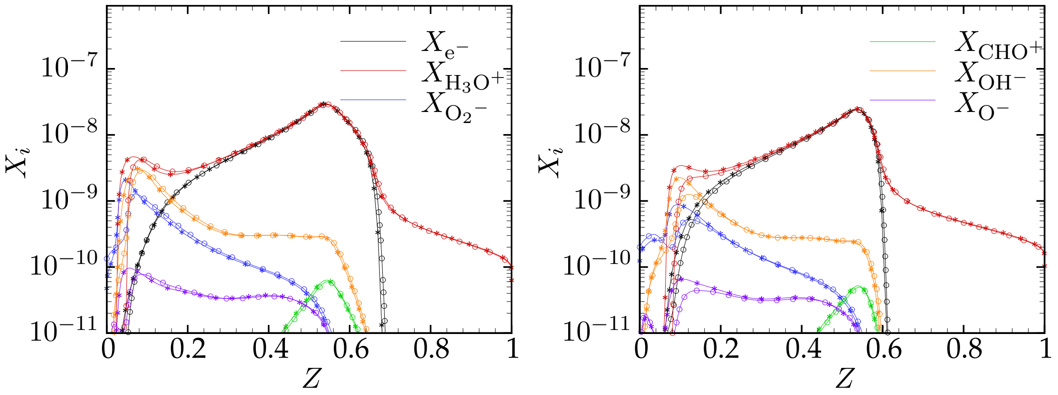

(a) $\Delta\Phi_{ref} = -0.5\,\mathrm{kV}$ (b) $\Delta\Phi_{ref} = -1.0\,\mathrm{kV}$

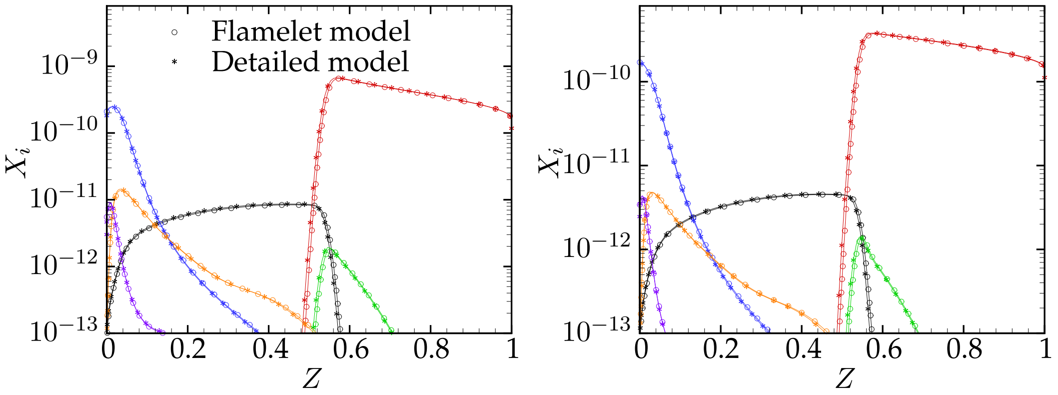

(c) $\Delta\Phi_{ref} = -1.5\,\mathrm{kV}$ (d) $\Delta\Phi_{ref} = -2.0\,\mathrm{kV}$

FIGURE 4.9: Comparison of the charged species molar fraction profiles obtained with the detail simulation of Chapter 3 and the flamelet model for the configuration with $Z_{st} = 0.5$.

$Z_{st} = 0.07$ and to the $\Delta\Phi_{ref} = -1.5\,\mathrm{kV}$ and $-2.0\,\mathrm{kV}$ for the diluted case. Only minor discrepancies are present in the H_3O^+ profiles for the higher voltages of the undiluted case, where the lower electric charge density was observed. The major differences between the two models are observed on the oxidizer side of the flame at $0 \leq Z \leq 0.02$ in the undiluted case and at $0 \leq Z \leq 0.2$ in the case with $Z_{st} = 0.5$. In particular, the flamelet model in the undiluted configuration predicts higher charge species concentrations in case with $\Delta\Phi_{ref} = -0.5\,\mathrm{kV}$ and $-1.0\,\mathrm{kV}$. Being the increase in concentration similar for the positive and negative ions, this discrepancy was not observable in the charge density profiles. Moreover, the magnitude of the difference between the two sets of data increases with the intensity of the impinging electric field, suggesting that it is related to a mismatch in the computed ion wind. Figures 4.9a and 4.9b show that, conversely with the undiluted case, the flamelet model predicts a lower concentration of the ionized species. In fact, in these cases, the electric potential gradient in the mixture fraction space is overestimated by the reduced order model leading to a higher ion flux at the boundary of the domain.

4.3 Electrified S-curves

Thanks to the low computational cost of the presented reduced model, it has been possible to start a preliminary exploration of the flamelet space including the ion-wind effects. Such a procedure is a mandatory requirement for the formulation of flamelet based combustion models for CFD simulations that include the effect of the impinging electric field on the chemistry of a turbulent flame. In particular, the chemical configurations considered in the previous section will be employed ranging the stoichiometric scalar dissipation rate of the flame in its entire range of operating conditions. The influence of the electric field on the χ distribution in the mixture fraction space will be neglected in these simulations employing the scaling in Equation (4.20). A common way of representing a set of steady flamelet solutions is to organize them in the so-called S-curve. For flamelets in the mixture fraction space, it is the curve constructed by plotting the value of the maximum temperature obtained in a flamelet versus the stoichiometric scalar dissipation rate used to obtain the solution. Descending the curve from the highest temperature to the lowest, three branches can be identified [85]: a top branch that is characterized by the stable solution of the flamelet system of equations and it ranges from a null χ_{st} to its quenching value $\chi_{st,q}$; a middle branch that represents all the metastable solutions of the system of the equations comprised between $0 < \chi_{st} < \chi_{st,q}$; a lower branch that includes all the non-reacting mixing solutions of the counterflow system. The plots in Figure 4.10 show a zoom of the quenching region of the S-curves obtained for the diluted and undiluted configuration in the unelectrified case and with an applied voltage across the mixture fraction domain equal to the maximum value tested during the comparison with the detailed model (see Table 4.1). In this way, it has been possible to analyze the effect of an intense electric field, which leads to electrical saturation of the flame, on the entire range of possible operating conditions of the system. As it is shown by the curves in the figure, the neutral chemistry seems to be unaffected by the impinging electric field, confirming the assumption made during the formulation of the FPV models proposed for the interaction of electric fields with diffusive flames [4, 5, 28]. In fact, the ionized species represent a minimal part of the mixture, therefore the chemical pathways of the neutral chemistry cannot be influenced by their flux modification induced by the electric field even on the very sensitive metastable branch. Even though only two voltages are plotted in Figure 4.10, the sensitivity of the S-curve to the impinging electric field has been tested for other values or voltage, reporting identical results.

Thanks to the relatively low computational cost of these simulations, it is possible to investigate the electric response of the flame to the imposed electric field. In particular, the evolution of the electric current density (J) produced by the flame along the S-curve computed with a constant imposed voltage in the mixture fraction domain has been plotted in Figure 4.11. Considering the difficulties of computing the electric diffusion velocity in the mixture fraction space and the unknown mixture velocity at the boundaries, it has been decided to compute J from the integral of the charged species production rate. In fact, considering the summation of all the positively charged species transport equations written in integral form over the entire one-dimensional computational domain, it is possible to define the ion current density that exits a side of the burner as

$$J = N_a e \int_0^1 \sum_{i=1}^{N_s} \frac{\mathcal{S}_i \dot{\omega}_i}{W_i} \bigg|_{\mathcal{S}_i > 0} \sqrt{\frac{2\alpha_Z}{\chi}} dZ. \tag{4.21}$$

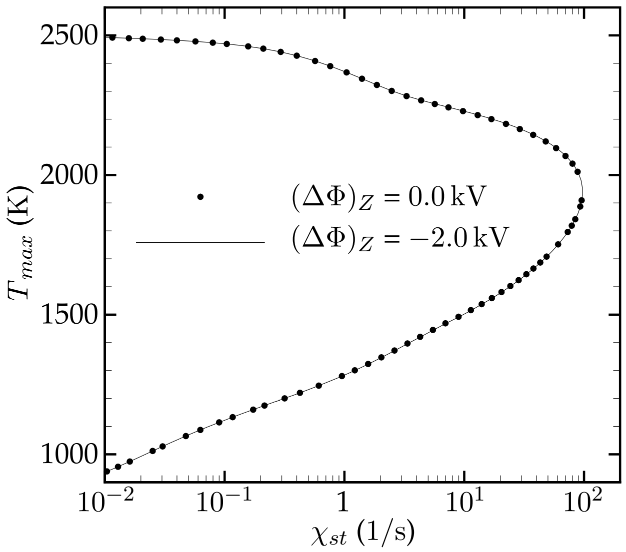

(a) $Z_{st} = 0.07$

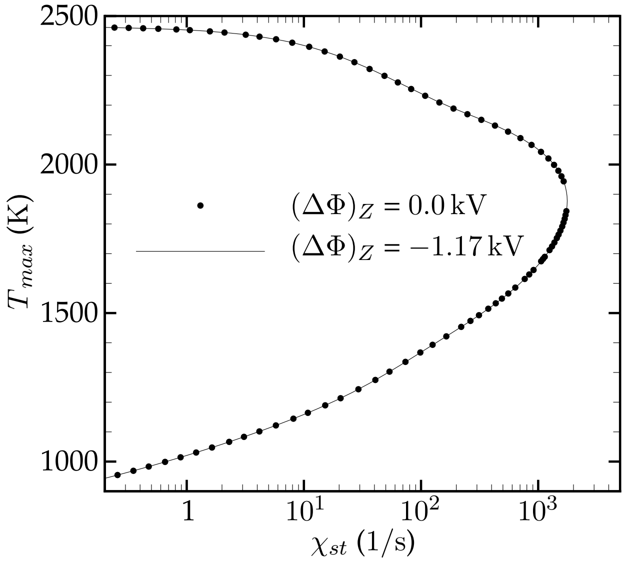

(b) $Z_{st} = 0.5$

FIGURE 4.10: Comparison of the electrified and unelectrified S-curves obtained for two chemical configurations.

Clearly, the calculation performed with $\mathcal{S}_i < 0$ produces exactly the same result because of the charge conservation principle. The three curves presented in the figures refer to the maximum, an intermediate and the minimum value of voltage $(\Delta\Phi)_Z$ of the diluted and undiluted case reported in Table 4.1. All the curves presented in the figures have the shape of closed loops. In fact, all the production rates, comprised those of the charged species, are null in the limit of zero scalar dissipation rate. This condition is reached at the beginning of the upper branch and at the end of the middle branch of the S-curve. Starting from the top of the S-curve and increasing the scalar dissipation rate, initially the electric current density produced by the flame is subjected to increase because of two reasons: the value of the reaction rates $(\dot{\omega}_i)$ of all the species involved in the combustion is increasing because of the

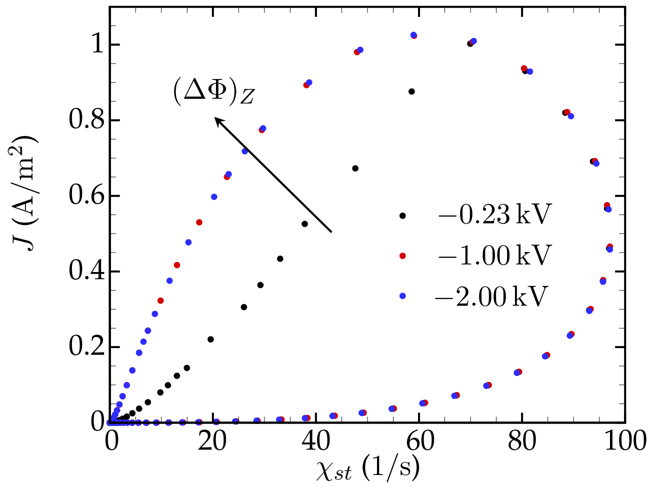

(a) $Z_{st} = 0.07$

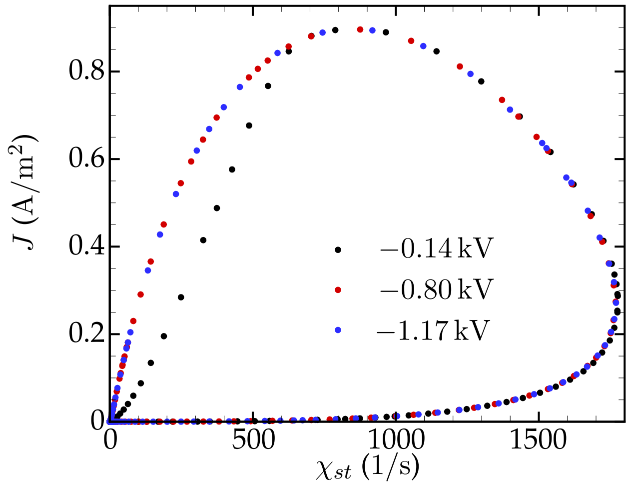

(b) $Z_{st} = 0.5$

FIGURE 4.11: Evolution of the ion-current versus the stoichiometric scalar dissipation rate along the S-curve for two different applied voltages.

increase of the strain rate of the flow; the intensity of the electric field applied to the mixing layer increases being $(\Delta\Phi)_Z$ constant and the value of $(\Delta x)_Z$ inversely proportional to the scalar dissipation rate. This second physical phenomenon is also the reason why the sets of data at lower voltage differ from the others in this region. In fact, varying the applied voltage at the edges of the mixture fraction domain, it is possible to achieve the electrical saturation of the flame (where all the sets of data converge to the same values of current density) at different χ_{st}. For instance, the cases with the higher voltage reach saturation very close to the null value of stoichiometric scalar dissipation rate, draining all the charged species produced by the flame. For this reason, the blue data represent the maximum envelope that these curves can produce for a given chemical configuration. The beginning of the rising branch of the lower voltage data sets presents a lower value of ion-current because it corresponds to sub-saturated conditions, where the charged particles produced in the reacting layer are partially drained by the electric field and partially recombined inside the mixture fraction domain. The decrease in temperature due to the higher diffusive fluxes present at high χ_{st} entails a reduction of the ionization rates inside the reacting layer of the flame. This decrease of the chemi-ionization rates determines a maximum and a consequent decrease of the ion current density profile along the S-curve. The very low temperatures reached by the metastable configurations produced in these chemical configurations are not sufficient to activate significant chemi-ionization processes in the mixture, leading the ion-current density to approach the horizontal axis of the plot at relatively high values of scalar dissipation rate. This reduction of the chemi-ionization processes is a further justification of the independence of the S-curve metastable branch from the applied voltage but, at the same time, it suggests the possibility of incurring in effects of the impinging electric field on the S-curve in chemical configurations where the chemi-ionization is still active in this regimes. Further instigations of this aspect will be subject of future studies along with a more thorough description of the steady electrified flamelet space.

Chapter 5

Flamelet progress-variable model

The models proposed in the previous chapters (especially in Chapter 3) of the thesis provide a very detailed description of the local mixture composition and properties at the expense of the computational time required to solve the entire flow. In order to extend the predictive capabilities obtained so far on simplified laboratory scale configurations, the present chapter will provide an approach oriented to the simplification of the mathematical formulation required to reproduce the effect of an impinging electric field on a flame on complex configurations.

The objective of reducing the number of unknowns and the computational cost required to compute a reacting flow is a classical problem in CFD community especially regarding the modeling of turbulent flames. In this context, a well-established type of models for turbulent combustion is the flamelet based approach proposed by Peters [83]. This approach is based on the assumptions that the Damköhler number is sufficiently high to let the chemistry be much faster than the time scales of the flow and that the reaction layer thickness is much smaller than the Kolmogorov length scale, entailing that the reacting region of the flame is just wrinkled by the turbulence and not directly affected by it. In these assumptions, the flame-front is approximated by an ensemble of steady laminar one-dimensional flames [85]. The main advantage of this approximation is that the one-dimensional flames can be easily computed using detailed chemistry and complex transport models in a pre-processing stage of the calculation. Then, they can be organized in form of a functional manifold able to provide all the mixture properties needed during the computation of the flow field as a function of a reduced number of scalar quantities (e.g. the mixture fraction) that are transported by the CFD solver. One of the most well-known ways of organizing the functional manifold for the mixture properties has been proposed by Pierce and Moin [86]. They, using arguments related to the shape of the s-curves produced by diffusive counterflow flamelets, developed a description of the flamelet space based on the mixture fraction and on a progress-variable (a scalar which measures the degree of completion of the combustion process), which was by the same authors named Flamelet Progress-Variable (FPV) model.

Considering the good predictive capabilities shown by FPV models in a wide range of cases [33, 49, 50, 72, 80, 86], the aim of the present chapter is to develop a model for the interaction of electric field with lifted diffusive flames, completely based on and consistent with the flamelet formulation. Such a formulation guarantees the possibility of using arbitrarily complex mechanisms for both the neutral and charged species, without any computational cost overhead. In the next sections, after the description of the main assumptions and equations employed by the model, two one-dimensional validation tests are presented to assess the capability of the FPV approach to reproduce the results of the corresponding detailed chemi-ionization mechanism; then, a two-dimensional numerical test case using two different kinetic mechanisms is considered to assess the effectiveness of the proposed approach.

5.1 Mathematical model

The FPV formulations rely on the definition of a number of transported scalars that, in conjunction with an appropriate functional manifold (Equation (1.4)), are able to represent all the mixture properties used during the integration of the flow. This procedure allows one to avoid the solution of the mass fraction of each species at run-time, replacing the corresponding equations with those of the defined scalars. Being the number of scalars usually much lower than the number of species, the number of unknowns is reduced with the consequent benefits in terms of computational cost of the simulations. The Navier–Stokes equations (Equations (2.21)-(2.22)) are, therefore, solved in their complete form using the density, the viscosity and the electric force determined as described in the following section. The effects of buoyancy on the mixture have been neglected in these calculations.

5.1.1 Chemistry model

The present approach is based on the flamelet model proposed by Fiorina et al. [32], which uses a set of one-dimensional premixed unstrained flames for solving a detailed mechanism and composing the two-dimensional manifold (Equation (1.4)). The Equations (2.21)-(2.24), coupled with the ideal gas law (Equation (2.25)), are used to compute the distribution of the temperature and of all the neutral and charged species with exception to the electrons, neglecting the electro-diffusion terms. In fact, the mass fraction of the electrons has been calculated imposing the charge neutrality of the mixture with the Equation (2.44). Such an approximation is used only during these pre-processing calculations. In fact, as described in detail in the next sub-section, the present model does not take into account the effect of the electric field on the flamelets. This assumption allows one to simplify the model avoiding the numerical and theoretical complexity of a functional mapping that involves the local electric field strength and direction but, at the same time, determines some limitations in the applied electric field intensity as properly discussed in the following.

Defining the mixture fraction using definition proposed by Williams [114] and the progress-variable as the linear combination of the mass fractions of the main combustion products, it is possible to embed the entire combustion process in a functional manifold. This manifold is populated using premixed unstrained flamelet solutions for a wide range of equivalence ratio and considering the mixture fraction and the progress-variable as independent variables. Therefore, only these two quantities are transported through the computational domain solving the following equations together with Equations (2.21) and (2.22):

$$\frac{\partial \rho Z}{\partial t} + \nabla \cdot (\rho \mathbf{u} Z) = \nabla \cdot (\rho \alpha_Z \nabla Z), \tag{5.1}$$

$$\frac{\partial \rho C}{\partial t} + \nabla \cdot (\rho \mathbf{u} C) = \nabla \cdot (\rho \alpha_C \nabla C) + \rho \dot{\omega}_C. \tag{5.2}$$

The Lewis number for these two scalars is assumed to be equal to one leading to $\alpha_C = \alpha_Z = \lambda/(\rho c_p)$; this quantity is computed and stored in a two-dimensional chem-table along with the chemical source term of the progress-variable, $\dot{\omega}_C$, the mixture density and viscosity.

5.1.2 Charged species transport model

The proposed model for charge transport is based on the assumption that the presence of the electric field does not affect the combustion process of the neutral species. This assumption, which is corroborated by the results shown in Section 4.3, is valid only when the applied electric field is weak enough not to activate non-thermal phenomena due to the presence of free-electrons and when ionized species mass fractions are much smaller than combustion radical ones. On the other hand, this hypothesis strongly simplifies the model, reducing the dimensions of the needed functional manifold, with obvious advantages in terms of computational cost and memory footprint. Moreover, the use of the low-Mach-number formulation of the Navier–Stokes equations has forced to neglect all the effects of the applied electric field on the energy of the system. This assumption is reasonable considering the low ion currents developed in the domain, which would lead to a negligible heating due to the Joule effect. Furthermore, the low amount of charges produced in the flame by chemi-ionization with respect to the neutral species implies that the enthalpy fluxes activated by the electric field would have only a minor effect of the total enthalpy of the system.

Since cations and anions move in opposite directions, when exposed to an electric field, at least two scalar quantities are necessary in order to predict the distribution of positive and negative charges in the domain. Using an approach similar to the definition of the progress-variable, we have employed the two quantities P and M, defined as

$$P = eN_a \sum_{i=1}^{N_s} \frac{\mathcal{S}_i Y_i}{W_i}\bigg|_{\mathcal{S}_i>0} \tag{5.3}$$

and

$$M = -eN_a \sum_{i=1}^{N_s} \frac{\mathcal{S}_i Y_i}{W_i}\bigg|_{\mathcal{S}_i<0} . \tag{5.4}$$

Being P and M linear combinations of species mass fractions, their transport equations read

$$\frac{\partial \rho P}{\partial t} + \nabla \cdot (\rho \mathbf{u} P + \rho k_P \mathbf{E} P) = \nabla \cdot (\rho \alpha_P \nabla P) + \rho\, \dot{\omega}_P \tag{5.5}$$

and

$$\frac{\partial \rho M}{\partial t} + \nabla \cdot (\rho \mathbf{u} M - \rho k_M \mathbf{E} M) = \nabla \cdot (\rho \alpha_M \nabla M) + \rho\, \dot{\omega}_M . \tag{5.6}$$

The additional advective term is due to the force applied by the electric field on the charged particles and it takes into account the different mobility of the species. The mobility of the drifting scalars is modeled using the following mass weighted-average:

$$k_P = \frac{\displaystyle\sum_{i=1}^{N_s} \frac{\mathcal{S}_i Y_i k_i}{W_i}\bigg|_{\mathcal{S}_i>0}}{\displaystyle\sum_{i=1}^{N_s} \frac{\mathcal{S}_i Y_i}{W_i}\bigg|_{\mathcal{S}_i>0}} \tag{5.7}$$

and

$$k_M = \frac{\left.\sum_{i=1}^{N_s} \frac{\mathcal{S}_i Y_i k_i}{W_i}\right|_{\mathcal{S}_i<0}}{\left.\sum_{i=1}^{N_s} \frac{\mathcal{S}_i Y_i}{W_i}\right|_{\mathcal{S}_i<0}}. \tag{5.8}$$

These two expressions are ill-defined far from the flame-front, where the charged species mass fractions, computed in the flamelet environment, are zero; moreover, imposing weak electric fields, the modification of the ions spatial distribution is very small far from the flame-front. For this reason, when the sum of the charged species molar fractions (either positive or negative) is lower than 10^{-30}, $k_{P/M}$ are evaluated as the arithmetical average of the species mobility. As proposed by Fialkov [31], $10^{-4}\,\mathrm{m}^2/(\mathrm{V\,s})$ has been retained as the mobility of heavy cations and anions, whereas the electron mobility has been estimated as $1.868 \times 10^{-2}\,\mathrm{m}^2/(\mathrm{V\,s})$ using the formula proposed by Belhi et al. [5]. As already pointed out in literature, this value is less accurate than the estimate of Bisetti and El Morsli [8], but it ensures a lower computational cost reducing the electron velocity through the domain. With the aim of evaluating the prediction capability of the formulated reduced FPV model, in the absence of detailed experimental data, this approximation appeared appropriate; in fact, the computational burden associated with the adoption of a more accurate and complex mobility model, leading to higher mobility values, would not have any significant information to the present work. The evaluation of the result sensitivity to the accuracy of the mobility model of cations, anions and electrons is highly relevant but it is beyond the scope of the present work and is deferred to future studies.

The same averaging procedure has been applied to predict the diffusivity of the two scalars, P and M. The diffusivity of the heavy charged species has been set equal to that of their corresponding neutral, whereas the Einstein relationship (Equation (2.41)) is used to model the electron diffusion coefficients. When the average operator is ill-defined, the drifting scalar diffusivity has been approximated with the thermal diffusivity.

The present model neglects the influence of the electric field on the combustion process. This is acceptable for weak electric fields; however, particular attention must be paid to the evaluation of the production terms of P and M, being the recombination process of the charges strongly dependent on the local charge balance [43]. In fact, computing these terms as a simple linear combination of the production rates of the corresponding species can lead to large errors in the prediction of the charge distributions. This is due to the presence of the electric drift in Equations (5.5) and (5.6) which renders the transport of these scalars very different from the conditions considered in the flamelet environment. In fact, the ion-wind is not taken into account when generating the flamelet chem-table, since the steady flamelet equations are solved neglecting the coupling with the electric field and its interaction with the charged species; therefore, in order to be consistent with the manifold used for all the other terms, it is necessary to define an appropriate scaling for the two production rates ($\dot{\omega}_P$ and $\dot{\omega}_M$), taking into account the concentration of positive and negative charges computed at run-time. The scaling used here is inspired by the work of Ihme and Pitsch [48] about the prediction of nitric oxide concentration using an FPV model.

The general model reaction for the production/depletion of ions has the form:

$$R' + R'' + ... \rightleftharpoons P^+ + P^- + P' + ... \tag{5.9}$$

where several neutral species (R', R'', …) react to produce positively and negatively charged particles (P^+ and P^-) as well as other neutrals (P', …). From now on, the procedure will be explained for a reaction where the forward direction produces the ions and backward direction consumes them. It is trivial to extend this procedure to reactions where only one direction is allowed. The charge transfer reactions are not considered in the procedure because they do not lead to a change in the total positive or negative charge, but only to a change of the mixture composition. The forward reaction rate will always depend on the fluid properties and on the concentrations of the neutral species. Therefore, under the assumption that the electric field does not have any effect on the neutral chemistry, the forward reaction rate can be kept constant for all the P and M values. A positive production term of the charges for the j-th reaction is defined as

$$\dot{\omega}_j^+ = eN_a K_{fr,j} n_c, \tag{5.10}$$

where $K_{fr,j}$ is the forward reaction rate of the j-th reaction and n_c is the number of cations or anions produced by the reaction. For the conservation of charges, Equation (5.10) can be applied to cations or anions, indifferently. The negative production term for the j-th reaction can be defined in a similar way,

$$\dot{\omega}_j^- = -eN_a K_{br,j} n_c, \tag{5.11}$$

where $K_{br,j}$ is the backward reaction rate of the j-th reaction and n_c is the number of cations or anions consumed by the reaction. The backward reaction rate depends on the fluid properties and on the concentrations of the products of the reaction. In particular, unlike the forward one, the backward reaction rate is strongly influenced by the imposition of an external electric field. For this reason, in order to take into account the real distribution of charges in the domain, assuming a first order kinetics for the charges, a linear scaling is imposed to the negative production rate, leading to the following definition of the production terms:

$$\dot{\omega}_P = \dot{\omega}_M = \sum_{j=1}^{N_r} \dot{\omega}_j^+ + \frac{\sum\limits_{j=1}^{N_r} \dot{\omega}_j^-}{(P)_{FPV}(M)_{FPV}} PM. \tag{5.12}$$

In the equation above, N_r is the number of reactions involving a production or a consumption of charges. Moreover, the summations are precomputed and stored in the chem-table, along with: the P and M quantities obtained by the solution of the steady flamelet equation and indicated with subscript "$(\cdot)_{FPV}$" (to distinguish them from the runtime values); k_P and k_M; α_P and α_M. Equation (5.12) ensures, by construction, that both scalars will have exactly the same production rate, enforcing the conservation of charge principle.

Using the described model it is possible to evaluate the local electric charge density of the fluid mixture as

$$\rho_q = \rho(P - M), \tag{5.13}$$

which can then be used in the Gauss law (Equation (2.26)). Finally, the electric force term that is considered in the momentum conservation equation (Equation (2.22)) can be easily computed as $\rho(P - M)\mathbf{E}$.

5.2 Numerical Procedure

The low-Mach-number Navier–Stokes equations together with the transport equations of the combustion model are solved by the semi-implicit fractional-step method proposed by Shunn et al. [97]. A Poisson equation for the pressure is obtained by a projection step to achieve a consistent discretization of the momentum equation. The computational domain is discretized by an unstructured grid employing a linear reconstruction of the variable inside each cell to evaluate spatial gradients. The resulting spatial discretization is second-order accurate with low numerical dissipation. As pointed out by Sommerer and Kushner [99] and more recently by Belhi et al. [5], the high drift velocity developed by the ions, even when exposed to weak electric fields, increases the stiffness of the problem requiring a time-step much smaller than that needed to advance the Navier–Stokes equations in time. In fact, the Courant–Friedrichs–Lewy (CFL) condition for the k^{th} drifting scalar is reformulated to provide the integration time-step (Δt) as

$$CFL_k = \max_{1 \leq j \leq n_{cv}} \left(\frac{\Delta t \displaystyle\sum_{i=1}^{n_{f,j}} |(\mathbf{u}_i + k_k \mathbf{E}_i) \cdot \mathbf{n}_i S_i|}{V_j} \right), \tag{5.14}$$

where: V_j is the grid cell volume; n_{cv} is the number of cell in the computational domain; $n_{f,j}$ is the number of faces for the j^{th} control volume; $\mathbf{n}_i$ is the unit normal to the i^{th} face; S_i is the i^{th} face surface area; $\mathbf{u}_i$ and $\mathbf{E}_i$ are the flow velocity and the electric field computed on the i-th face; k_k is the mobility of the k^{th} drifting scalar. Since electron mobility is orders of magnitude higher than that of other ionized species, the time-step will be always limited by the scalar that represents the negative charges. In order to optimize the computational effort needed by the numerical procedure, a nested time discretization is combined with the fractional step for advancing the drifting scalars (P and M) and the electric potential, imposing a target CFL condition for the drifting scalars. In particular, the nested time procedure consists in subdividing the time step used to integrate the flow and chemistry equations into a number of steps calculated in order to guarantee the stability of the stiff charged species transport model, namely, Equations (5.5), (5.6) and (2.16). The fluid and scalar properties needed for the solution of these equations are linearly interpolated at the solution time.

5.3 1D verification of the method

In order to verify the correct implementation of the model in our CFD solver and to provide a first validation of the present approach, we have computed the two flamelet solutions provided in Section 2.3.2 with the proposed FPV approach. Even though this may seem a trivial test case, it requires that the production rates, the diffusive fluxes as well as the drift induced by the electric field have to be well resolved in order to obtain a good agreement between the results of the FlameMaster code and of the CFD solver.

The CFD solution has been obtained using a one-dimensional grid composed of 3001 nodes evenly distributed over a total length of $40\,\mathrm{mm}$. Dirichlet conditions have been imposed at the first left point of the computational domain, enforcing the laminar planar flame speed, the mixture fraction relative to the case at $\phi = 1$ and the

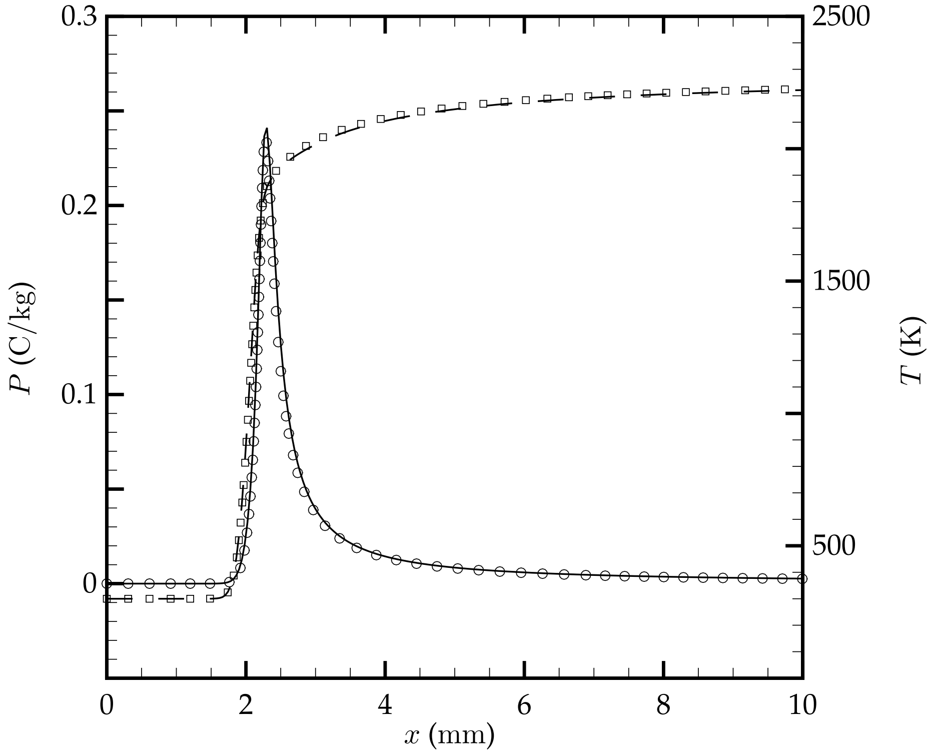

FIGURE 5.1: Comparison of the unstrained premixed flamelet solution at $\phi = 1$ obtained using the FlameMaster code and the proposed model considering mechanism "A". Symbols represent the profiles of P (○) and temperature (□), computed using the detailed chemistry. The dashed and solid lines correspond to the solutions obtained with our CFD code.

progress-variable equal to zero. The concentration of positive and negative ions has also been set to zero at this point, considering that this configuration should not produce any ion-flux. Moreover, the large distance considered between the inlet plane and the flame-front (about $1.6\,\mathrm{mm}$) ensures the suitability of this assumption. In fact, it has been verified that the profiles of positive and negative charges concentration reach zero at a large distance from the inlet (about $1.5\,\mathrm{mm}$ as shown in Figures 5.1 and 5.2), entailing that the boundary condition is not influencing their fluxes in the domain. A convective outlet condition has been imposed at the last right point of the computational domain for the velocity and all the scalars.

Figures 5.1 and 5.2 show the results obtained for the mechanism "A" and "B", respectively. In both cases, the solutions obtained by the FPV approach have been compared with those computed by the FlameMaster code. It is noteworthy that, unlike the FPV-CFD solver, the FlameMaster simulations are performed considering the fully coupled detailed chemistry but enforcing the electrical neutrality of the mixture and therefore without solving the generated electric field. There is an excellent agreement between the profiles of both temperature and positive charge density for the two simulations of each case. Only tiny differences, which can be attributed to the charge transport computed by the FPV-CFD solver, can be seen on the

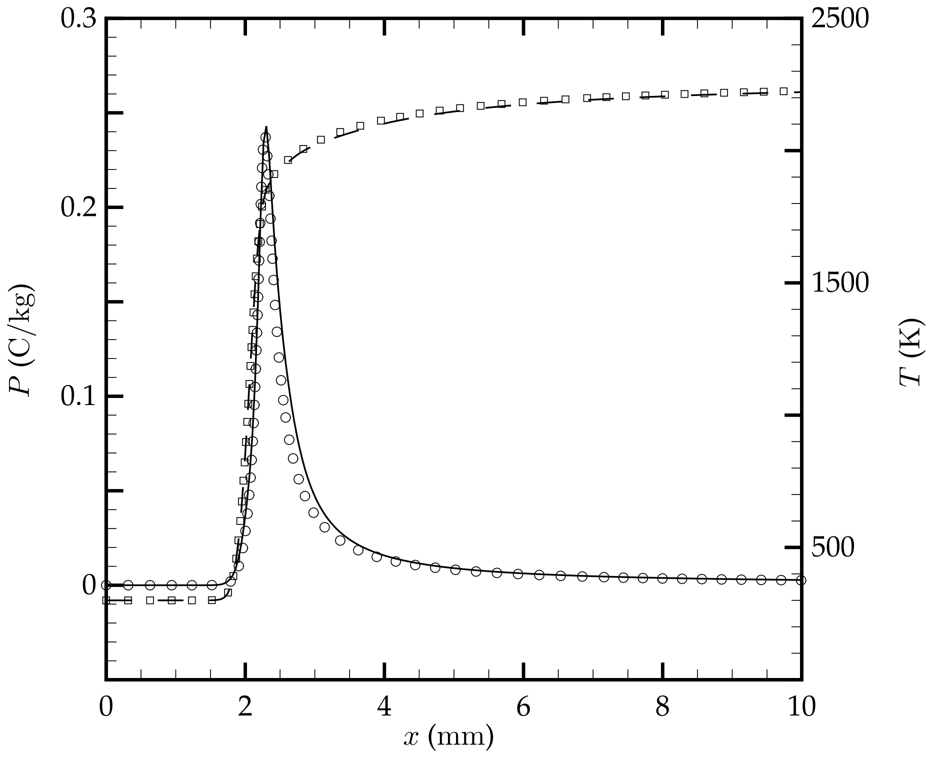

FIGURE 5.2: Comparison of the unstrained premixed flamelet solution at $\phi = 1$ obtained using the FlameMaster code and the presented model considering the mechanism "B". Symbols represent the profiles of P (○) and temperature (□), computed using the detailed chemistry. The dashed and solid lines correspond to the solutions obtained with our CFD code.

charges profile for both cases. This result was expected considering the small effect of the auto-generated electric field and constitutes a first validation of the proposed model.

5.4 Validation for burner-stabilized flame

A further one-dimensional test case has been performed to compare the results of the present reduced order model with those obtained employing a detailed description of the phenomenon in a configuration where the flame interacts with an imposed electric field. The test case has been carried out in the well-known configuration presented by Speelman et al. [100] and consists of a premixed one-dimensional flame produced by a cylindrical heat-flux stabilized burner, whose deck area is $7.069\,\mathrm{cm}^2$. A mixture of methane and air at $\phi = 1$ is injected with the laminar flame speed of the same mixture at $298\,\mathrm{K}$ and $1\,\mathrm{atm}$, whereas the temperature of the burner is kept at $350\,\mathrm{K}$. An external electric field is imposed using two electrodes, one positioned at the injection point of the mixture and the other $1\,\mathrm{cm}$ downstream.

The computations employing the detailed chemi-ionization mechanism have been performed using the code FlameMaster [87] modified in order to solve the Poisson

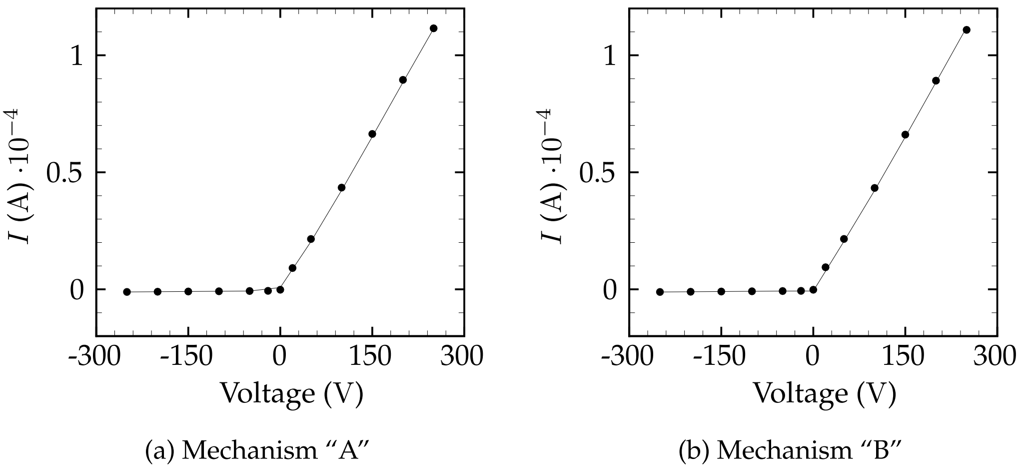

(a) Mechanism "A"

(b) Mechanism "B"

FIGURE 5.3: Results obtained for the test case of Speelman et al. [100] with the detailed model (continuous line) and reduced order model (symbols).

equation for the local electric potential and to account for the electric diffusion of the charged species. The resulting computational tool is very similar to that proposed by Speelman et al. [100] except for the numerical discretization of the differential equations and for the molecular diffusion model employed. In fact, FlameMaster [87] employs a central finite difference representation instead of the upwind finite-volume method used by Speelman et al. [100] and the diffusion model of Ern and Giovangigli [30] is substituted with that described in the Section 2.2. Since the tabulated approach, used in the present work to describe the chemistry, is not able to correctly predict heat transfer phenomena, it has been decided to perform the reduced order model simulations solving only the equations presented in the Section 5.1.2. The data needed by the equations of the charged species have been extracted by a flamelet calculation performed in by the FlameMaster code [87] imposing the electrical neutrality of the system. This procedure provides exactly the same data needed for the solution of the P and M equations as if they were interpolated from a table produced with the procedure described in Section 5.1.1 but avoids the limitations imposed by the use of a tabulated chemistry approach.

In order to keep the formulation consistent with the rest of the chapter and to reduce the computational cost of this validation, we employ the same values of the mobility described in Section 5.1.2 for both computational approaches. For this reason, the numerical results obtained will not be comparable with the experimental results of Speelman et al. [100].

Figure 5.3 shows the electric current produced by the system versus the applied voltage obtained using the detailed and reduced order model in conjunction with the mechanism "A" and "B". As expected the values of current measured with these simulations is much lower than that presented by Speelman et al. [100]. Such a mismatch is only due to the reduced mobility of the ions. Moreover, the reduced effect of the electric field on the charged species prevents the onset of the saturation on the flame. Apart from this point, the match of the two sets of data is satisfactory for both the mechanisms and particularly relevant for the performance of the model: it ensures that the reduced model is able to reproduce the results of the detailed mechanism it has been built on.

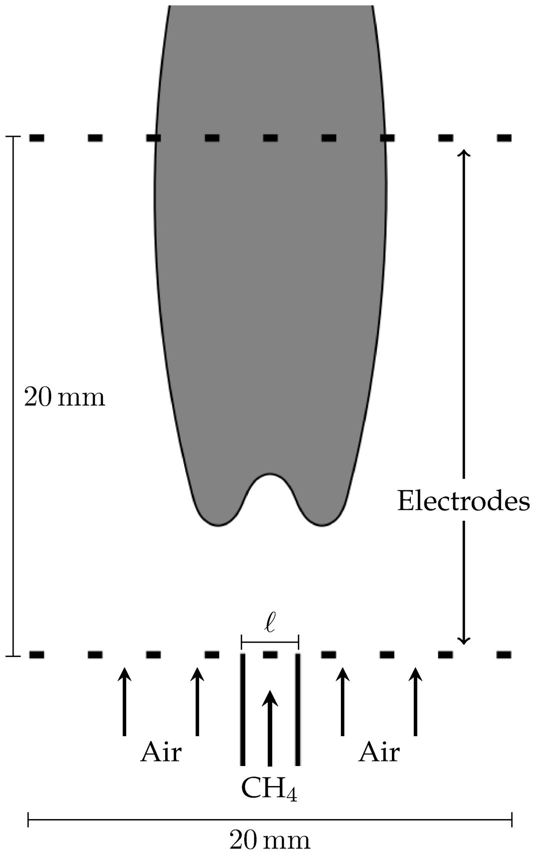

FIGURE 5.4: Sketch of the numerical test case configuration.

5.5 Two-dimensional test case

In order to test the proposed electro-chemical model in a more complex configuration, a two-dimensional configuration inspired to that of Belhi et al. [5] has been considered. It consists of a diffusive lifted methane-air flame burning in a two-dimensional slot burner whose geometry is shown in Figure 5.4. The fuel is injected in the middle of a $20\,\mathrm{mm}$ wide combustion chamber with a velocity profile corresponding to a fully developed Poiseuille flow at an average velocity of $4\,\mathrm{m/s}$. The fuel nozzle is composed of two parallel flat plates, whose thickness is $0.1\,\mathrm{mm}$, at distance of $\ell = 2\,\mathrm{mm}$, representing the reference length. At each side of the fuel nozzle, an air co-flow enters the combustion chamber with the Blasius velocity profile having a free-stream velocity equal to $0.8\,\mathrm{m/s}$ and an upstream flat plate length of $3.5\,\mathrm{mm}$. The fuel is pure methane and the oxidizer is standard dry air; both streams enter at $300\,\mathrm{K}$. The combustion process, which develops at atmospheric pressure, has a stoichiometric mixture fraction $Z_{st} = 5.4 \times 10^{-2}$ and a laminar stoichiometric flame velocity of about $u_{st}^{fl} = 0.38\,\mathrm{m/s}$. The configuration parameters are summarized in Table 5.1.

Two mesh electrodes are positioned at the inlet of the fuel and oxidizer flow and $20\,\mathrm{mm}$ downstream of the inlet, respectively, forming a sort of capacitor configuration, whose mean electric field direction is aligned with the jet velocity. The two electrodes are attached to an electrical generator in order to apply the electric field on the flame; the electric voltage is applied to the downstream electrode, whereas the inlet one is maintained at zero voltage. The fluid flow is supposed not to be

TABLE 5.1: Diffusive methane/air flame main parameters.

Parameters	Fuel flow	Oxidizer flow
Temperature (K)	300	300
Composition	$X_{\mathrm{CH}_4} = 1$	$X_{\mathrm{O}_2} = 0.21$, $X_{\mathrm{N}_2} = 0.79$
Mean/Free-stream velocity $(\mathrm{m/s})$	4	0.8
Velocity profile	Poiseuille	Blasius ($L_{up} = 3.5\,\mathrm{mm}$)
Stoichiometric flame velocity (u_{st}^{fl})		$0.38\,\mathrm{m/s}$
Stoichiometric mixture fraction (Z_{st})		5.4×10^{-2}

influenced by the presence of the electrodes.

5.6 Numerical setup

The computational domain used for all the calculations coincides with the portion of the combustion chamber located between the electrodes (Figure 5.4). This choice derives from a trade-off between the accuracy of the prediction and the number of points needed for the simulation. In fact, a longer domain would guarantee reduced influence of the outlet boundary condition on the flame, but also an increase in the number of grid points. Moreover, the chosen configuration ensures a straightforward specification of the boundary condition at the downstream electrode. The two-dimensional computational grid has been generated starting from a structured grid made of 128^2 uniformly distributed points. An homothetic refinement procedure has led to a mesh of about 2.4×10^5 quadrilateral cells clustered in the flame region. The obtained grid spacing has a minimum value of about $4 \times 10^{-2}\,\mathrm{mm}$ next to the center line of the chamber and smoothly increases going toward the sides of the domain.

Dirichlet boundary conditions have been imposed at the inlet points for the fluid velocity, mixture fraction and progress-variable. A no-slip condition has been applied to the fuel nozzle lip, whereas the sides of the domain have been considered as inviscid walls. Standard convective boundary condition for the flow velocity has been imposed at the downstream outlet points. The effect of buoyancy has been neglected.

The electrodes have been modeled by a Dirichlet boundary condition for the Gauss equation and alternatively using Neumann or Dirichlet boundary conditions for P and M. In the particular electrical configuration considered here, for the cathode (negative pole, being this a power consuming device), the Dirichlet condition is applied to the negative charges ($M = 0$), which are repelled by the surface, and the Neumann condition is applied to the positive charges ($\nabla P \cdot \mathbf{n} = 0$), which are attracted by the surface. Concerning the anode, the numerical boundary conditions are the opposite. However, since the flow outlet section intercepts the flame, the charged particles are always present in this section and the Dirichlet condition would cause numerical instabilities. For this reason, the zero normal gradient boundary condition for the charges has been imposed at the outlet points both for an anode or a cathode.

The flamelet profiles have been computed by the code FlameMaster V3.3.10 [87] using 1000 unevenly spaced grid points; the output data are organized in a chemical look-up table.

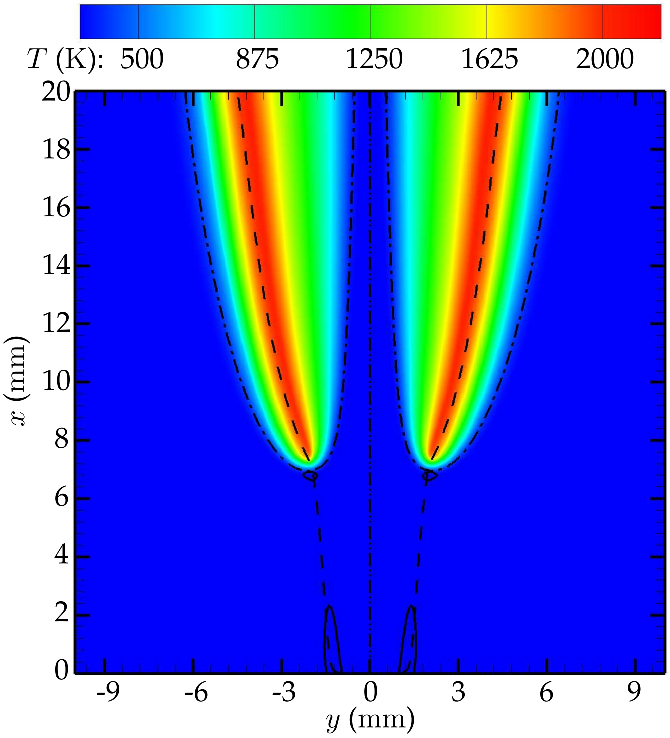

FIGURE 5.5: Comparison of temperature fields (expressed in K) in the cases without charge transport for the mechanism "A" (left) and mechanism "B" (right). The dot-dashed line is the iso-line at $C = 5 \times 10^{-3}$; the dashed line is the stoichiometric iso-line location; the continuous line is the contour at $u_x = u_{st}^{fl} = 0.38\,\mathrm{m/s}$; the dot-dot-dashed line is the symmetry axis.

5.7 Results

This section provides the analysis of the flame structure corresponding to different applied voltages, including the configuration without any imposed electric field. An important feature of the flame structure is the flame-tip position, which is here defined as the first point where C reaches the value of 5×10^{-3} on the stoichiometric mixture fraction iso-line.

In the next sub-section, the flame configuration computed without charges transport model is discussed, being taken as baseline configuration. Afterwards, the effect of an applied continuous voltage on the flame-tip position will be presented analyzing the new equilibrium configurations. In order to further study the local behavior of the flame immersed in an electric field, the analysis of the electric potential and mixture charge will be performed in the steady configuration of each value of the applied voltage.

5.7.1 Simulations without charge transport model

For both chemical mechanisms considered in this work, these simulations have been initialized using a zero velocity flow-field. A first computation has been performed to determine the steady solution for the non-reactive flow. Then, the flame has been ignited imposing the maximum physical value of the progress-variable (based on the local Z value) and a second simulation has been performed in order to reach the steady configuration.

For both mechanisms, the flame is symmetric from the ignition time to the stabilization, which is reached in about $1.5\,\mathrm{s}$. Figure 5.5 shows the temperature contours computed using mechanisms "A" (on the left-hand side) and "B" (on the right-hand side). The two mechanisms predict the same flame configuration, proving the marginal influence of the chemi-ionization mechanism on the combustion process. The baseline lift-off height measured in both cases is $x_0 = 6.97\,\mathrm{mm}$ (about $3.5\ \ell$), whereas the spanwise position of the flame tip is $y_0 = 1.90\,\mathrm{mm}$ (about $0.95\ \ell$). Both these data are in good agreement with the results of Belhi et al. [5]. The difference between the present test and that in literature is the shape of the injection velocity profile of the co-flow. The position of the flame seems remarkably influenced by this boundary condition, in fact, the flame is easily blown-off or shifted toward the fuel nozzle slightly changing the upstream length of the plate for the Blasius profile.

It is noteworthy that both solutions show the well-known reduction of the mixture velocity in the upstream region of the flame as described by many authors in the literature [29, 89, 93]. This phenomenon, together with the shape of the velocity profiles imposed at the inlet sections, determines the point of stabilization of the flame in a flow with an average velocity higher than the laminar planar flame speed.

5.7.2 Flame-tip steady position for voltage imposition

Once the steady configuration of the flame has been obtained without considering charge transport phenomena, a series of simulations has been run for both mechanisms varying the voltage applied to the flame. Two sets of twelve simulations have been performed changing the applied voltage in the range between $-750\,\mathrm{V}$ and $1250\,\mathrm{V}$. This range has been chosen considering the attachment voltages predicted by Belhi et al. [5] and the limitations posed by the employed central finite difference scheme. A step of $125\,\mathrm{V}$ has been used as sample interval for the negative polarity cases, whereas the positive polarity has been sampled by a $250\,\mathrm{V}$ interval. The smaller sample interval employed for the negative polarity has been chosen in order to capture the sharper attachment of the flame expected in this configuration.

The streamwise (x/x_0) and spanwise (y/y_0) non-dimensional coordinates of the flame-tip at steady-state are plotted in Figure 5.6 versus the applied voltage, x_0, y_0 being the streamwise and spanwise coordinates of the flame-tip for $\Delta\Phi = 0\,\mathrm{V}$. For consistency, it has been verified that the flame-tip position does not change when the charge transport model is employed and no voltage is imposed. On the other hand, as shown in the figure, both the positive and negative polarities lead to a reduction of the flame-tip lift-off height. In the unattached cases, the new equilibrium point is reached when the force due to the electric field is balanced by the higher momentum of the flow next to the injection region. Because of this mechanism, the flame will eventually attach to the upstream electrode when the flow momentum is not strong enough to counteract the electric force. In this context, it is evident the importance of the injection velocity profiles of both the co-flow and fuel jet, as well as of the nozzle lip thickness. It is noteworthy that the present model is not adequate to reproduce quasi-attached configurations because of the strong electric field generated between the flame and the electrode. The electric field intensities predicted in these configurations would definitely activate non-thermal processes and probably lead to the electrical breakdown of the mixture. Moreover, the high strain of the flow and the possible heat flux through the fuel nozzle would make the present chemical model inadequate to describe the combustion process in these configurations.

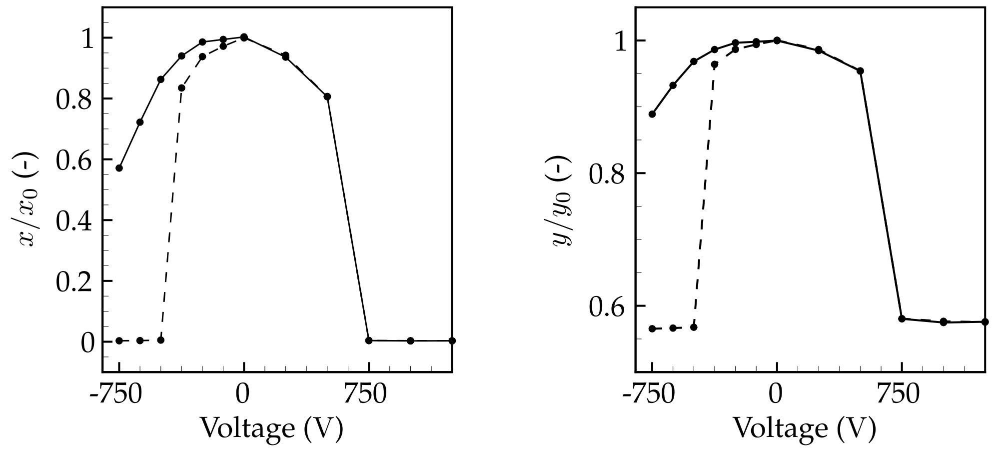

(a) Streamwise position

(b) Spanwise position

FIGURE 5.6: Flame-tip steady position in the streamwise and spanwise directions expressed as fraction of the reference position for mechanism "A" (—●—) and mechanism "B" (- ● -).

Figure 5.6a shows that both the chemical set of reactions predict the attachment of the flame to the upstream electrode at $\Delta\Phi = 750\,\mathrm{V}$ for the positive polarity. In particular, the right-hand sides of the two graphs are almost identical because the two considered chemical mechanisms produce a similar quantity of positive ions with the same transport properties, exchanging the same momentum with the incoming flow. The branches of the graph related to the negative polarities (left-hand side of the graphs) show a completely different behavior for each mechanism. In fact, the flames computed with the mechanism "A" are less responsive to the applied voltage, if compared with the positive polarity cases, and do not achieve the attachment to the upstream electrode in the considered voltage range. On the other hand, mechanism "B" provides flames which are continuously closer to the upstream electrode and predicts an attachment of the flame-tip between $\Delta\Phi = -375\,\mathrm{V}$ and $\Delta\Phi = -500\,\mathrm{V}$. Such a difference, commonly called "diodic effect", has been already observed in the literature [117]. The difference in the shape of the plotted graphs is due to the different nature of the ions produced by the two mechanisms. The presence of the anions in the upstream part of the flame, predicted by mechanism "B" as shown in Figure 2.2, is responsible for the stronger attraction of the flame by the upstream electrode in the cases with negative polarity. Firstly, the heavy anions are more effective than the electrons in reducing the flow momentum, thanks to their lower mobility [43]. Then, the formation of anions inhibits the recombination of the electrons with the cations through the mechanism described in Section 2.3.2, generating a larger region of negatively charged mixture, as described by Belhi et al. [5]. On the other hand, mechanism "A" produces only electrons, which are lighter than the cations and, therefore, less effective in reducing the momentum of the incoming flow.

Figure 5.6b shows the spanwise non-dimensional coordinate of the flame-tip for all the tested configurations. The behavior of both mechanisms is very similar to that of the streamwise position plots, except that it appears to be less affected by the applied voltage. The cause of this difference is that the applied electric field is mainly aligned with the flow direction with only minor deviations close to the flame-tip due to the flame curvature. The displacement toward the center of the flame-tip is, therefore, due to the shape of the stoichiometric mixture fraction iso-line shown in Figure 5.5.

The results shown here are in good agreement with the findings of Belhi et al. [5], considering the high sensitivity of this kind of system to the modeling assumptions and numerical setup. Regarding the positive polarity, the available calculations [5] show an attachment of the flame at 1250 V. This value is rather higher than those found in the present results, but this difference is probably due to a different injection profile of the co-flow. Furthermore, analyzing the negative polarity branches of the graph, it is possible to find a substantial agreement of the flame position computed using both the considered chemical mechanisms. In fact, the sharp attachment achieved with the mechanism "B" and the high distance of the flame from the nozzle predicted with the mechanism "A" reduce the influence of the inlet injection profile uncertainty on the flame position. Although the very good agreement obtained in the validation in Section 5.4 suggests that the assumptions made for evaluating the transport properties and reaction terms of the drifting scalars are appropriate, another source of discrepancy between the present results and those of Belhi et al. [5] can still be in the use of Equations (5.7), (5.8) and (5.12) when the model is employed for more complex configurations. Unfortunately, the impossibility of isolating these two sources of error and the lack of experimental data on this case make further analyses unfeasible at the present time.

5.7.3 Electric potential distribution

As expected and described in the previous section, the introduction of the electrical model does not have any influence on the flame configuration when no electric voltage is imposed, but this case is interesting because of the ability of the present model to reproduce the electric field generated by the flame. In fact, the large difference in diffusivity between the heavy charged particles and the electrons, which are produced in the reaction region of the flame, leads to a charge unbalance reducing the number of anions in this zone. This mixture polarization generates an electric field pointing away from the flame and inducing a drift velocity of the electrons which counteracts their diffusive flux. The electric potential field is shown in Figure 5.7 for the region surrounding the flame. This generated electric field is too weak to influence the fluid dynamics producing a negligible force, and, for this reason, it is usually neglected in combustion simulations. On the other hand, this phenomenon is widely used in various types of combustion chambers in order to monitor the behavior of the flame with ion-sensors.

Mechanism "B" predicts a slightly lower electric potential difference, whose magnitude is 0.6 V, and it is concentrated in the reacting region. On the other hand, the high potential region computed with mechanism "A" is larger and more intense (the total difference of potential is about 1.2 V). Both predicted values are in good agreement with the measurements available in literature obtained by ion-sensors [1, 68, 75].

The contour plots provided in Figure 5.8 show the distribution of electric potential in the entire computational domain for two values of applied voltage with opposite polarity, 500 V and -375 V, for both chemical mechanisms. In both graphs, the flame creates a region with constant electric potential between the flame-front and the downstream electrode, highlighting the importance of modeling the interaction of the flame with the electric field. The extension of this region is determined by

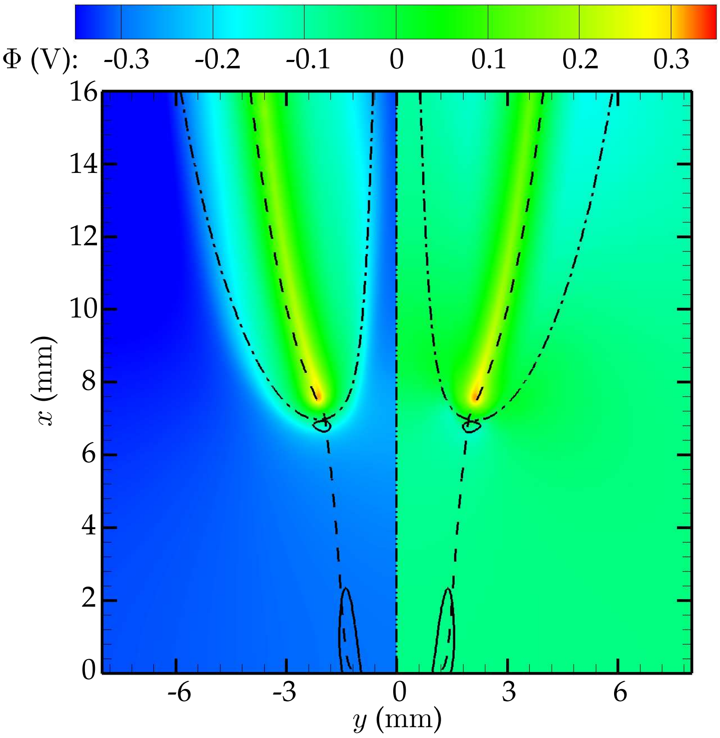

FIGURE 5.7: Comparison of electric potential field (expressed in V) in the cases at $\Delta\Phi = 0\,\mathrm{V}$ for the mechanism "A" (left) and mechanism "B" (right). The iso-lines are defined as in Figure 5.5.

the ability of the flame to produce a large amount of charges in its reacting layer. In fact, in a steady condition, the charges are usually depleted at a rate close to the production rate and the difference between the two rates is equal to the advective and diffusive fluxes. When the electric field induces a displacement on the charges distribution, they move in opposite direction locally reducing their consumption rate. The equilibrium point is reached either when the charge separation is sufficient to absorb the imposed voltage or when the maximum amount of charges is produced by the flame. In both the presented cases, the steady configuration is obtained through the first configuration, being the flame sub-saturated. The electric potential distribution, shown in the contour plot, entails that the electric field intensity is higher in the region between the flame-tip and the upstream electrode and highlights the need of considering the mixture charge in the Gauss equation (Equation (2.16)). Moreover, this modification of the electric potential field by the flame strongly affects the convective movement of the charges. In fact, their distribution is marginally affected in the diffusive region of the flame and, instead, strongly modified in the premixed part of the triple flame.

Figure 5.9 shows a plot of the value of the electric potential measured at the flame-tip position versus the applied voltage for mechanisms "A" and "B". The plotted line is almost coincident with the bisector for all the lifted flame configurations of both polarities. The line sharply deviates from the bisector when the flame attaches to the upstream electrode and the kinetics of the ions becomes more complex and not suitable to be predicted by the present model. The largest difference between the flame-tip voltage and the imposed one for an unattached flame is in the region between $-500\,\mathrm{V}$ and $-750\,\mathrm{V}$ for mechanism "A". The smooth but consistent

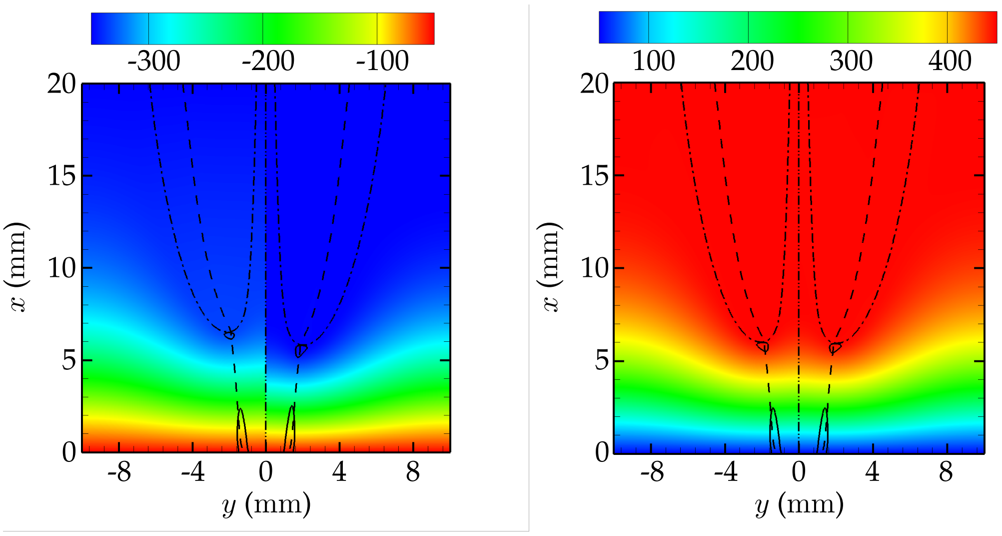

(a) $\Delta\Phi = -375\,\mathrm{V}$ (b) $\Delta\Phi = 500\,\mathrm{V}$

FIGURE 5.8: Electric potential contour plots (expressed in V) in the flame-front region at two different imposed voltage difference. Results for mechanism "A" are on the left and for mechanism "B" on the right of each picture. The iso-lines are defined as in Figure 5.5.

deviation from the bisector suggests an incipient electrical saturation of the flame.

Figure 5.9 also explains why the streamwise and spanwise position of the flame-tip exhibit a parabolic scaling for both simulation set (see Figures 5.6a and 5.6b). This result is in good agreement with the results present in literature. This non-linearity is due to the increasing polarization of the flame, which experiences a larger charge separation in order to absorb the rising difference of potential, as shown in Figure 5.9. In fact, the larger charges separation over the flame-front region, in conjunction with the increased difference of potential, leads to the mentioned quadratic scaling of the equilibrium point position between the flow momentum and the electric force.

5.7.4 Charge repartition and local electric field

Figure 5.10 shows the charge distribution in the surroundings of the flame tip at both $-375\,\mathrm{V}$ and $500\,\mathrm{V}$. The four combinations of mechanisms and polarities predict two charge concentration regions, one next to the C iso-line and the other located further downstream in the reaction layer. The first charge peak is due to modification of the ionized species distribution caused by the presence of the electric field. In fact, the sign of this peak is a direct consequence of the applied field polarity, being positive in the positive polarity case and negative in the other. The second peak of charge, which is positive in all the four cases examined here, coincides with the region of the flame where the charges are produced and it is due to the high diffusivity of the electrons. In fact, such a charge peak is responsible for the electric field generated by the flame and described in the previous sub-sections (Figure 5.7). Its effect on the electric potential field is not visible in the contour plots relative to the present cases (Figure 5.8), being the magnitude of the generated potential much weaker than the applied voltage.

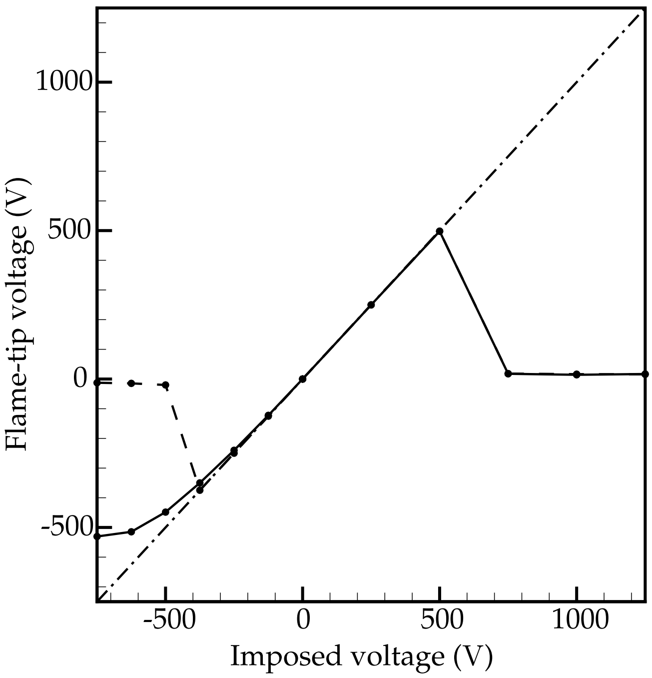

Figure 5.9: Flame-tip electric potential for mechanism "A" (—●—) and mechanism "B" (- ● -). The bisector is plotted as (-·-·-).

In the positive polarity case, both the fields of the Figure 5.8b show similar charged areas along the C iso-line, but the calculations performed with the mechanisms "A" are characterized by a higher and more elongated peak. On the other hand, the solution obtained with the mechanisms "B" has two additional small charge concentration regions, located between the C iso-line and the reacting region. These differences between the two mechanisms are ascribable to the higher charges mobility of the mechanism "A", which contains only electrons as negatively charged species. The higher negative mobility induces a higher mixture polarization localized in the upstream part of the flame-front. Regarding mechanism "B", the presence of heavy ions in the mixture, which modify the local transport properties of the scalar M, entails more complicated equilibrium points for the distribution of the electrical quantities.

In the negative polarity case (Figure 5.8a), mechanism "B" predicts a higher peak due to the electric field induced charges transport. The diametrical behavior of the two mechanisms with respect to the positive polarity is due to the already described effect of the heavy anions (present in the upstream part of the flame) that inhibit the recombination of the electrons and therefore cause an anion concentration. The shape of this concentration and its location are in good agreement with the contour plots shown by Belhi et al. [5] in his Figure 11. This phenomenon is responsible for the stronger influence of the imposed electric field on the flame position for this type of polarity.

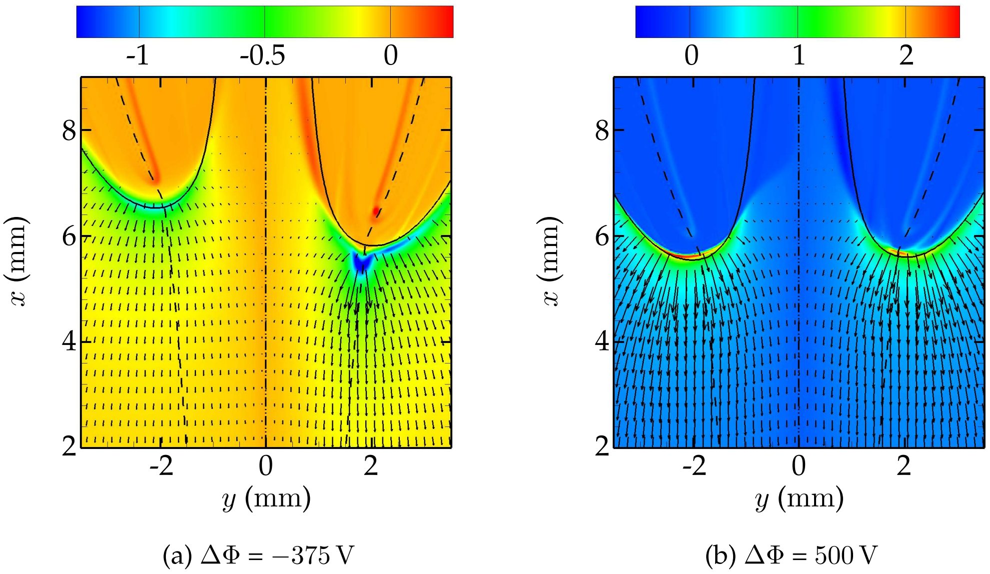

(a) $\Delta\Phi = -375\,\mathrm{V}$ (b) $\Delta\Phi = 500\,\mathrm{V}$

FIGURE 5.10: Electric charge density contour plots (expressed in $\mathrm{mC/m^3}$) for two imposed voltage difference. The vectors represent the electric force exchanged with the fluid mixture. Results for mechanism "A" are on the left panel and for mechanism "B" on the right panel. The iso-lines are defined as in Figure 5.5.

5.8 Computational cost of the simulations

Formulating an effective model, besides its accuracy one has to put particular attention in enhancing its efficiency and its affordability. In fact, the reduction of the computational cost of this kind of simulations is a mandatory requirement for analyzing complex flows in the future. For this reason, a comparison of the average wall-time needed per time-step has been carried-out for each simulation done in this work. When mechanism "A" is used, the computational cost of the present approach is comparable with the performance of the model proposed by Belhi et al. [4]. Mechanism "B" instead provides a completely different behavior of the model because of the introduction of the averaged properties of the scalars.

All the simulations were run on two Xeon 10-core E5-2660v3 (2.6 GHz) processors without hyper-threading arranged on a single node. The time-step for the inner iterations has been evaluated using the CFL number based on the advection of the negative charges (CFL_M), which has been set to 3.5 for all the simulations. The outer advancement step has been kept constant and equal to $5 \times 10^{-6}\,\mathrm{s}$ for all the simulations (corresponding to a CFL number of about 2.5 based on the flow velocity). The results of the comparison are reported in Table 5.2 for each combination of applied voltage and kinetic mechanisms.

Analyzing the data in Table 5.2, it is clear the large speedup obtained employing the present model in conjunction with mechanism "B". The best cases (where the speedup is close to 40) are those where an external voltage is applied and where the flame is not collapsed on the upstream electrode. Such a large difference is due to the reduction of the advection velocity of the scalar M in the regions far from the flame. This reduction of drift velocity is entailed by the averaging process on the scalar mobility.

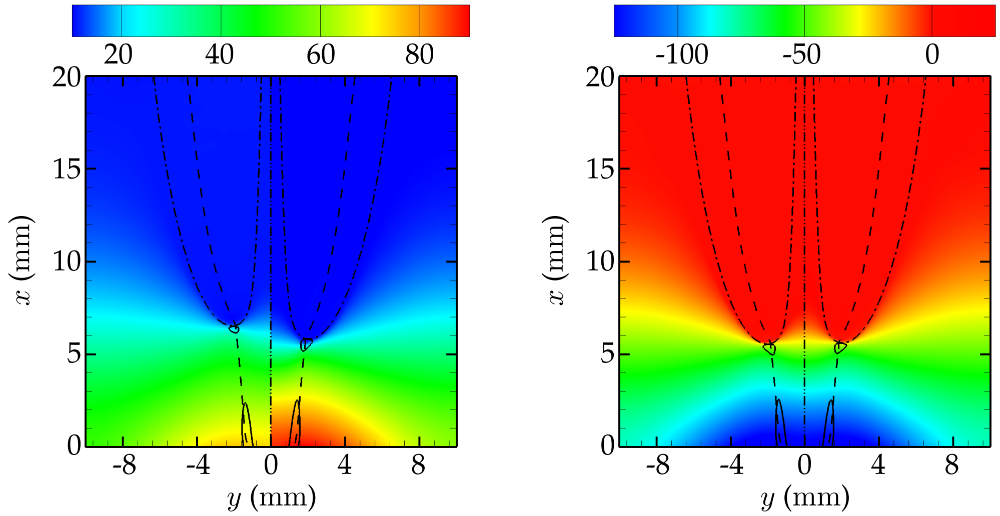

(a) $\Delta\Phi = -375$ V x direction

(b) $\Delta\Phi = 500$ V x direction

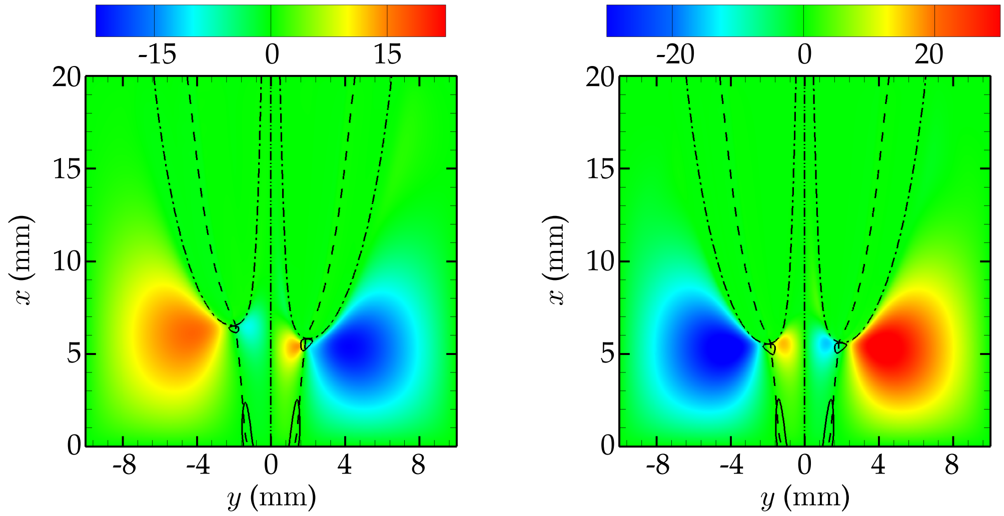

(c) $\Delta\Phi = -375$ V y direction

(d) $\Delta\Phi = 500$ V y direction

FIGURE 5.11: Electric field intensity projected along the x (a-b figures) and y (c-d figures) directions (expressed in $\mathrm{kV/m}$) at two different imposed voltage. Results for mechanism "A" and for mechanism "B" are shown on the left and right hand-side of each picture, respectively. The iso-lines are defined as in Figure 5.5.

For this reason, the time per step measured in the case without any applied voltage is almost identical for the two mechanisms. In this case, the region where the electric field reaches its higher intensity coincides with the flame, where the mobilities of P and M are computed using the species distributions obtained by the flamelet equations. Being the distribution predicted by the flamelets very similar to those predicted by the CFD simulation, the drift velocity computed for the scalar M does not change with the ionization mechanism. As consequence, the number of inner time-steps needed by both mechanisms is almost the same (about 5).

On the other hand, when an external voltage is applied, the maximum electric

TABLE 5.2: Computational cost of the simulations with FPV model per flow time-step.

Voltage (V)	**Mech. "A"** (s)	**Mech. "B"** (s)	**Speedup**
-750	111.26	17.12	6.50
-625	93.15	14.91	6.25
-500	71.86	7.69	9.34
-375	55.90	1.36	41.16
-250	39.72	1.36	29.08
-125	26.96	0.95	28.25
0	5.29	5.26	1.01
250	37.16	1.33	28.01
500	79.90	1.79	44.61
750	123.75	15.25	8.11
1000	177.23	22.67	7.82
1250	256.91	32.67	7.86

field intensity is going to be placed next to the upstream electrode, as shown in Figure 5.11, where no charges are present especially in the weak voltage cases. In this region, mechanism "A" computes the drift velocity of the scalar M using the mobility of the electrons. On the other hand, mechanism "B" uses an arithmetically averaged mobility which is two orders of magnitude lower than the electron mobility. In the second case, the drift velocity computed for the anions is much lower and, therefore, the set-up employing mechanism "A" experience a most restrictive time advancement condition. Accordingly, the solver is forced to perform a larger number of inner time-steps (for a $\Delta\Phi = 500\,\mathrm{V}$ the simulations with the mechanism "A" and "B" require about 200 and 5 inner time-steps, respectively). Since the number of operations performed per inner time-steps is the same regardless the complexity of the chemistry model, a large variation of wall-time needed for the solution is registered.

The speedup effect of mechanism "B" vanishes in the cases with attached flame because the reacting region reaches the zone of the computational domain where the electric field is maximum and therefore the computed velocity of the anions becomes again comparable between the two mechanisms.

Such a reduction of the numerical cost is not a mere numerical artifact produced by the present model, but it relies on the fact that the electrons, produced in the flame region, are very likely to collide with molecular oxygen present in the mixture upstream the flame, producing $O_2{}^-$. This phenomenon, which tracking each species does not make any impact on the stiffness of the problem, strongly enhances the numerical efficiency of the system in this configuration where the maximum electric field is reached well outside the reacting region (see Figure 5.11).

Chapter 6

Conclusions

The use of electric fields has experimentally demonstrated to be a very effective way of controlling reacting flows. The understanding of the physical phenomena involved in this interaction is still an open research problem, which has been recently undertaken both numerically and experimentally. In particular, the results of the present thesis are oriented to a better understanding the aspects of modeling of the impingement of an electric field on non-premixed flames and are organized in three main parts.

A detailed description of the aero-thermo-chemical fields produced by diffusion flames interacting with an electric field is provided in the first part of this thesis results (see Chapter 3). Axisymmetric numerical simulations of methane-air counterflow laminar diffusion flames impinged by sub-breakdown DC electric fields are performed using multi-component transport and a detailed chemical mechanism that includes elementary steps for the conversion of six electrically charged species. An axial electric field is induced by two electrodes located on the oxidizer and fuel sides and arranged parallel to the mixing layer. The configuration matches the geometry and flow parameters of the burner recently studied experimentally by Park et al. [78]. Steady-state solutions are obtained by integrating the conservation equations using a pseudo-time stepping method. The overall effect of the incident electric field is to induce a bi-directional ionic wind that interacts with the two incoming streams of neutral gases, in such a way that the local strain rate is decreased. This generates a faster-burning flame and, consequently, a smaller concentration of charged species. Byproducts of this phenomenon are a slight increase in the flame temperature, a decrease in the stoichiometric scalar dissipation rate, a displacement of the stagnation plane, a non-monotonic trend of the intensity with respect to the applied voltage, and a strong distortion in the spatial distribution of charged species. In the present arrangement of the electrodes, where the upper one is the anode and the bottom one is the cathode, the ionic wind is primarily formed by H_3O^+, flowing to the oxidizer side, and ${O_2}^-$, flowing to the fuel side. The transfer of momentum between the ionic wind and the neutral gases occurs primarily outside the mixing layer in the fuel and oxidizer streams. In contrast, the hot gas within the diffusion flame tends to be one moving under quieter conditions of quasi-electroneutrality and negligibly small electric force. Fuel dilution tends to dampen these effects by centering the diffusion flame in the burner, which leads to an increased cancellation of the electric forces induced by the ionic winds. At small voltages, the diffusion flame behaves as a quasi-perfect conductor whose interior is shielded by electric charges produced in abundance, while high voltages enhance dispersion of charges and lead to saturation of the electric current. An intermediate regime, where an overcurrent occurs, is found that results from the competition between electric drift, charge production, and molecular diffusion of reactants. The results presented in this study are in qualitative agreement with the experimental observations made by Park et al.

[78]. Nonetheless, quantitative disagreements are obtained in the saturation current, which is larger in the simulations, and in the intensity of the flow modifications enabled by the incident electric field, which are more pronounced in the experiments. The former issue calls for necessary improvements in the chemical-kinetic description of the problem, while the latter involves experimental uncertainties related to hydrodynamic effects caused by the perforated plates and to the fundamental question of whether the PIV tracers follow the flow pathlines in the presence of incident electric fields. In the present work, additional calculations of simulant PIV particles carrying a small amount of electric charge show improved agreement with experimentally observed flow patterns. The functional form of the scalar dissipation rate is found to depend on the applied electric field. This suggests that a closure model for the scalar dissipation rate, to be used in notional flamelet models incorporating these effects, should in principle be augmented to account for the resolved value of the electric field.

The Chapter 4 of the thesis deals with the problem of developing a tool able to provide a complete description of the mixture thermo-chemical properties in a diffusive flame impinged by an electric field, using a lower amount of computational resources compared to the computations presented in Chapter 3. This objective is accomplished, in this work, applying the well-known transformation of the governing equations form the physical space formulation to the mixture fraction space. In this way, the phenomena described in two dimensions in Chapter 3 are projected on a one-dimensional space which is perpendicular to the stoichiometric surface of the flame with the intrinsic computational benefits related to the reduction of the dimensionality of the problem. Moreover, the coordinate system defined based on the mixture fraction is, by construction, stretched in the mixing layer of the flow and, therefore, is particularly efficient in describing the reacting layer of the flame. On the other hand, this approach is not capable of describing the variation of the electric field that happens outside the mixing layer, where the mixture fraction mapping becomes singular. This electrified flamelet approach has been validated on the counterflow flame experimentally studied by Park et al. [78] using the data extracted from the detailed simulations of Chapter 3. The comparison of the two sets of data showed that this reduced order model is capable of accurately recover the results of the detailed model for the electric potential distribution and for both the neutral and ionized species as well. Some marginal errors are present in the charged species profiles where the presence of the singularities in the electric potential profiles leads to numerical errors in the estimation of the ionized species fluxes in these regions. Thanks to the low computational cost of the model, it has also been possible to perform a preliminary exploration of the steady electrified flamelet space constructing the entire s-curves for three different applied electric field. This tool can be particularly useful in the formulation of sub-grid-scale models for turbulent and laminar combustion that consider the effect of the electric field on the reacting layer of the flame.

The last part of the thesis proposed a formulation of a Flamelet Progress-Variable (FPV) model that includes the effects of the impingement of the electric field on the charged species produced by the flame and that can be applied to an arbitrary geometry. The proposed formulation solves the same number of governing equations independently of the chemical mechanism used to predict the chemi-ionization of the flame. This model, consistently with the FPV approach, only introduces two scalar quantities, which are used to predict the local presence of positive and negative charges in the mixture. Therefore, the proposed approach allows one to use detailed and more accurate chemistry models, improving the accuracy of the numerical simulations without any increase of computational cost. The model has been tested using two numerical test cases and employing two different chemical mechanisms for the ionization of the mixture. Two one-dimensional test case has been first considered in order to validate the accuracy of the proposed reduced-order model to reproduce the results of a detailed chemi-ionization model. Then, the results of two-dimensional simulations, performed with a wide range of constant imposed voltage, have shown a good agreement with the calculations available in the literature regarding the flame position and its electrical response. It has also been shown that it is possible to reduce the computational cost of each simulation by a factor of 40. This aspect, together with the low dimensionality of the chem-tables required by the model, can be very useful for the extension of the present formulation to turbulent flows. The two scalar quantities defined to describe the behavior of the positive and negative charges, which are the key feature of the proposed FPV approach, on one hand render its use very efficient and, on the other hand, introduce some approximations in modeling the charge transport phenomena. This aspect should be definitely investigated in the future, taking advantage of experimental test case specifically produced for model validation. Moreover, the behavior of the present formulation with more complex species transport models and configuration is a current field of investigation.

6.1 Suggestion for future works

As pointed out multiple times in the text of this thesis, a large number possible investigations have been deferred to future works. Some of the most important open problems encountered in this thesis are listed below.

- *Sensitivity to the transport properties:* this study employs a simplified approach for the evaluation of the transport properties of the charged species. For instance, the value of the electron mobility has been considered constant independently of mixture thermo-chemical condition. Moreover, phenomena such as the polarization of the molecules have been neglected in the interaction of heavy charged molecules with the other components of the mixture. More accurate approaches are present in the literature and their influence on the results presented in this work still needs to be assessed.

- *Sensitivity to the chemical mechanism:* the mismatches in the ion current profiles encountered during the comparison of the numerical results with experimental data provided in Chapter 3 have been ascribed to shortcomings related to the chemical kinetic mechanisms employed for the prediction of the reactions among neutral and charged species. The limitation posed by the scaling of computational cost with the number of unknowns of the problem has led to the impossibility of determining the real impact of the assumptions made on the chemistry on the entire system. The development of more advanced numerical methods, for instance parallel matrix-free Newton-based solvers, may allow the researchers to increase the detail of the employed chemical mechanism.

- *Time accurate simulations:* the determination of transient behavior of flame impinged by an electric field is a mandatory requirement in order to have predictive capabilities on the ability of this technology to suppress combustion instability. Because of the computational cost of the simulations, this is a completely unexplored regime of this kind of flame. If, as suggested in the previous point, a coupled fully implicit Newton-based method is employed to advance the governing equations of the phenomenon, depending on the computational efficiency of the method, it might be possible to perform a time accurate integration of the system. In case such an algorithm will be developed, one of the first problems to be undertaken should be the study of the combustion instability observed by Park et al. [78].

- *Electrified flame front inside homogeneous isotropic turbulence:* all the numerical analysis present in the literature deal with the computation of laminar flames. Because of the difficulties of extracting this kind of data in an experimental context, it is still unknown how the wrinkling imposed by the turbulence on the flame front interacts with the imposed electric field. Moreover, it would also be interesting to determine how the local electric forces produced inside the domain change the properties of the surrounding flow field. In order to perform these analyses, a direct numerical simulation of a flame front wrinkled by a homogeneous isotropic turbulent field inside a capacitor should be investigated. In this context, the reduction of the characteristic time scales related to the fluid dynamics in such a flow may facilitate the computational procedure with respect to the laminar flows studied so far.

- *Electrified FPV model:* the FPV model proposed in the present work avoids the complexity of introducing the effect of the electric field as an additional independent variable of the functional manifold used during the CFD simulations, assuming that the chemistry of the combustion process is not affected by the impinging electric field and using averaging procedure to compute the local transport properties and reaction rates of the charged species. Even though the assumption made regarding the overall combustion process seems to be adequate (see Section 4.3), the introduction of an additional dimension in the functional manifold could improve the estimation of the quantities related to the charged species distributions, which are, instead, strongly affected by the applied difference of potential, and extend the application of the proposed model to more intense electric fields. This context is one of the possible applications of the electrified flamelet model proposed in Chapter 4.

- *Turbulent flame modeling:* in order to extend to use of this technology to real-world industrial applications, it is necessary to include the effects of turbulence in the proposed FPV model. In a large eddy simulation context, a very well established approach is based on accounting for the effects of the sub-grid-scales fluctuations of the resolved quantities using a presumed shape probability density function approach. This procedure is usually applied to model the residual turbulent diffusion fluxes of the mixture fraction and of the progress-variable, which have been filtered during the large eddy governing equation derivation. A similar procedure should also be applied to the electric quantities, such as the electric field and the local charge density. At this purpose, the shapes of the probability density function for these quantities in a turbulent flow are completely unknown.

Bibliography

[1] Aithal, S. M. “Prediction of Voltage Signature in a Homogeneous Charge Compression Ignition (HCCI) Engine Fueled with Propane and Acetylene”. In: *Combustion Science and Technology* 185.8 (Aug. 2013), pp. 1184–1201. DOI: `10.1080/00102202.2013.781593`.

[2] Alquaity, A. B. S. et al. “New insights into methane oxygen ion chemistry”. In: *Proceedings of the Combustion Institute* (2016), pp. 1–23. DOI: `10.1016/j.proci.2016.05.053`.

[3] Altendorfner, F., Beyrau, F., Leipertz, A., Hammer, T., Most, D., Lins, G. and Branston, D. W. “Technical Feasibility of Electric Field Control for Turbulent Premixed Flames”. In: *Chemical Engineering & Technology* 33.4 (Mar. 2010), pp. 647–653. DOI: `10.1002/ceat.200900625`.

[4] Belhi, M., Domingo, P. and Vervisch, P. “Direct numerical simulation of the effect of an electric field on flame stability”. In: *Combustion and Flame* 157.12 (2010), pp. 2286–2297. DOI: `10.1016/j.combustflame.2010.07.007`.

[5] Belhi, M., Domingo, P. and Vervisch, P. “Modelling of the effect of DC and AC electric fields on the stability of a lifted diffusion methane/air flame”. In: *Combustion Theory and Modelling* 17.4 (2013), pp. 749–787. DOI: `10.1080/13647830.2013.802415`.

[6] Bilger, R. W. “The Structure of Diffusion Flames”. In: *Combustion Science and Technology* 13.1-6 (July 1976), pp. 155–170. DOI: `10.1080/00102207608946733`.

[7] Bird, R. B., Stewart, W. E. and Lightfoot, E. N. *Transport phenomena*. New York: John Wiley & Sons, Inc., June 1960, p. 780. DOI: `10.1002/aic.690070245`.

[8] Bisetti, F. and El Morsli, M. “Calculation and analysis of the mobility and diffusion coefficient of thermal electrons in methane/air premixed flames”. In: *Combustion and Flame* 159.12 (2012), pp. 3518–3521. DOI: `10.1016/j.combustflame.2012.08.002`.

[9] Bisetti, F. and El Morsli, M. “Kinetic parameters, collision rates, energy exchanges and transport coefficients of non-thermal electrons in premixed flames at sub-breakdown electric field strengths”. In: *Combustion Theory and Modelling* 18.1 (2014), pp. 1–37. DOI: `10.1080/13647830.2013.872300`.

[10] Bohme, D. K., Goodings, J. M. and Ng, C.-W. “In situ chemical ionization as a probe for neutral constituents upstream in a methane-oxygen flame”. In: *International Journal of Mass Spectrometry and Ion Physics* 24.3 (July 1977), pp. 335–354. DOI: `10.1016/0020-7381(77)80040-5`.

[11] Bone, W. A., Fraser, R. P. and Wheeler, W. H. “Further Experiments upon Flame Propagation through Dry Carbonic Oxide-Oxygen Mixtures in an Electric Field”. In: *Proceedings of the Royal Society A: Mathematical, Physical and Engineering Sciences* 132.819 (1931), pp. 1–10. DOI: `10.1098/rspa.1931.0083`.

[12] Brown, R. C. and Eraslan, A. N. "Simulation of ionic structure in lean and close-to-stoichiometric acetylene flames". In: *Combustion and Flame* 73.1 (1988), pp. 1–21. DOI: `10.1016/0010-2180(88)90050-8`.

[13] Burcat, A. and Ruscic, B. *Third Millennium Ideal Gas and Condensed Phase Thermochemical Database for Combustion with updates from Active Thermochemical Tables*. 2005. URL: `http://garfield.chem.elte.hu/Burcat/burcat.html`.

[14] Burke, S. P. and Schumann, T. E. W. "Diffusion Flames". In: *Industrial & Engineering Chemistry* 20.10 (Oct. 1928), pp. 998–1004. DOI: `10.1021/ie50226a005`.

[15] Capitelli, M., Ferreira, C. M., Gordiets, B. F. and Osipov, A. I. *Plasma Kinetics in Atmospheric Gases*. Springer Berlin Heidelberg, 2000, p. 316.

[16] Capitelli, M. et al. "Thermodynamics, transport and kinetics of equilibrium and non-equilibrium plasmas: A state-to-state approach". In: *Plasma Chemistry and Plasma Processing* 32.3 (2012), pp. 427–450. DOI: `10.1007/s11090-011-9339-7`.

[17] Capriati, G., Colonna, G., Gorse, C. and Capitelli, M. "A parametric study of electron energy distribution functions and rate and transport coefficients in nonequilibrium helium plasmas". In: *Plasma Chemistry and Plasma Processing* 12.3 (1992), pp. 237–260. DOI: `10.1007/BF01447024`.

[18] Castela, M., Fiorina, B., Coussement, A., Gicquel, O., Darabiha, N. and Laux, C. O. "Modelling the impact of non-equilibrium discharges on reactive mixtures for simulations of plasma-assisted ignition in turbulent flows". In: *Combustion and Flame* 166 (2016), pp. 133–147. DOI: `10.1016/j.combustflame.2016.01.009`.

[19] Cessou, A., Varea, E., Criner, K., Godard, G. and Vervisch, P. "Simultaneous measurements of OH, mixture fraction and velocity fields to investigate flame stabilization enhancement by electric field". In: *Experiments in Fluids* 52 (2012), pp. 905–917. DOI: `10.1007/s00348-011-1164-5`.

[20] Coffee, T. P. and Heimerl, J. M. "Transport algorithms for premixed, laminar steady-state flames". In: *Combustion and Flame* 43.C (1981), pp. 273–289. DOI: `10.1016/0010-2180(81)90027-4`.

[21] Colonna, G., Gorse, C., Capitelli, M., Winkler, R. and Wilhelm, J. "The influence of electron-electron collisions on electron energy distribution functions in N2 post discharge". In: *Chemical Physics Letters* 213.1-2 (1993), pp. 5–9. DOI: `10.1016/0009-2614(93)85410-P`.

[22] Curtiss, C. F. and Hirschfelder, J. O. "Transport Properties of Multicomponent Gas Mixtures". In: *The Journal of Chemical Physics* 17.6 (June 1949), pp. 550–555. DOI: `10.1063/1.1747319`.

[23] Dautov, N. G. and Starik, A. M. "On the problem of choosing a kinetic scheme for the homogeneous reaction of methane with air". In: *Kinetics and catalysis* 38.2 (1997), pp. 207–230.

[24] Dayal, S. K. and Pandya, T. P. "Optical study of counterflow diffusion flames in transverse electric fields". In: *Combustion and Flame* 116 (1972), pp. 113–116. DOI: `10.1016/S0010-2180(72)80091-9`.

[25] Dayal, S. K. and Pandya, T. P. "Structure of counterflow diffusion flame in transverse electric fields". In: *Combustion and Flame* 35.C (1979), pp. 277–287. DOI: `10.1016/0010-2180(79)90033-6`.

[26] Delcroix, J.-L. and Bers, A. *Physique del Plasmas, Vol. 2*. EDP Sciences, 1994.

[27] Desjardins, O., Blanquart, G., Balarac, G. and Pitsch, H. "High order conservative finite difference scheme for variable density low Mach number turbulent flows". In: *Journal of Computational Physics* 227.15 (2008), pp. 7125–7159. DOI: `10.1016/j.jcp.2008.03.027`.

[28] Di Renzo, M., De Palma, P., Tullio, M. D. de and Pascazio, G. "An efficient flamelet progress-variable method for modeling non-premixed flames in weak electric fields". In: *Computers & Fluids* 157 (2017), pp. 14–27. DOI: `10.1016/j.compfluid.2017.08.024`.

[29] Domingo, P. and Vervisch, L. "Triple flames and partially premixed combustion in autoignition of non-premixed turbulent mixtures". In: *Symposium (International) on Combustion* 26.1 (Jan. 1996), pp. 233–240. DOI: `10.1016/S0082-0784(96)80221-9`.

[30] Ern, A. and Giovangigli, V. *Multicomponent transport algorithms*. Ed. by Araki, H. et al. Vol. 24. Lecture Notes in Physics Monographs. Berlin, Heidelberg: Springer Berlin Heidelberg, 1994. DOI: `10.1007/978-3-540-48650-3`.

[31] Fialkov, A. "Investigations on ions in flames". In: *Progress in Energy and Combustion Science* 23.5-6 (1997), pp. 399–528. DOI: `10.1016/S0360-1285(97)00016-6`.

[32] Fiorina, B., Gicquel, O., Vervisch, L., Carpentier, S. and Darabiha, N. "Approximating the chemical structure of partially premixed and diffusion counterflow flames using FPI flamelet tabulation". In: *Combustion and Flame* 140.3 (2005), pp. 147–160. DOI: `10.1016/j.combustflame.2004.11.002`.

[33] Fiorina, B., Vicquelin, R., Auzillon, P., Darabiha, N., Gicquel, O. and Veynante, D. "A filtered tabulated chemistry model for LES of premixed combustion". In: *Combustion and Flame* 157.3 (2010), pp. 465–475. DOI: `10.1016/j.combustflame.2009.09.015`.

[34] Firsov, A., Savelkin, K. V., Yarantsev, D. A. and Leonov, S. B. "Plasma-enhanced mixing and flameholding in supersonic flow". In: *Philosophical Transactions of the Royal Society A: Mathematical, Physical and Engineering Sciences* 373.2048 (2015), p. 20140337. DOI: `10.1098/rsta.2014.0337`.

[35] Fox, J. S. and Mirchandani, I. "Influence of electric fields on burning velocity". In: *Combustion and Flame* 22.2 (1974), pp. 267–268. DOI: `10.1016/S0010-2180(74)80015-5`.

[36] Gomez, A. and Chen, G. "Charge-Induced Secondary Atomization in Diffusion Flames of Electrostatic Sprays". In: *Combustion Science and Technology* 96.1-3 (1994), pp. 47–59. DOI: `10.1080/00102209408935346`.

[37] Goodings, J. M. and Bohme, D. K. "Positive ion probe of mehtane-oxygen combustion". In: *Kinetics of Elementary Reactions* (1974), pp. 891–902. DOI: `10.1016/S0082-0784(77)80382-2`.

[38] Goodings, J. M., Bohme, D. K. and Chun-Wai NG. "Detailed ion chemistry in methane-oxygen flames. I. Positive ions". In: *Combustion and Flame* 36 (1979), pp. 27–43. DOI: `10.1016/0010-2180(79)90045-2`.

[39] Goodings, J. M., Bohme, D. K. and Chun-Wai NG. "Detailed ion chemistry in methane-oxygen flames. II. Negative ions". In: *Combustion and Flame* 36 (1979), pp. 45–62. DOI: `10.1016/0010-2180(79)90045-2`.

[40] Guenault, E. M. and Wheeler, R. V. "XXVII.-The propagation of flame in electric fields. Part I. Distortion of the flame surface". In: *Journal of the Chemical Society (Resumed)* (1931), pp. 195–199. DOI: `10.1039/JR9310000195`.

[41] Guerra-Garcia, C. and Martinez-Sanchez, M. "Counterflow nonpremixed flame DC displacement under AC electric field". In: *Combustion and Flame* 162.11 (2015), pp. 4254–4263. DOI: `10.1016/j.combustflame.2015.07.038`.

[42] Han, J., Belhi, M. and Bisetti, F. "Numerical modeling of ion transport in flames". In: *Combustion Theory and Modelling* 19.6 (2015), pp. 744–772. DOI: `10.1080/13647830.2015.1090018`.

[43] Han, J., Belhi, M., Casey, T. A., Bisetti, F., Im, H. G. and Chen, J. Y. "The i-V curve characteristics of burner-stabilized premixed flames: Detailed and reduced models". In: *Proceedings of the Combustion Institute* 36.1 (2017), pp. 1241–1250. DOI: `10.1016/j.proci.2016.05.056`.

[44] Hayhurst, A. N. "The mass spectrometric sampling of ions from atmospheric pressure flames as exemplified by the reactions of OH- and O2- in O2-rich flames". In: *Pure and Applied Chemistry* 65.2 (1993), pp. 285–295. DOI: `10.1351/pac199365020285`.

[45] Hirschfelder, J. O., Curtiss, C. F. and Bird, R. B. *Molecular theory of gases and liquids*. John Wiley & Sons, 1964, p. 1249.

[46] Hu, J., Rivin, B. and Sher, E. "The effect of an electric field on the shape of co-flowing and candle-type methane–air flames". In: *Experimental Thermal and Fluid Science* 21.1–3 (2000), pp. 124–133. DOI: `http://dx.doi.org/10.1016/S0894-1777(99)00062-X`.

[47] Hutchins, A. R., Reach, W. A., Kribs, J. D. and Lyons, K. M. "Effects of Electric Fields on Stabilized Lifted Propane Flames". In: *Journal of Energy Resources Technology* 136.2 (2014), pp. 1–10. DOI: `10.1115/1.4027407`.

[48] Ihme, M. and Pitsch, H. "Modeling of radiation and nitric oxide formation in turbulent nonpremixed flames using a flamelet/progress variable formulation". In: *Physics of Fluids* 20.5 (2008), p. 055110. DOI: `10.1063/1.2911047`.

[49] Ihme, M. and Pitsch, H. "Prediction of extinction and reignition in nonpremixed turbulent flames using a flamelet/progress variable model 1. A priori study and presumed PDF closure". In: *Combustion and Flame* 155 (2008), pp. 80–89. DOI: `10.1016/j.combustflame.2008.04.015`.

[50] Ihme, M. and Pitsch, H. "Prediction of extinction and reignition in nonpremixed turbulent flames using a flamelet/progress variable model 2. Application in LES of Sandia flames D and E". In: *Combustion and Flame* 155 (2008), pp. 90–107. DOI: `10.1016/j.combustflame.2008.04.015`.

[51] Jaggers, H. C. and Engel, A. von. "The effect of electric fields on the burning velocity of various flames". In: *Combustion and Flame* 16.3 (1971), pp. 275–285. DOI: `10.1016/S0010-2180(71)80098-6`.

[52] Kee, R. J., Dixon-Lewis, G., Warnatz, J., Coltrin, M. and Miller, J. A. "A FORTRAN computer code package for the evaluation of gas-phase multicomponent transport properties". In: *Sandia report* SAND86-824.December (1986), pp. 3–39. DOI: `citeulike-article-id:8257884`.

[53] Kim, J. S. and Williams, F. A. "Structures of Flow and Mixture-Fraction Fields for Counterflow Diffusion Flames with Small Stoichiometric Mixture Fractions". In: *SIAM Journal on Applied Mathematics* 53.6 (Dec. 1993), pp. 1551–1566. DOI: `10.1137/0153072`.

[54] Kim, M. K., Ryu, S. K., Won, S. H. and Chung, S. H. "Electric fields effect on liftoff and blowoff of nonpremixed laminar jet flames in a coflow". In: *Combustion and Flame* 157.1 (2010), pp. 17–24. DOI: `10.1016/j.combustflame.2009.10.002`.

[55] Knudsen, E. and Pitsch, H. "A general flamelet transformation useful for distinguishing between premixed and non-premixed modes of combustion". In: *Combustion and Flame* 156.3 (2009), pp. 678–696. DOI: `10.1016/j.combustflame.2008.10.021`.

[56] Kono, M., Carleton, F. B., Jones, A. R. and Weinberg, F. J. "The effect of nonsteady electric fields on sooting flames". In: *Combustion and Flame* 78.3-4 (1989), pp. 357–364. DOI: `10.1016/0010-2180(89)90023-0`.

[57] Lacoste, D. A., Xiong, Y., Moeck, J. P., Chung, S. H., Roberts, W. L. and Cha, M. S. "Transfer functions of laminar premixed flames subjected to forcing by acoustic waves, AC electric fields, and non-thermal plasma discharges". In: *Proceedings of the Combustion Institute*. Elsevie Inc., 2016. DOI: `10.1016/j.proci.2016.05.034`.

[58] Law, C. K. *Combustion Physics*. Cambridge: Cambridge University Press, 2006. DOI: `10.1017/CBO9780511754517`.

[59] Lawton, J. and Weinberg, F. J. "Maximum Ion Currents from Flames and the Maximum Practical Effects of Applied Electric Fields". In: *Proceedings of the Royal Society of London A: Mathematical, Physical and Engineering Sciences* 277.1371 (Feb. 1964), pp. 468–497. DOI: `10.1098/rspa.1964.0035`.

[60] Lee, S. M., Park, C. S., Cha, M. S. and Chung, S. H. "Effect of electric fields on the liftoff of nonpremixed turbulent jet flames". In: *IEEE Transactions on Plasma Science* 33.5 (2005), pp. 1703–1709. DOI: `10.1109/TPS.2005.856414`.

[61] Lewis, B. and Kreutz, C. D. "The Effect of an Electric Field on the Flame Temperature of Combustible Gas Mixtures". In: *Journal of the American Chemical Society* 55.3 (1933), pp. 934–938. DOI: `10.1021/ja01330a009`.

[62] Liñán, A. "The asymptotic structure of counterflow diffusion flames for large activation energies". In: *Acta Astronautica* 1.7-8 (July 1974), pp. 1007–1039. DOI: `10.1016/0094-5765(74)90066-6`.

[63] Marcum, S. D. and Ganguly, B. N. "Electric-field-induced flame speed modification". In: *Combustion and Flame* 143.1-2 (2005), pp. 27–36. DOI: `10.1016/j.combustflame.2005.04.008`.

[64] Mason, E. A. and McDaniel, E. W. *Transport Properties of Ions in Gases*. New York: Wiley, 1988. DOI: `10.1002/3527602852`.

[65] Masri, A. R., Bilger, R. W. and Dibble, R. W. "Turbulent nonpremixed flames of methane near extinction: Probability density functions". In: *Combustion and Flame* 73.3 (Sept. 1988), pp. 261–285. DOI: `10.1016/0010-2180(88)90023-5`.

[66] Mathur, S., Tondon, P. K. and Saxena, S. C. "Molecular Physics Thermal conductivity of binary, ternary and quaternary mixtures of rare gases Thermal conductivity of binary, ternary and quaternary mixtures of rare gases". In: *Molecular Physics* 12.6 (1967), pp. 569–579. DOI: `10.1080/00268976700100731`.

[67] Mcbride, B., Gordon, S. and Reno, M. "Coefficients for Calculating Thermodynamic and Transport Properties of Individual Species". In: *Nasa Technical Memorandum* 4513.NASA-TM-4513 (1993), p. 98.

[68] Mehresh, P., Souder, J., Flowers, D., Riedel, U. and Dibble, R. W. "Combustion timing in HCCI engines determined by ion-sensor: Experimental and kinetic modeling". In: *Proceedings of the Combustion Institute* 30.2 (2005), pp. 2701–2709. DOI: `10.1016/j.proci.2004.08.135`.

[69] Metcalfe, W. K., Burke, S. M., Ahmed, S. S. and Curran, H. J. "A hierarchical and comparative kinetic modeling study of C1 - C2 hydrocarbon and oxygenated fuels". In: *International Journal of Chemical Kinetics* 45.10 (2013), pp. 638–675. DOI: `10.1002/kin.20802`.

[70] Mittal, V., Pitsch, H. and Egolfopoulos, F. "Assessment of counterflow to measure laminar burning velocities using direct numerical simulations". In: *Combustion Theory and Modelling* 16.3 (June 2012), pp. 419–433. DOI: `10.1080/13647830.2011.631033`.

[71] Monchick, L. and Mason, E. A. "Transport Properties of Polar Gases". In: *The Journal of Chemical Physics* 35.5 (Nov. 1961), pp. 1676–1697. DOI: `10.1063/1.1732130`.

[72] Moureau, V., Domingo, P. and Vervisch, L. "From Large-Eddy Simulation to Direct Numerical Simulation of a lean premixed swirl flame: Filtered laminar flame-PDF modeling". In: *Combustion and Flame* 158.7 (2011), pp. 1340–1357. DOI: `10.1016/j.combustflame.2010.12.004`.

[73] Mueller, M. E., Iaccarino, G. and Pitsch, H. "Chemical kinetic uncertainty quantification for Large Eddy Simulation of turbulent nonpremixed combustion". In: *Proceedings of the Combustion Institute* (2012), pp. 1–16. DOI: `10.1016/j.proci.2012.07.054`.

[74] Nagaraja, S., Li, T., Sutton, J. A., Adamovich, I. V. and Yang, V. "Nanosecond plasma enhanced H2/O2/N2 premixed flat flames". In: *Proceedings of the Combustion Institute* 35.3 (2015), pp. 3471–3478. DOI: `10.1016/j.proci.2014.08.024`.

[75] Nair, S., Rajaram, R., Meyers, A. J., Lieuwen, T. C., Tozzi, L. and Benson, K. "Acoustic and Ion Sensing of Lean Blowout in an Aircraft Combustor Simulator". In: *43rd AIAA Aerospace Sciences Meeting and Exhibit*. Reston, Viriginia: American Institute of Aeronautics and Astronautics, Jan. 2005. DOI: `10.2514/6.2005-932`.

[76] Papac, M. J. "Effects of Electric Fields on Convection in Combustion Plasmas and Surrounding Gases". In: *36th AIAA Plasmadynamics and Lasers Conference*. 2005. DOI: `10.2514/6.2005-4784`.

[77] Papac, M. J. and Dunn-Rankin, D. "Modelling electric field driven convection in small combustion plasmas and surrounding gases". In: *Combustion Theory and Modelling* 12.1 (Feb. 2008), pp. 23–44. DOI: `10.1080/13647830701383814`.

[78] Park, D. G., Chung, S. H. and Cha, M. S. "Bidirectional ionic wind in nonpremixed counterflow flames with DC electric fields". In: *Combustion and Flame* 168 (2016), pp. 138–146. DOI: `10.1016/j.combustflame.2016.03.025`.

[79] Park, D. and Cha, M. S. Private Communication. 2016.

[80] Pecquery, F., Moureau, V., Lartigue, G., Vervisch, L. and Roux, A. "Modelling nitrogen oxide emissions in turbulent flames with air dilution: Application to LES of a non-premixed jet-flame". In: *Combustion and Flame* 161.2 (2014), pp. 496–509. DOI: `10.1016/j.combustflame.2013.09.018`.

[81] Pedersen, T. and Brown, R. C. "Simulation of electric field effects in premixed methane flames". In: *Combustion and Flame* 94.4 (1993), pp. 433–448. DOI: `10.1016/0010-2180(93)90125-M`.

[82] Peeters, J. and Mahnen, G. "Reaction Mechanisms and Rate Constants of Elementary Steps in Methane - Oxygen Flames". In: *Symposium (International) on Combustion* (1973).

[83] Peters, N. "Laminar diffusion flamelet models in non-premixed turbulent combustion". In: *Progress in Energy and Combustion Science* 10.3 (Jan. 1984), pp. 319–339. DOI: `10.1016/0360-1285(84)90114-X`.

[84] Peters, N. "Local Quenching Due to Flame Stretch and Non-Premixed Turbulent Combustion". In: *Combustion Science and Technology* 30.1-6 (Jan. 1983), pp. 1–17. DOI: `10.1080/00102208308923608`.

[85] Peters, N. *Turbulent Combustion*. Ed. by Davis, S., Freund, L. B., Leibovich, S. and Tvergaard, V. Cambridge University Press, 2004. DOI: `10.1088/0957-0233/12/11/708`.

[86] Pierce, C. D. and Moin, P. "Progress-variable approach for large-eddy simulation of non-premixed turbulent combustion". In: *Journal of Fluid Mechanics* 504 (2004), pp. 73–97.

[87] Pitsch, H. *FLAMEMASTER V3.3.10: A C++ computer program for 0D combustion and 1D laminar flame calculations*. 1998. URL: `http://www.itv.rwth-aachen.de/en/downloads/flamemaster/`.

[88] Pitsch, H. and Peters, N. "A Consistent Flamelet Formulation for Non-Premixed Combustion Considering Differential Diffusion Effects". In: *Combustion and Flame* 114.1-2 (July 1998), pp. 26–40. DOI: `10.1016/S0010-2180(97)00278-2`.

[89] Plessing, T., Terhoeven, P., Peters, N. and Mansour, M. S. "An experimental and numerical study of a laminar triple flame". In: *Combustion and Flame* 115.3 (1998), pp. 335–353. DOI: `10.1016/S0010-2180(98)00013-3`.

[90] Poinsot, T. and Veynante, D. *Theoretical and Nemerical Combustion*. 2005.

[91] Prager, J., Riedel, U. and Warnatz, J. "Modeling ion chemistry and charged species diffusion in lean methane-oxygen flames". In: *Proceedings of the Combustion Institute* 31 (2007), pp. 1129–1137. DOI: `10.1016/j.proci.2006.07.141`.

[92] Rockwood, S. D. "Elastic and inelastic cross sections for electron-Hg scattering from Hg transport data". In: *Physical Review A* 8.5 (1973), pp. 2348–2358. DOI: `10.1103/PhysRevA.8.2348`.

[93] Ruetsch, G. R., Vervisch, L. and Liñán, A. "Effects of heat release on triple flames". In: *Physics of Fluids* 7.6 (1995), p. 1447. DOI: `10.1063/1.868531`.

[94] Ryu, S. K., Kim, Y. K., Kim, M. K., Won, S. H. and Chung, S. H. "Observation of multi-scale oscillation of laminar lifted flames with low-frequency AC electric fields". In: *Combustion and Flame* 157.1 (2010), pp. 25–32. DOI: `10.1016/j.combustflame.2009.10.001`.

[95] Seshadri, K. and Peters, N. "Asymptotic structure and extinction of methane-air diffusion flames". In: *Combustion and Flame* 73.1 (July 1988), pp. 23–44. DOI: `10.1016/0010-2180(88)90051-X`.

[96] Sher, E., Pinhasi, G., Pokryvailo, A. and Bar-On, R. "Extinction of pool flames by means of a DC electric field". In: *Combustion and Flame* 94.3 (1993), pp. 244–252. DOI: `10.1016/0010-2180(93)90071-A`.

[97] Shunn, L., Ham, F. and Moin, P. "Verification of variable-density flow solvers using manufactured solutions". In: *Journal of Computational Physics* 231.9 (2012), pp. 3801–3827. DOI: `10.1016/j.jcp.2012.01.027`.

[98] Smith, G. P. et al. *GriMech 3.0.* 2000. URL: `http://www.me.berkeley.edu/gri_mech/`.

[99] Sommerer, T. J. and Kushner, M. J. "Numerical investigation of the kinetics and chemistry of rf glow discharge plasmas sustained in He, N 2, O 2, He/N 2/O 2, He/CF4 /O2 , and SiH4 /NH3 using a Monte Carlofluid hybrid model". In: *Journal of Applied Physics* 71.4 (Feb. 1992), pp. 1654–1673. DOI: `10.1063/1.351196`.

[100] Speelman, N., Goey, L. P. H. de and Oijen, J. A. van. "Development of a numerical model for the electric current in burner-stabilised methane–air flames". In: *Combustion Theory and Modelling* 19.2 (2015), pp. 159–187. DOI: `10.1080/13647830.2014.998712`.

[101] Speelman, N., Kiefer, M., Markus, D., Maas, U., Goey, L. P. H. de and Oijen, J. A. van. "Validation of a novel numerical model for the electric currents in burner-stabilized methane–air flames". In: *Proceedings of the Combustion Institute* 35.1 (2015), pp. 847–854. DOI: `10.1016/j.proci.2014.05.067`.

[102] Starik, A. M. and Titova, N. S. "Kinetics of Ion Formation in the Volumetric Reaction of Methane with Air". In: *Combustion, Explosion and Shock Waves* 38.3 (2002), pp. 253–268. DOI: `10.1023/A:1015668900629`.

[103] Starikovskaia, S. M., Starikovskii, A. Y. and Zatsepin, D. V. "Hydrogen oxidation in a stoichiometric hydrogen-air mixture in the fast ionization wave". In: *Combustion Theory and Modelling* 5.1 (Mar. 2001), pp. 97–129. DOI: `10.1088/1364-7830/5/1/306`.

[104] Starikovskii, A. Y. "Plasma supported combustion". In: *Proceedings of the Combustion Institute* 30 II (2005), pp. 2405–2417. DOI: `10.1016/j.proci.2004.08.272`.

[105] Starikovskiy, A. and Aleksandrov, N. "Plasma-assisted ignition and combustion". In: *Progress in Energy and Combustion Science* 39.1 (2013), pp. 61–110.

[106] Stokes, G. G. *On the theories of the internal friction of cluids in motion*. 1845. DOI: `10.1017/CBO9780511702242`.

[107] Teuff, Y. H. L., T. J. Millar, T. J. and A.J. Markwick, T. J. *The UMIST database for astrochemistry*. 1999. URL: `http://www.rate99.co.uk`.

[108] Veynante, D., Fiorina, B., Domingo, P. and Vervisch, L. "Using self-similar properties of turbulent premixed flames to downsize chemical tables in high-performance numerical simulations". In: *Combustion Theory and Modelling* 12.6 (Nov. 2008), pp. 1055–1088. DOI: `10.1080/13647830802209710`.

[109] Vinogradov, J., Sher, E., Rutkevich, I. and Mond, M. "Voltage-current characteristics of a flame-assisted unipolar corona". In: *Combustion and Flame* 127 (2001), pp. 2041–2050. DOI: `10.1016/S0010-2180(01)00305-4`.

[110] Wang, H., You, X., Joshi, A. V., Davis, S. G., Laskin, A., Egolfopoulos, F. and Law, C. K. *USC Mech Version II. High-Temperature Combustion Reaction Model of H2/CO/C1-C4 Compounds*. 2007.

[111] Wang, Z. H. et al. "Investigation of combustion enhancement by ozone additive in CH4/air flames using direct laminar burning velocity measurements and kinetic simulations". In: *Combustion and Flame* 159.1 (2012), pp. 120–129. DOI: `10.1016/j.combustflame.2011.06.017`.

[112] Warnatz, J., Maas, U. and Dibble, R. W. *Combustion*. 3rd. Berlin, Heidelberg: Springer Berlin Heidelberg, 2001. DOI: `10.1007/978-3-662-04508-4`.

[113] Wilke, C. R. "A Viscosity Equation for Gas Mixtures". In: *The Journal of Chemical Physics* 18.4 (1950), pp. 517–519. DOI: `10.1063/1.1747673`.

[114] Williams, F. A. *Combustion theory*. Ed. by Williams, F. A. 2nd. The Benjamin/Cummings Publishing Company, Inc., 1985.

[115] Wisman, D. L., Marcum, S. D. and Ganguly, B. N. "Electrical control of the thermodiffusive instability in premixed propane-air flames". In: *Combustion and Flame* 151.4 (Dec. 2007), pp. 639–648. DOI: `10.1016/j.combustflame.2007.06.021`.

[116] Won, S. H., Cha, C. M., Park, C. S. and Chung, S. H. "Effect of electric fields on reattachment and propagation speed of tribrachial flames in laminar coflow jets". In: *Proceedings of the Combustion Institute* 31.1 (Jan. 2007), pp. 963–970. DOI: `10.1016/j.proci.2006.07.166`.

[117] Won, S. H., Ryu, S. K., Kim, M. K., Cha, M. S. and Chung, S. H. "Effect of electric fields on the propagation speed of tribrachial flames in coflow jets". In: *Combustion and Flame* 152.4 (Mar. 2008), pp. 496–506. DOI: `10.1016/j.combustflame.2007.11.008`.

[118] Wortberg, G. "Ion-concentration measurements in a flat flame at atmospheric pressure". In: *Symposium (International) on Combustion* 10.1 (1965), pp. 651–655. DOI: `10.1016/S0082-0784(65)80210-7`.

[119] Xiong, Y., Cha, M. S. and Chung, S. H. "AC electric field induced vortex in laminar coflow diffusion flames". In: *Proceedings of the Combustion Institute* 35.3 (2015), pp. 3513–3520. DOI: `10.1016/j.proci.2014.08.027`.

[120] Xiong, Y., Chung, S. H. and Cha, M. S. "Instability and electrical response of small laminar coflow diffusion flames under AC electric fields: Toroidal vortex formation and oscillating and spinning flames". In: *Proceedings of the Combustion Institute* (2016). DOI: `10.1016/j.proci.2016.06.022`.

[121] Xiong, Y., Park, D. G., Lee, B. J., Chung, S. H. and Cha, M. S. "DC field response of one-dimensional flames using an ionized layer model". In: *Combustion and Flame* 163 (2016), pp. 317–325. DOI: `10.1016/j.combustflame.2015.10.007`.

[122] Yagodnikov, D. A. "Effect of an Electric Field on the Stabilization of a Turbulent Propane—Air flame". In: *Combustion, Explosion, and Shock Waves* 34.1 (1998), pp. 16–19. DOI: `10.1007/BF02671810`.

[123] Yamashita, K., Karnani, S. and Dunn-Rankin, D. "Numerical prediction of ion current from a small methane jet flame". In: *Combustion and Flame* 156.6 (2009), pp. 1227–1233. DOI: `10.1016/j.combustflame.2009.02.002`.

[124] Yu, J. and Meng, H. "A numerical study of counterflow diffusion flames of methane/air at various pressures". In: *Science China Technological Sciences* 57.3 (Mar. 2014), pp. 615–624. DOI: `10.1007/s11431-014-5484-6`.